Effects of Secondary Air Injection During Cold Start of SI Engines

by

Dongkun Lee

B.S., Mechanical and Aerospace Engineering
Seoul National University, 2003

S.M., Mechanical Engineering
Massachusetts Institute of Technology, 2005

Submitted to the Department of Mechanical Engineering
in partial fulfillment of the requirements for the degree of

DOCTOR OF PHILOSOPHY

at the

MASSACHUSETTS INSTITUTE OF TECHNOLOGY

February 2010

Signature of Author ……
Department of Mechanical Engineering
January 22, 2010

Certified by ……
John B. Heywood
Professor of Mechanical Engineering
Thesis Supervisor

Accepted by ……
David E. Hardt
Chairman
Department Committee on Graduate Students

To my family

Effects of Secondary Air Injection During Cold Start of SI Engines

by

Dongkun Lee

Submitted to the Department of Mechanical Engineering
on January 22, 2010 in partial fulfillment of the requirements
for the degree of Doctor of Philosophy

Abstract

The paucity of exhaust oxygen during cold start of automobile SI engines limits the extent of exothermic chemical reactions in the exhaust port, manifold, and catalyst. The injection of air into the exhaust system therefore could be an effective way to utilize additional thermal and chemical energy available in the exhaust gas. This study investigates the thermal and chemical processes associated with secondary air injection (SAI) inside the exhaust system in order to fully exploit the simultaneous benefits of reducing converter-in emissions and improving catalyst light-off performance during cold start.

An experimental study was performed to develop a more fundamental understanding of the effects of SAI on exhaust gas emissions and catalyst light-off characteristics during cold start of a modern SI engine. The effects of several design and operating parameters such as spark retardation, fuel enrichment, secondary air flow rate and air injection location were investigated to understand the mixing, heat loss, and thermal and catalytic oxidation processes associated with SAI. Time-resolved HC, CO and CO_2 concentrations were tracked from the cylinder exit to the catalytic converter outlet and converted to mass flow rates by applying an instantaneous exhaust mass flow rate model. A phenomenological model of exhaust heat transfer combined with the gas composition analysis was also developed to define the thermal and chemical energy state of the exhaust gas with SAI.

The study found that significant emissions reduction can be achieved with SAI by the thermal oxidation process prior to the catalyst, which results in enhancing the chemical process inside the catalyst by faster catalyst light-off. The engine operation, with a relative air/fuel ratio 20% rich of stoichiometric and 100% secondary air, yielded the fastest catalyst light-off (4.2 sec). The SAI system reduced HC emissions by 46% to 88% and CO emissions by 37% to 93% compared with the normal operating conditions. The analysis showed that the post-catalyst HC emissions levels were optimized with secondary air flow rates corresponding to an overall exhaust lambda of 1.3.

Thesis Supervisor: John B. Heywood
Title: Professor of Mechanical Engineering

Contents

List of Figures

List of Tables

Nomenclature

ABDC	after bottom dead center
ATDC	after top dead center
BBDC	before bottom dead center
BDC	bottom dead center
BTDC	before top dead center
CA	crank angle
COV	coefficient of variation
DAQ	data acquisition
DOHC	dual overhead camshaft
ECM	engine control module
EGR	exhaust gas recirculation
EVC	exhaust valve closing
EVO	exhaust valve opening
FFID	fast-response flame ionization detector
FID	flame ionization detector
FTP	federal test procedure
HC	hydrocarbon
IAC	idle air control
IMEP	indicated mean effective pressure
IVC	intake valve closing
IVO	intake valve opening
MAP	manifold air pressure
MDS	modular development system
MFB	mass fraction burned
NDIR	non-dispersive infrared
PVC	positive crankcase ventilation
RPM	revolutions per minute
SAI	secondary air injection
SI	spark ignition
TDC	top dead center
UEGO	universal exhaust gas oxygen

Chapter 1

Introduction

1.1 Background

1.1.1 Cold Start Emissions

The cold start emission problem has been known from the earliest days of engine emission control. However, until the end of the 1980s, the emissions technologies were primarily aimed at fully warmed-up engine conditions. The most significant gains could be made by the use of catalytic converters without the need to address the cold start issue. This very disparity eventually brought about a change of emphasis: since exhaust gas after-treatment is now remarkably effective in reducing tailpipe-out emissions from warmed-up engines, increasing emphasis is being placed upon cold start emissions.

There are various ways of defining the term "cold start". Broadly, it means vehicle operation after any sufficiently long period of non-use. The close legal definition relates to the mandatory room temperature soak which a vehicle must undergo prior to a test protocol such as the Federal Test Procedure (FTP). Currently, the majority of the total HC and CO emissions during the FTP-75 are produced during the first 25 or so seconds of engine operation before the catalyst reaches its light-off temperature, approximately 250^{o}C [1]. Therefore much of the blame for failure to meet future, stringent emission standards can be ascribed to this cold start emission issue.

Since only a small portion of injected fuel vaporizes and contributes to the combustible mixture in a cold engine [2,3], the cold start-up process of port fuel injected SI engines generally involves significant over-fueling in the intake port. A substantial amount of fuel is injected to overcome unexpected transients as well as poor mixture preparation. This fuel enrichment provides a sufficiently large amount of vaporized fuel so that smooth and robust engine operation can be assured during the start-up process. A large portion of

this excess fuel, however, does not vaporize and enters the cylinder as liquid [4]. This fuel may be stored in various places in the cylinder (e.g. deposits, oil layers on the cylinder liner, piston top and cylinder head, or combustion chamber crevices), survive the subsequent combustion process unburned, and come out into the bulk exhaust, where catalytic converters are essentially ineffective until light-off temperatures are achieved.

1.1.2 Legislation History

Spark-ignition and diesel engines are a major source of urban air pollution. The spark-ignition engine exhaust gases contain oxides of nitrogen (nitric oxide, NO, and small amounts of nitrogen dioxide, NO_2 – collectively known as NO_x), carbon monoxide (CO), and organic compounds which are unburned or partially burned hydrocarbons (HC). The consequences of these emissions have been well documented but, briefly, CO is a direct poison to humans, while HC and NO_x undergo photochemical reactions in the sunlight, leading to the generation of smog and ozone [5].

In 1970, the US Congress passed the Clean Air Act, which called for the first tailpipe emissions standards. The pollutants controlled were carbon monoxide (CO), volatile organic compounds (VOC), and oxides of nitrogen (NO_x). The new standards went into effect in 1975 with the requirements for cars and light-duty trucks of 1.5 g/mile HC, 15.0 g/mile CO and 3.1 g/mile NO_x [6]. The Environmental Protection Agency (EPA) established a Federal Test Procedure (FTP) simulating the average driving conditions in the U.S. in which emissions were measured using a constant volume sampling system. The FTP cycle was conducted on an engine dynamometer and included measurements from the automobile during following three conditions. The test begins with a cold start Phase 1 or Bag 1 (at 20-30^{o}C) after a minimum 12 hour soak at constant ambient temperature. After 505 seconds, the vehicle is driving at the speeds indicated in the Phase 2 or Bag 2 hot stabilized portion. The vehicle is then shut-down for 600 seconds, after which a hot start Phase 3 or Bag 3 is implemented. This phase is identical to the speeds and accelerations indicated in Phase 1. The only difference between these two phases is that the first begins with a cold start and the third begins with a warm start. However, Phase 1 typically generates several times as much HC and CO as phase 3 [7].

Currently, two sets, or Tiers, of emission standards for light-duty vehicles in the United States were defined as a result of the Clean Air Act Amendments of 1990. The Tier I standard was adopted in 1991 and was phased in from 1994 to 1997. Tier II standards are being phased in from 2004 to 2009. Tier II standards reduced non-methane hydrocarbon (NMHC) emissions to a maximum of 0.125 g/mile by 2004 (down from 0.41 g/mile in 1991), CO to 1.7 g/mile (down from 3.4 g/mile in 1991), and NO_x to 0.2 g/mile (down from 1.0 g/mile).

Table 1-1 Light-Duty Vehicle -- Clean Fuel Fleet Exhaust Emission Standards from EPA

Vehicle Type	Emissions Category	Useful Life Standard	NMOG (g/mi)	NOx (g/mi)	CO (g/mi)	Formaldehyde (g/mi)	PM (g/mi)
LDVs	TLEV	Intermediate	0.125	0.4	3.4	0.015	-
	LEV		0.075	0.2	3.4	0.015	-
	ULEV		0.040	0.2	1.7	0.008	-
	TLEV	Full	0.156	0.6	4.2	0.018	0.08
	LEV		0.090	0.3	4.2	0.018	0.08
	ULEV		0.055	0.3	2.1	0.011	0.04

1.2 Motivation

Improving catalyst light-off characteristics during cold start and reducing engine-out emissions prior to catalyst light-off have been regarded as the keys to meeting future, stringent emission regulations. To address these issues, many technologies and control strategies have been proposed, such as spark retardation, charge motion control, secondary air injection, close-coupled catalysts, electrically-heated catalysts, exhaust gas ignition, HC traps, etc. Among these, secondary air injection (SAI) into the exhaust port in combination with rich engine operation received a lot of attention due to its robust and consistent performance to meet the development goal. In addition, when compared with other approaches, secondary air injection can be implemented relatively easily with today's engine system without requiring a major design change [8].

The paucity of exhaust oxygen at a cold start limits the extent of exothermic reactions in the exhaust port, manifold, and catalyst. The injection of air into the exhaust system therefore could be an effective way to utilize additional thermal and chemical energy available in the exhaust gas for low emissions. The secondary air leads to two types of lambda: "engine lambda (λ_{engine})" and "exhaust lambda ($\lambda_{exhaust}$)". The facility to adjust the latter independently of the former eases the calibration constraints. The need to attain stoichiometric fueling as rapidly as possible is relaxed because sufficient air can always be added to compensate for the deficiency in oxygen in the engine-out exhaust gas. The amount of energy available by promoting burn-up in the exhaust with secondary air is surprisingly large. Calculations have indicated that air injection into the exhaust ports can yield as much as 7kW [9]. About one third of this energy went toward heating the exhaust system and two thirds to the exhaust gas. Luminous flames have been observed extending for 50mm into the exhaust [10]. In such conditions it is the HC and CO which sustain the combustion, although it is the hydrogen which is primarily responsible for the ignition.

$$\lambda_{engine} = \left(\frac{Air_{intake}}{Fuel} \right) / (A/F)_s \tag{1.1}$$

$$\lambda_{exhaust} = \left(\frac{Air_{intake} + Air_{secondary}}{Fuel} \right) / (A/F)_s \tag{1.2}$$

1.3 Research Objectives

This study was initiated to investigate the thermal and chemical processes associated with SAI inside the exhaust system in order to maximize the simultaneous benefit of reducing converter-in emissions and improving catalyst light-off performance during cold start. There has been little study trying to examine the real engine start-up process with SAI. Most of the previous experimental studies on enhancing emission and catalyst light-off performance for the cold start-up process have been performed under the simulated steady state conditions due to the difficulty of engine control. Therefore, experiments were designed to quantify the effects of secondary air injection on emissions

and catalyst light-off performance during real cold start of SI engines. A variety of experimental techniques and equipment was utilized to quantify engine exhaust gas emissions and temperatures at various locations. Fast-response exhaust gas analyzers and exhaust gas quenching experiments provided a detailed understanding of the thermal and chemical energy of the exhaust gas from the cylinder exit to the outlet of the catalytic converter.

The objective of this research is to develop a more fundamental understanding of the effects of secondary air injection (SAI) on the cold start emissions and catalyst light-off of an SI engine. Five main tasks were carried out:

- Develop diagnostics to examine the impacts of controlled SAI on the cold start exhaust system behavior.
- Investigate the thermal and chemical processes associated with SAI inside the exhaust system.
- Identify desirable air injection strategies by examining several design and operating parameters.
- Assess the effectiveness of these SAI strategies on the cold start emissions and catalyst light-off performance.
- Develop a phenomenological based thermal model of exhaust system with SAI during the cold start-up process.

Chapter 2

Experimental Apparatus and Procedures

2.1 Experimental Setup

2.1.1 Engine and Dynamometer

Experiments were performed on a 2003 model year, GM 2.2 liter L61 Ecotec (GMX357) engine to investigate the effects of various secondary air injection approaches on the cold start-up process of a port fuel injected SI engine. The engine was coupled to an eddy current, absorbing only, dynamometer (Froude Consine AE-80). This test setup used the engine starter motor for cranking operation with full control over the engine control modules (ECM). Additional engine specifications are shown in Table 2-1.

Table 2-1 Engine specifications

Ecotec 2.2-liter, 4-cylinder Engine Specifications	
Type	Naturally Aspirated, Line 4
Displacement Volume (cc)	2189
Clearance Volume (cc)	65
Bore (mm)	86
Stroke (mm)	94.6
Connecting Rod (mm)	146.5
Wrist Pin Offset (mm)	0.8
Compression Ratio	10.0:1
Firing Order	1-3-4-2
Valve Configuration	16v DOHC
Valve Timing	IVO: 7^{o} BTDC | IVC: 56^{o} ABDC
	EVO: 46^{o} BBDC | EVC: 32^{o} ATDC
Fuel System	Sequential Fuel Injection

2.1.2 Exhaust System Setup

The engine's exhaust system consisted of a cast iron manifold, a three-way catalytic converter and a muffler. The cylinder head and exhaust manifold were equipped with passages for secondary air operation. The catalyst supplied with the engine was an active Ultra-Low-Emission Vehicle (ULEV) catalyst. The catalyst was dyno-aged 100 hours to simulate 50,000 vehicle miles. The converter had a total volume of 82 cubic inches and was 4.2 inches in diameter with 600 cells per inch. The catalyst substrate wall thickness was 0.0043 inches. The converter was composed of two bricks; the first was 2 inches in length and loaded with 3.5 grams of Palladium (Pd) and the second brick was 4 inches in length and loaded with 1.5 grams of Platinum (Pt) and 0.31 grams of Rhodium (Rh). The second brick also contained a washcoat with oxygen storage capacity (OSC). A thermocouple was embedded at the middle of each brick along the centerline of the catalyst and an additional thermocouple measured the catalyst shell temperature. Pre-catalyst and post-catalyst gas samples were acquired approximately 4.7 inches from the bricks.

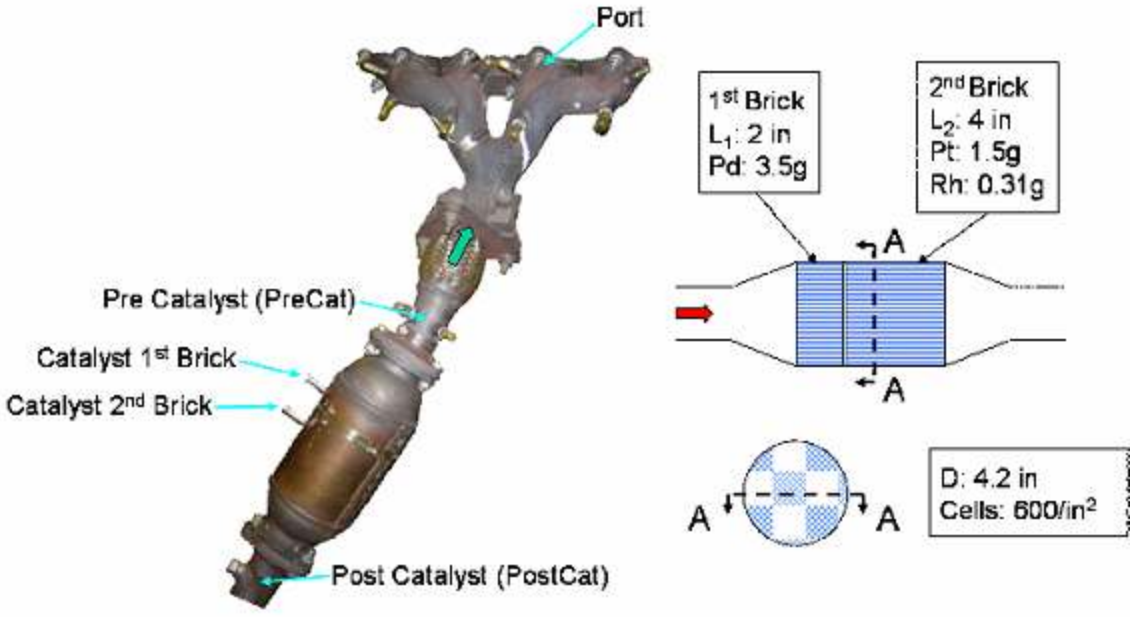

Figure 2-1 Schematic of exhaust system with active three-way catalytic converter specifications

2.1.3 Engine Subsystems and Instrumentation

Intake air mass flow rate was measured by a thermal mass flow meter (EPI, Series 8000MP). Throttle position was controlled by a stepper motor (Pacific Scientific SinMax 1.8^{o} motor with 5230 indexer/driver) connected via a cable to the engine throttle body. Incremental movement of the throttle was adjusted by two momentary contact switches with a selectable stepping rate. A pressure transducer (OMEGA PX-176) was also installed in the intake plenum that provided better transient response compared with the OEM MAP transducer.

Fuel was supplied by an external fuel pump with an inline filter, accumulator, and pressure regulator. The regulator outlet was connected to the fuel injector rail. A constant fuel rail pressure of 52 psig was maintained for a returnless fuel injection system. Injected fuel mass was calculated from the fuel pulse width duration and pressure differential across the injector. The positive crankcase ventilation (PCV) system was utilized during the engine operation, but the exhaust gas recirculation (EGR) system was not used for these experiments.

Coolant temperature was controlled by an external heat exchanger. The engine coolant system was a closed looped system driven by an internal water pump that circulated fluid through the block and cylinder head. The thermostat was removed and the heater core was modified to eliminate the recirculation of coolant within the cylinder head and block. Coolant exited the head and flowed to an external water pump installed in the engine's cooling circuit. The pump outlet was connected to an external heat exchanger and to a coolant reservoir tank before being routed back to the engine. Coolant temperature was varied via a set-point controller that actuated a valve allowing for plant water to flow through an external heat exchanger. The engine oil was not externally cooled and its temperature was measured in the oil pan.

Exhaust gas temperatures were obtained from chromel-alumel (type-K) exposed junction thermocouples (0.8-mm bead diameter) with custom radiation shielding. Exhaust air/fuel ratio was measured by a universal exhaust gas oxygen (UEGO) sensor located at the exhaust manifold collector. A Horiba MEXA-700 analyzer interpreted the signal and displayed the air/fuel ratio or the relative air/fuel ratio.

2.1.4 Engine Control System

A Delco Modular Development System (MDS) [11] was used to control and modify the engine control module (ECM). Specific ECM operations were monitored and recorded by the MDS. This system provided the user control of parameters including the change of calibration data by read only memory (ROM) emulation. A PC was connected to the MDS stack that allowed for internal and external data logging. The stack was composed of several units. The main instrument unit (MIU) was the core of the MDS and contained two embedded processors: the main instrument processor (MIP) and the input output processor (IOP). The computer interface buffer internal logging (CIBIL) provided MDS communication with a computer. The analog conversion module (ACM) contained 8-BNC outputs and 2 instantaneous switches scaled from 0 to 5 volts. A 1MB GMPX Pod was connected to the X-pod that interfaced with the ECM and allowed the ECM's EPROM to be flashed for standalone ECM operation. The shell program allowed the user to have full access to lookup tables and relevant environmental variables. Real-time monitoring and modification of several parameters (RPM, MAP, spark timing, air/fuel ratio and idle air control (IAC) valve position) was accomplished by using the MDS's external display unit (DU). Full control of the engine was possible using the Delphi Electronics Instrument Tool Suite (ITS) running the Saturn Legacy Software. File handling between the computer and MDS unit was achieved using the ITS software. The program CalTools was used to modify ECM parameters and lookup table variables.

2.1.5 Data Acquisition System

The data acquisition (DAQ) system utilized two DAQ boards from National Instruments installed in a personal computer. The first card (PCI-6071E) acquired 32 differential channels of high-speed signals. The second card (PCI-6024E) was used with a multiplexing chassis (SCXI-1000) and a 32 channel thermocouple module (SCXI-1102) to acquire temperature data from type-K thermocouples. The two boards were operated at different speeds; high-speed data was captured with a frequency of 40000 hz (once per 0.025ms), while temperature data was acquired with a frequency of 4000 hz (once per 0.25ms). Both DAQ cards were triggered from signals provided by an incremental encoder

(BEI Series H25E) coupled to the engine crankshaft. LabView software was used to create a virtual instrument for data scaling, processing, and logging.

2.1.6 In-cylinder Pressure measurements

Each cylinder was equipped with a flush-mounted piezoelectric pressure transducer (Kistler 6125A). The cylinder head passage sleeve incorporated an eight-hole flame arrestor to minimize the occurrence of thermal shock. The current signal from the transducer was converted to a voltage signal by a charge amplifier (Kistler 5010B). The transducers were statically calibrated at several pressure points using a dead weight tester. For pressure referencing, an absolute pressure transducer was installed in the intake manifold plenum that provided better transient response compared to the OEM MAP transducer. In-cylinder pressure was referenced on an individual cycle basis over a 20^{o} CA interval centered on BDC of the intake event, 170^{o} ATDC to 190^{o} ATDC, using the intake manifold plenum pressure.

2.1.7 Secondary Air Injection Setup

A secondary air injection (SAI) device was installed between the engine block and exhaust manifold as shown in Figure 2-2 and Figure 2-3. Secondary air was injected through a set of 8 tubes, with each tube directed straight towards each valve. To avoid possible back flow effects during the blowdown phase of the exhaust process, the tube design in this study had a close end and two holes drilled on the side of the tube so that the secondary air was injected from the tube perpendicular to the exhaust gas flow. The secondary air flow rates were regulated by critical orifices, which were calibrated by a mass flow meter. Three values of secondary air flow rate were tested during the constant lambda start-up experiments. The same experimental setup outlined here was used for exhaust gas quenching experiments in which secondary air was replaced by nitrogen gas.

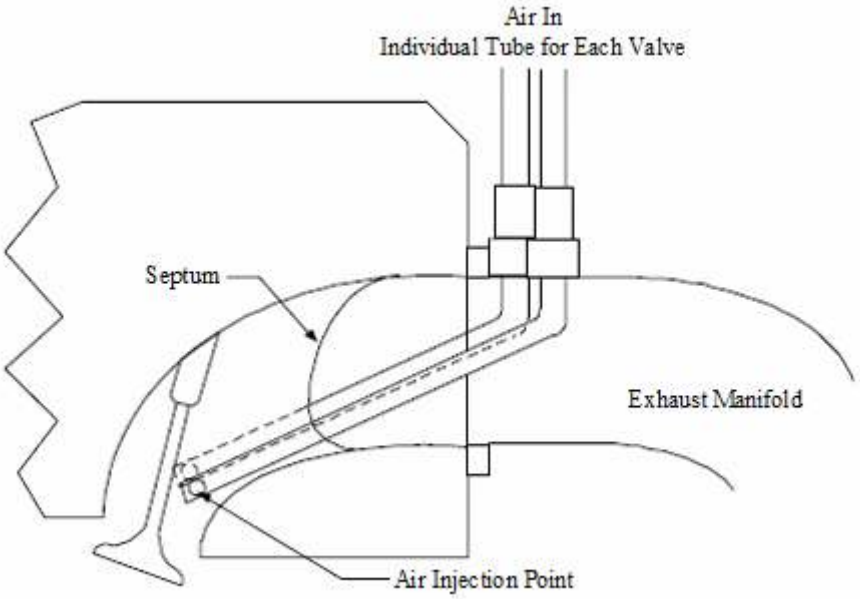

Figure 2-2 Schematic of secondary air injection probes located in the vicinity of the exhaust valve seats

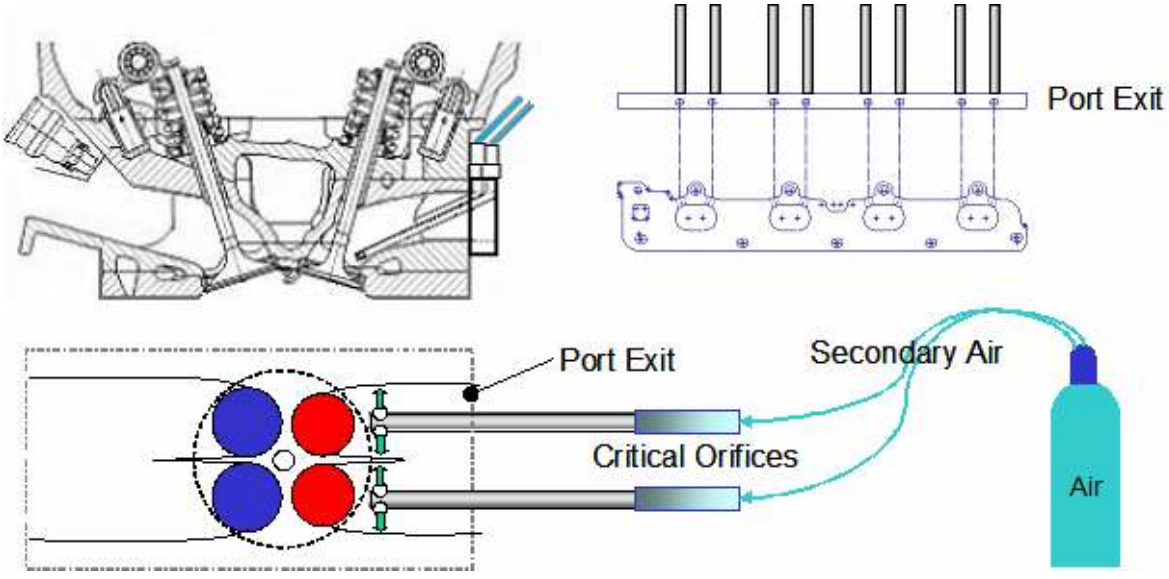

Figure 2-3 Overview of secondary air delivery system equipment (probes, critical orifices, etc.)

2.1.8 Fast-Response Emissions Analyzers

- Fast-Response HC Analyzer

Time-resolved HC concentrations were measured via a Cambustion HFR400 fast-response flame ionization detector (FID). The FID is the industry standard method of measuring HC concentration. The fast-response FID consists of a main control unit (MCU) and two remote sampling heads. The sample gas is introduced into a hydrogen flame inside the FID. Any hydrocarbons in the sample will produce ions when they are burned. Ions are detected using a metal collector which is biased with a high DC voltage. The current across this collector is thus proportional to the rate of ionization which in turn depends upon the concentration of HC in the sample gas. This fast-response FID has a 10-90 % response time of approximately 1 millisecond. A heated transfer sampling line (TSL-H) with a hole diameter of 0.026" was placed at each measurement location in the exhaust system. The fast-response FID was calibrated before and after each experiment using 1500ppmC_3 propane gas (span) and nitrogen gas (zero).

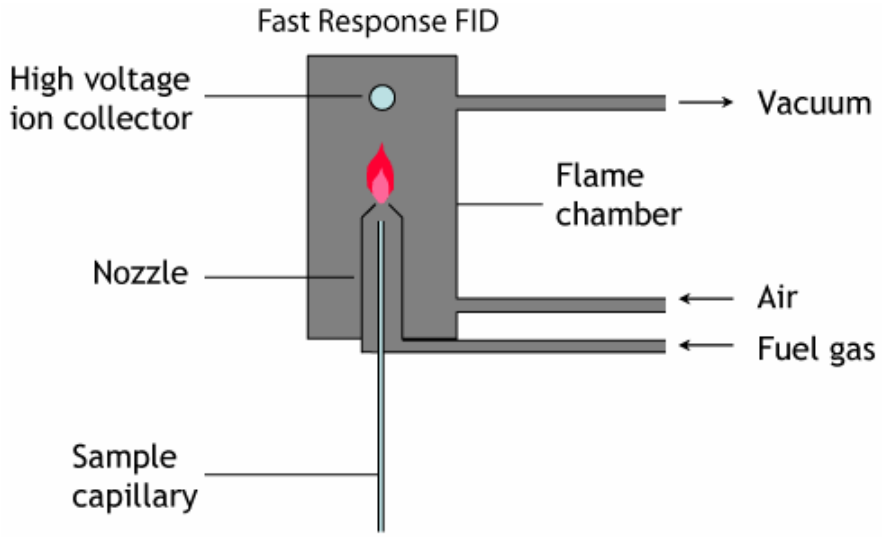

Figure 2-4 Schematic of fast-response FID sampling head from Cambustion [12].

- Fast-Response CO and CO_2 Analyzer

Time-resolved CO and CO_2 concentrations were measured via a Cambustion NDIR500 fast-response non-dispersive infrared (NDIR) detector. The NDIR is the industry standard method of measuring engine exhaust CO and CO_2 emissions. The instrument is a two-channel analyzer with the detectors located in remote sample heads. It measures CO and CO_2 simultaneously from one sample head, providing four streams of data per analyzer. Sample gas from the engine is conveyed through narrow heated capillaries directly into the sample chamber. The optical filters are mounted on a chopping wheel; reference and blank sectors on the chopping wheel correct for minute changes in temperature and IR emitter performance. The instrument gives a $T_{10–90}$ response time of approximately 8 milliseconds. The main control unit is housed in a mobile cabinet with the vacuum pump located in the base. The analyzer is controlled via RS232 or RS485 serial communications from a laptop computer with the installed operating software. The interface provides full control of the instrument including auto-calibration, start-up, self-test, and trouble-shooting and help functions with video assistance. Recommended cleaning process was conducted before and after each experiment to remove accumulations from optical windows.

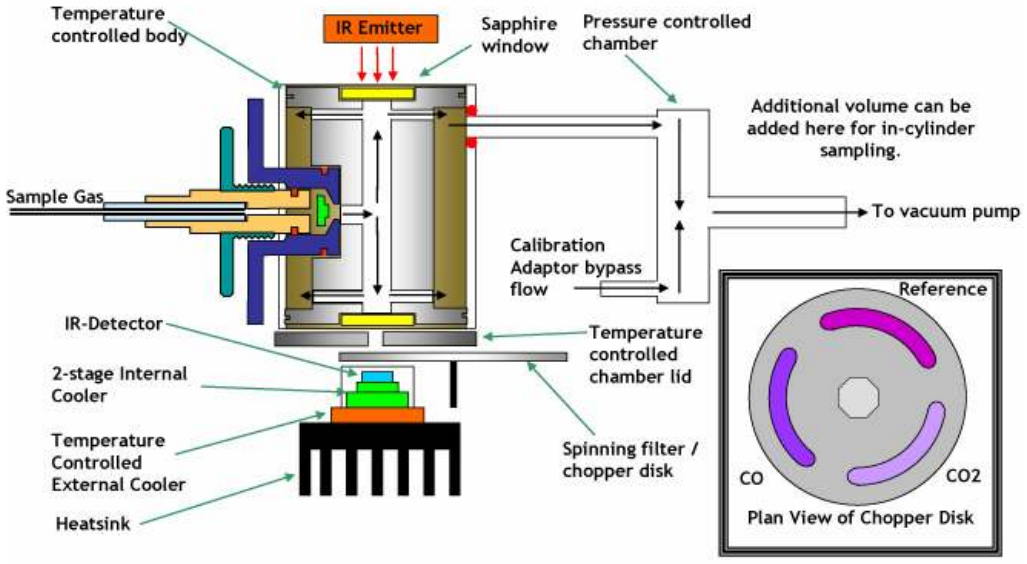

Figure 2-5 Schematic of fast-response NDIR sampling head from Cambustion [13].

2.2 Experimental Conditions and Procedures

2.2.1 Steady State Test Conditions and Procedures

Steady state cold-fluid experiments were performed to understand the basic effects of secondary air injection on exhaust gas emissions and temperatures. In order to simulate the park idle condition, the engine was operated at the condition of 1200 rpm, 8.0 g/s intake air flow rate with secondary air or nitrogen injection. Spark timing sweeps were conducted with a fixed coolant temperature of 20^{o}C and a relative air/fuel ratio of 0.9. The coolant temperature was regulated by an external heat exchanger. The exhaust system, however, was not externally cooled and was allowed to reach a hot stabilized temperature for steady state experiments. A set of data for 300 cycles was recorded for each operating condition. All experiments were performed with unleaded test gasoline (UTG), commonly termed "Indolene". This is a standardized fuel type typically used for emissions certification and laboratory work. UTG-91 from Chevron Phillips Chemical Company LLC was used for these experiments to represent the performance of gasoline. The relevant specification of this fuel is in Table 2-2.

Table 2-2 Unleaded test gasoline (Indolene, UTG-91) properties [14].

UTG-91

Property	Typical Value	Specification	Test Method
Specific Gravity at 60/60 °F	0.7350	0.7343 – 0.7440	ASTM D 4052
API Gravity	61.0	Report	ASTM D 1250
Copper Corrosion, 3 h at 50 °C	1	1 max	ASTM D 130
Existent Gum (washed), mg/100 mL	2	5 max	ASTM D 381
Sulfur, ppm	130	1000 max	ASTM D 5453
Reid Vapor Pressure, psia	9.0	8.8 – 9.2	ASTM D 5191
Lead, g/gal	0.0010	0.0050 max	ICP/OES
Phosphorus, g/gal	0.001	0.002 max	ICP/OES
Hydrogen, wt %	13.7	Report	ASTM D 5291
Carbon, wt %	86.3	Report	ASTM D 5291
Carbon Density, g/gal		Report	Calculated
Distillation Range at 760 mmHg, °F			ASTM D 86
Initial Boiling Point	88	75 – 95	
10%	122	120 – 135	
50%	212	200 – 230	
90%	321	300 – 325	
End Point	399	415 max	
Oxidation Stability, min	> 1440	1440 min	ASTM D 525
Heat of Combustion, Net, Btu/lb	18500	Report	ASTM D 240
Composition, vol %			ASTM D 1319
Aromatics	24.0	35.0 max	
Olefins	6.0	10.0 max	
Saturates	70.0	Report	
Research Octane Number	90.8	90.3 – 91.7	ASTM D 2699
Motor Octane Number	82.8	Report	ASTM D 2700
Anti-Knock Index, (R+M)/2	86.8	87.0 max	Calculated
Sensitivity	7.8	7.5 min	Calculated
Oxygenates, vol %		0.0 max	Chromatography
Benzene, vol %		Report	Chromatography

2.2.2 Start-up Test Conditions and Procedures

Engine start-up experiments were conducted with three different constant lambda start-up strategies. Exhaust gas emissions and catalyst light-off characteristics were evaluated with the various fuel injection and spark timing strategies during the first 25 seconds following engine cranking. General Motors provided the target speed-load point during the park idle period of the FTP (0-15 seconds) for this engine. The baseline calibration produced a Net-IMEP of 2.5 bar and 1000 RPM with 0.45 bar MAP and 6^{o}BTDC spark timing. However, the idle speed of these experiments was raised up to 1450 RPM in order to provide a higher rate of thermal energy to the catalyst. Therefore, the engine was calibrated using the MDS hardware and CalTools software to achieve the target operation condition for the park idle period, 2.0 bar Net-IMEP and 1450 RPM. All engine start-up tests were conducted with Indolene (UTG-91, Table 2-2) at approximately 20^{o}C environmental conditions. The coolant temperature was initially fixed at 20^{o}C by the external coolant control system.

After each start-up test, the engine was operated and warmed up to a coolant temperature of 70^{o}C to avoid residual fuel build-up in the intake port [15]. After shutdown, the engine was purged by cranking with the injector off for 1 minute. Then, the exhaust system including the catalyst was purged with compressed air for 5 minutes. This purging process was performed when the catalyst was still very hot, over 500^{o}C. Flowing compressed air into the exhaust system burned up residual HC in the exhaust system, especially inside the catalyst. Metal temperatures throughout the engine and exhaust system, then, were force-cooled to ambient temperatures before another experiment was conducted.

Several previous studies showed that the engine start-up behavior is affected by the initial phasing of the piston positions [16,17]. For a 4-cylinder 4-stroke engine, the engine tends to stop with one of the pistons at mid stroke (~90^{o} from the BDC) of compression. Therefore, the piston starting point was fixed at 60^{o}ATDC of the expansion stroke of cylinder #4 to avoid excessive complexity in data analysis.

Engine speed and load were not regulated by the dynamometer controller (Digalog Series 1022A) due to the unstable transient control of the dyno-engine system during start-up RPM flare. The required engine idle load was achieved by utilizing engine

accessories with the dynamometer coupled but not absorbing power from the engine. Two components, a hydraulic power steering pump and an alternator, were added to the engine setup to simulate park idle load conditions observed during the first 15 seconds of the FTP. The power steering pump was throttled to 800 psig by the use of a needle valve. The low pressure line was routed through a heat exchanger before returning oil to the reservoir tank. The regulated 14.7 volt output from the alternator was isolated from the 12 volt battery bus by a zener diode and connected to bank of power watt resistors, which had total 0.2 Ohm (three 0.6 Ohm resistors in parallel).

Chapter 3

Overview of Secondary Air Injection

3.1 Secondary Air Injection

3.1.1 Overview

It is well known that engine-out exhaust gas composition varies substantially with engine air/fuel ratio. When the engine is operated with a richer-than-stoichiometric mixture, hydrogen and carbon monoxide will be produced and exhausted into the exhaust stream. The concentrations of H_2 and CO in the exhaust gas rise steadily as the mixture gets richer. A similar trend is also true with engine-out HC emissions. Injecting secondary air into the exhaust port, which allows the secondary air to mix and react with these reactants (H_2, CO, HC) produced during fuel-rich operation, leads to an exothermic reaction in the exhaust system. This reaction can effectively reduce HC emissions inside the exhaust manifold and simultaneously accelerate the heating process of the catalytic converter following a cold start of gasoline engines [8].

At first thought, secondary air is rather a straightforward method of combating cold start emissions, but it does require some careful optimization nonetheless. The reason is that the physical cooling imparted by cold air entering the exhaust stream runs counter to the chemical heating imparted by oxidation of combustible gases. Heating the secondary air prior to injection ameliorates this trade-off [18], but this does not appear to have been widely-adopted. Much then rests on the location of injection. If air is injected at the catalyst inlet, then oxidation can take place within the catalyst itself. This will assist light-off. However, this beneficial effect is opposed by the entry of cold air. On the other hand, if injection takes place at the exhaust ports, then the exhaust is usually still hot enough for chemical energy to be generated by homogeneous gas phase reactions. The chemical energy released in this way may easily out-weigh the cooling effect.

3.1.2 Thermal Oxidation vs. Catalytic Oxidation [8]

In general, the chemical reactions occurring in the exhaust system with secondary air injection can be categorized into two types of oxidation of reactants as discussed above. These two types of oxidation are both exothermic, but the temperatures required for these to occur rapidly are significantly different. One is the oxidation process that happens inside the exhaust port and manifold prior to the catalytic converter, which is referred to as "thermal oxidation" in this experimental study. The other is the oxidation of HC and CO that occurs inside the catalytic converter, which is significantly different from thermal oxidation due to the presence of a catalyst and is referred to as "catalytic oxidation".

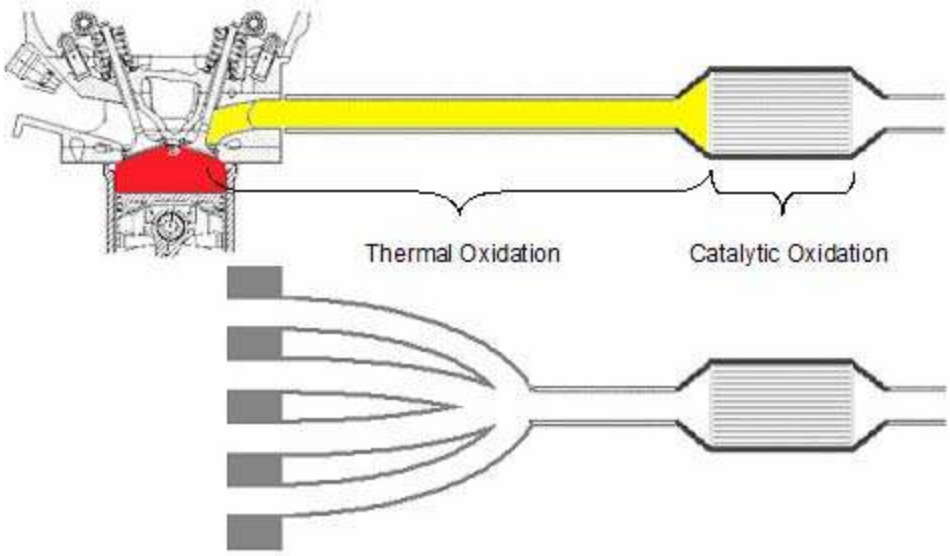

Figure 3-1 Schematic of thermal oxidation and catalytic oxidation in the exhaust system.

Thermal oxidation usually requires a temperature of 750^{o}C or higher to become significant, depending on the exhaust species and residence time. It is believed that the production of H_2 in engine combustion can significantly enhance the thermal oxidation process inside the exhaust port and manifold, and CO and HC can well sustain the process once it is established [10]. In contrast, the conversion of HC and CO can start at a similar rate with a much lower temperature (200^{o}C) on the surface of certain types of catalysts [1]. Both thermal oxidation and catalytic oxidation contribute to heating the catalyst for

shortening the light-off time. In comparison, catalytic oxidation is more effective in improving the catalyst light-off by heating the catalyst directly when it reaches a certain temperature threshold. This must be provided by cylinder-out exhaust heat plus upstream thermal oxidation. Part of the heat produced via thermal oxidation will be dissipated to the exhaust manifold walls and as a result, its impact on catalyst light-off will be slightly degraded.

However, thermal oxidation can be very effective in removing engine-out HC emissions, if adequate temperatures are sustained. This is extremely important prior to catalyst light-off. Rich engine operation generally produces higher engine-out HC emissions as compared to that of lean operation, which demands a further reduction in converter-in emissions. With the addition of secondary air, the converter-in emissions can be reduced significantly due to the enhanced oxidation in the manifold.

Thus, a good compromise between the exhaust manifold thermal oxidation and catalytic oxidation of CO and HC emissions is necessary. The former provides the heat necessary to initiate the exothermic reaction of CO and HC on the catalyst surface and reduces the HC and CO loading on the catalyst to minimize any emissions breakthrough. The latter has a direct heating effect on the catalyst surface and requires a certain level of HC and CO emissions to achieve this. If the thermal oxidation consumes too much engine-out reactants, which is important in minimizing HC emissions prior to catalyst light-off during cold start, the catalyst light-off process may be slowed down due to reduced energy release directly inside the catalytic converter. In contrast, if the converter is overdosed with the reactants due to poor thermal oxidation, there may be more emissions breakthrough even though the catalyst may be lit-off slightly faster. As will be discussed in Section 4, the system must be optimized to balance these two oxidation processes in order to maximize the benefits.

3.2 Steady State Experimental Results

Steady state cold-fluid testing was performed to understand the basic effects of secondary air injection on exhaust gas temperatures and emissions. The engine was operated with various spark timings at a fixed condition of 1200 rpm, λ_{engine}= 0.9, and 8.0 g/s intake air flow to the engine. The experiments were repeated with secondary air and nitrogen injection at each operating condition. The physical cooling effects of secondary air were reasonably decoupled from the chemical heating effects by comparing nitrogen injection cases with air injection cases. A set of data for 300 cycles was analyzed for each operating condition.

The net indicated mean effective pressure (Net-IMEP) values were calculated from in-cylinder pressure data acquired from four cylinders. Combustion stability was also quantified and investigated in terms of the coefficient of variation (COV) in Net-IMEP. Figure 3-2 shows the Net-IMEP and the COV in Net-IMEP as a function of spark timing in each case. With increased levels of spark retard, combustion stability deteriorated as combustion occurred in a rapidly expanding cylinder volume.

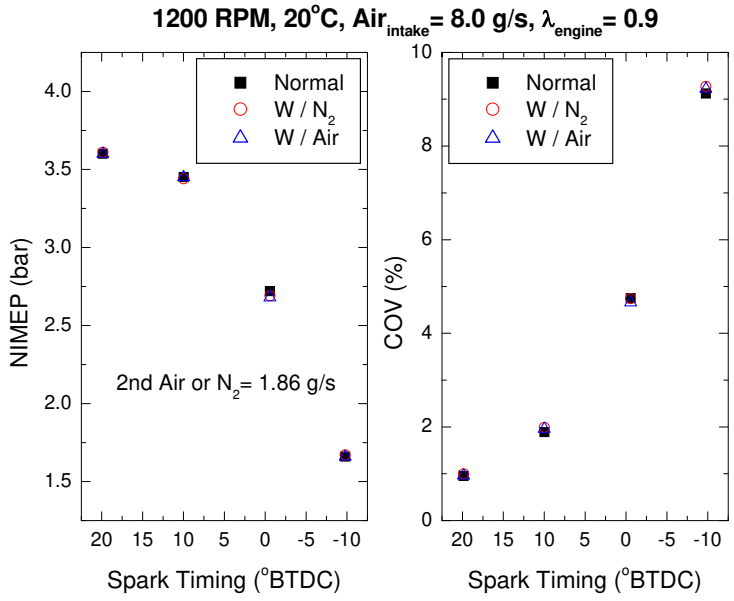

Figure 3-2 Net-IMEP and COV of Net-IMEP as a function of spark timing at 1200 RPM, intake air flow of 8.0 g/s and engine lambda of 0.9 with the 20°C coolant.

The exhaust gas temperatures were observed to increase with spark retard as shown in Figure 3-3. Phasing the combustion process later in the expansion stroke decreased the amount of useful work extracted from the burned gases, resulting in higher exhaust gas temperatures and increased post-flame oxidation rates. Higher exhaust gas temperatures enhanced the initiation of the thermal oxidation reaction as shown in Figure 3-4 and Figure 3-5. Clearly, the advantage with spark retard was higher exhaust gas temperature, resulting from thermal oxidation. This could heat the catalyst more quickly to the light-off temperature during cold start. Therefore, it was concluded that some spark retard was required in the engine start-up experiments with SAI in order to initiate the thermal oxidation reaction in the manifold. The benefit in improving the reaction rate should be examined carefully against the concern with combustion quality with extreme spark retard.

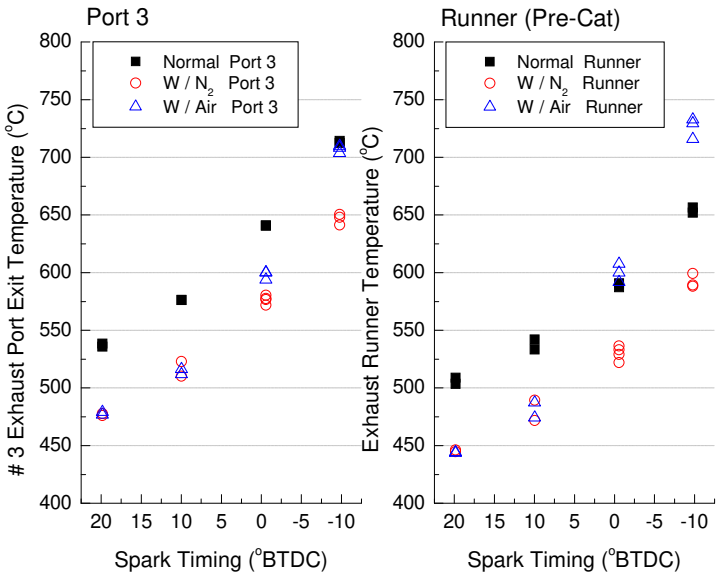

Figure 3-3 Exhaust gas temperatures at the port exit of cylinder #3 and runner as a function of spark timing with the secondary air or nitrogen injection at 1200 RPM, intake air flow of 8.0 g/s and engine lambda of 0.9 with the 20°C coolant.

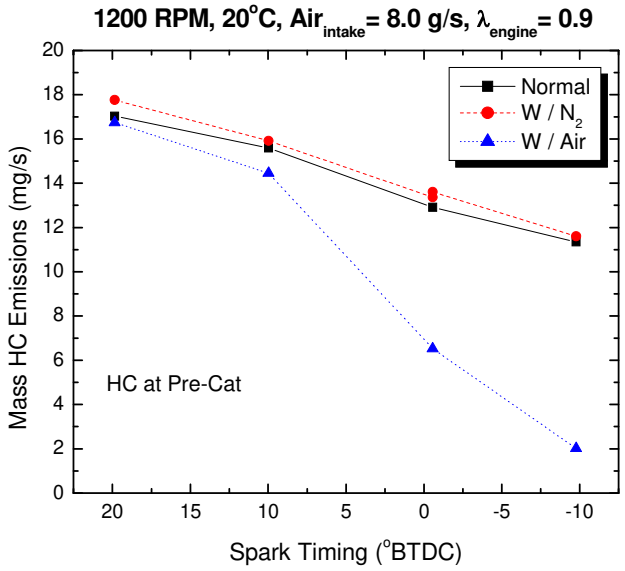

Figure 3-4 **Hydrocarbon mass emissions at the pre-catalyst as a function of spark timing with the secondary air or nitrogen injection at 1200 RPM, intake air flow of 8.0 g/s and engine lambda of 0.9 with the 20°C coolant.**

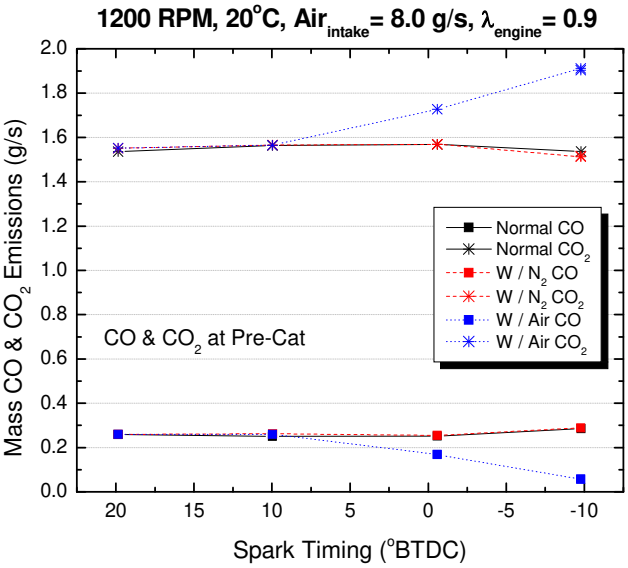

Figure 3-5 **CO and CO_2 mass emissions at the pre-catalyst as a function of spark timing with the secondary air or nitrogen injection at 1200 RPM, intake air flow of 8.0 g/s and engine lambda of 0.9 with the 20°C coolant.**

3.3 Typical Engine Start-up

Engine start-up from ambient conditions is a complicated process that requires delivery of an adequate relative air/fuel ratio around the spark plug gap for a robust combustion event during engine cranking. The engine undergoes severe transients before it reaches the idle speed. Upon the first cylinder firing, the engine accelerates to a speed up to about 1600 RPM, resulting in a rapid decrease in the intake manifold pressure. During the first part of this transient period, spark timing is advanced as engine speed and in-cylinder exhaust gas residuals increase. The engine then decelerates to normal idle speeds during the second part of this transient period; therefore, the intake manifold pressure and spark timing also transition to the idle calibration state. In order to better understand the typical engine start-up behavior, several operating parameters and exhaust emissions were acquired during the first 20 seconds after cranking commenced, as shown in Figure 3-6 and Figure 3-7. A substantial amount of fuel was injected into the cylinder for the first few cycles to prepare the appropriate in-cylinder mixture for robust combustion. Significantly rich in-cylinder mixture conditions and high transient HC concentrations were also observed during the first few seconds.

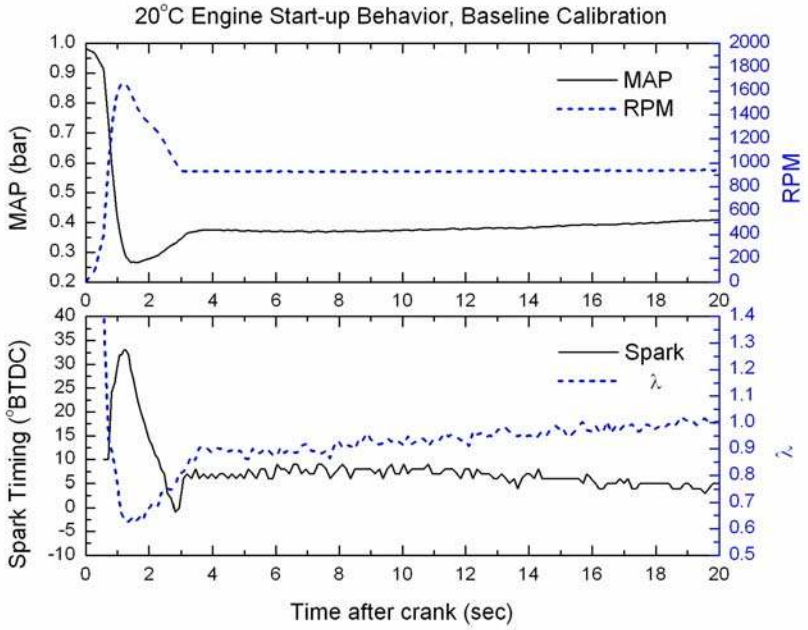

Figure 3-6 Typical start-up calibration MAP, RPM, spark timing, and relative air/fuel ratio as a function of time after crank.

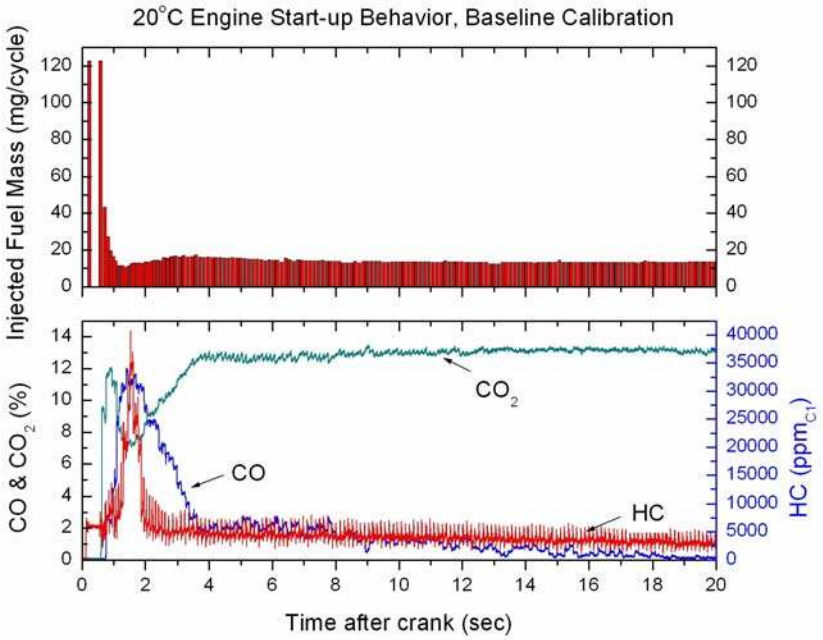

Figure 3-7 Injected fuel masses and exhaust gas emissions measured at the exhaust port exit of cylinder #4 as a function of time after crank with a typical start-up calibration.

During a typical 20°C start-up process, the baseline calibration resulted in an idle speed of 1000 RPM and 6° BTDC spark timing at approximately 3 seconds after the onset of engine cranking. The average Net-IMEP of 2.5 bar with 5% COV was obtained during the quasi-steady idle period of 3-20 seconds.

3.4 Constant Lambda Engine Start-up

3.4.1 Operating Conditions

The continuously varying lambda values with a typical engine calibration during cold start introduce additional complexity in the emissions analysis with the secondary air injection strategy. Thus, in order to perform adequate experiments for the effects of SAI, engine start-up experiments were conducted with three different constant lambda start-up strategies as shown in Figure 3-8. Since the engine operations with the constant lambda trajectories produced relatively constant levels of exhaust emissions, the effects of SAI were more clearly observed with the constant lambda start-up processes. To ensure an equivalent start-up process, the same RPM trajectory, Figure 3-9, was maintained with the different constant lambda histories. This resulted in a reasonably similar Net-IMEP and COV during each start-up operation, as plotted in Figure 3-10 and Figure 3-11. It should be noted that spark timings were retarded to keep the same RPM trajectory with richer engine lambda conditions due to a more robust and stable combustion, allowing for additional spark retard from MBT. Consequently, the same history of inducted air mass was delivered to the cylinders, cycle by cycle, for all three different start-up processes.

General Motors provided the target speed-load point during the park idle period of the FTP (0-15 seconds) for this engine. The baseline calibration produced a Net-IMEP of 2.5 bar and 1000 RPM with 0.45 bar MAP and 6^{o}BTDC spark timing. However, the idle speed of these experiments was raised to 1450 RPM in order to provide a higher rate of thermal energy to the catalyst. Therefore, the engine was calibrated to achieve the target operating condition for the park idle period, 2.0 bar Net-IMEP and 1450 RPM. All engine start-up tests were conducted with Indolene (UTG-91, Table 2-2) at approximately 20^{o}C environmental conditions. The coolant temperature was initially fixed at 20^{o}C by the external coolant control system.

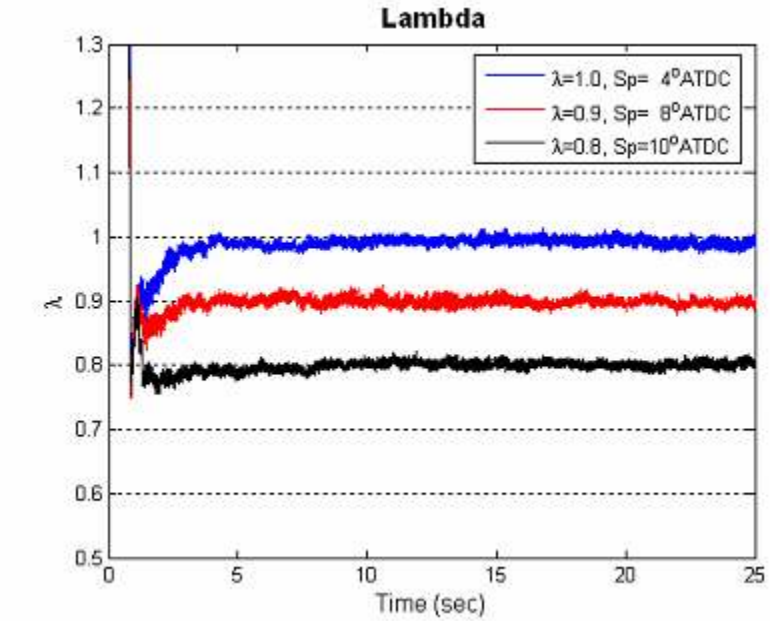

Figure 3-8 Lambda trajectories for three constant lambda start-up processes as a function of time after cranking.

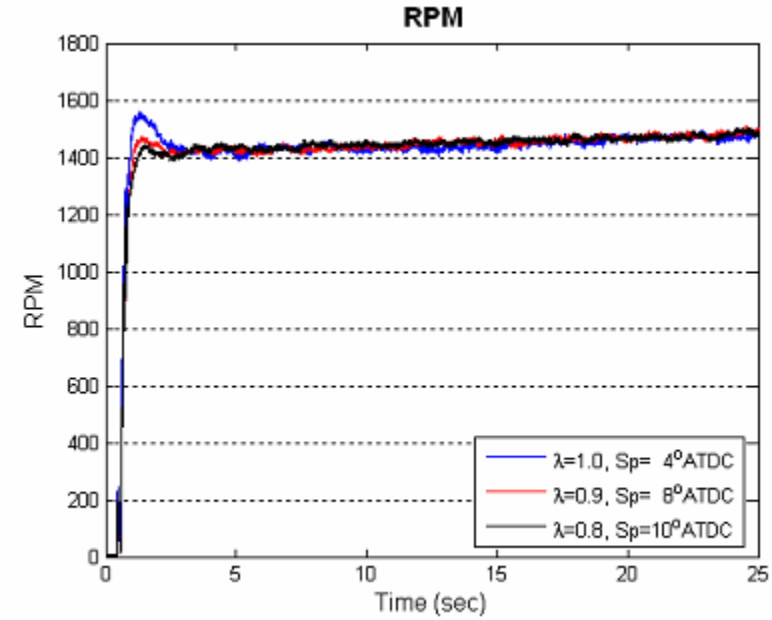

Figure 3-9 RPM trajectories for three constant lambda start-up processes as a function of time after cranking.

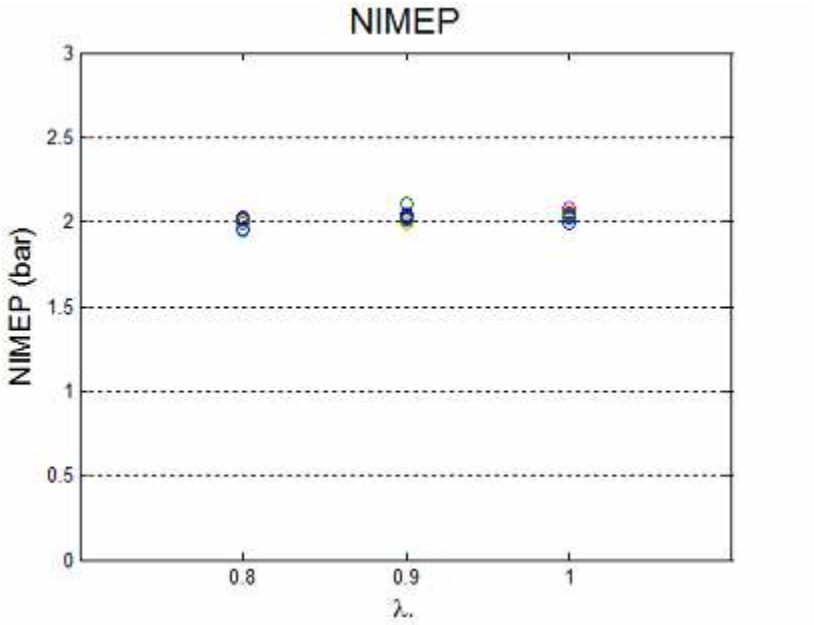

Figure 3-10 Net-IMEP of cycle no. 21-300 during cold start as a function of engine lambda.

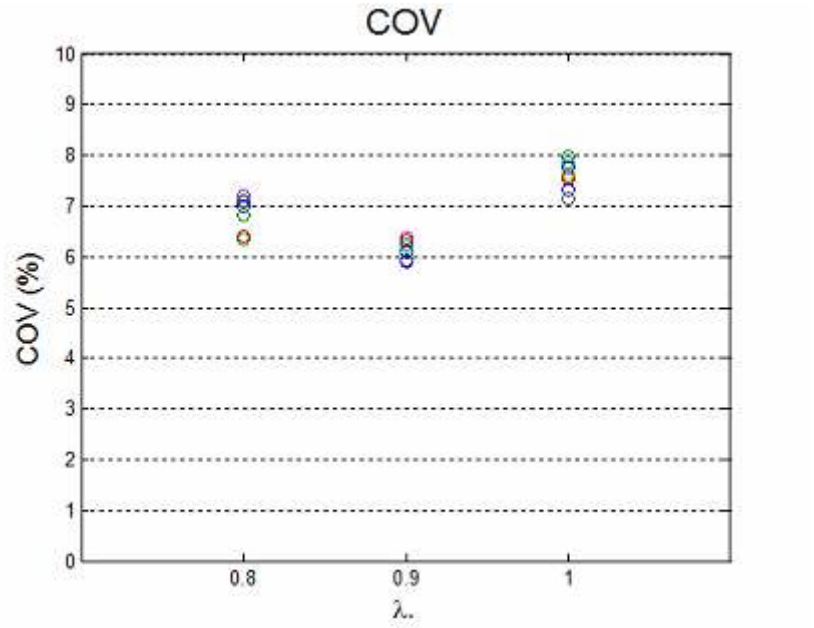

Figure 3-11 COV in Net-IMEP of cycle no. 21-300 during cold start as a function of engine lambda.

3.4.2 Test Matrix

The test matrix, shown in Table 3-1, was designed for various secondary air injection flow rates and engine lambda conditions in order to investigate the effects of SAI on exhaust emissions and catalyst light-off characteristics. The results of these tests are discussed in Section 4 and 5.

Table 3-1 Test matrix for the constant lambda start-up strategies with different levels of SAI.

SAI / Lambda	3.63(g/s)	7.26 (g/s)	10.89 (g/s)
0.8			
0.9			
1.0			
SAI % to normal intake air mass flow	33%	67%	100%

3.5 Exhaust Gas Composition

3.5.1 Exhaust Gas Stoichiometry Overview

The most accurate approach for burned mixture property and composition calculations is to use a thermodynamic equilibrium program at temperatures above about 1700 K and to assume a frozen composition below 1700 K due to the following mechanisms. At high temperatures (e.g., during combustion and the early part of the expansion stroke) the burned gas composition corresponds closely to the equilibrium composition at the local temperature, pressure, and equivalence ratio. During the expansion process, recombination reactions simplify the burned gas composition. However, late in the expansion stroke and during exhaust blowdown, the recombination reactions are unable to

maintain the gases in chemical equilibrium and therefore, in the exhaust process, the composition becomes frozen [1].

Exhaust gas composition depends on the relative proportion of fuel and air fed to the engine, fuel composition, and completeness of combustion. These relationships can be used to determine the operating fuel/air equivalence ratio of an engine from a knowledge of its exhaust gas composition. For fuels comprised of carbon and hydrogen only, a carbon balance air/fuel ratio can be employed by the use of measured carbon based species (HC, CO, CO_2) and a water-gas shift reaction constant, K = 3.5, which is commonly used for normal engine operating conditions. Varying K from 2.5 to 4.5 produces a negligible difference in the computed lambda. However, the same range of K variation results in sizable differences in hydrogen and water concentrations, which will affect the calculation of exhaust gas enthalpy.

3.5.2 UEGO Sensor Output

A UEGO (Universal Exhaust Gas Oxygen) sensor was used to measure a wide range of air/fuel ratios in this experimental work. This UEGO sensor operates over all ranges of air/fuel ratios, unlike a conventional oxygen sensor which provides reliable measurements only near the stoichiometric point.

The UEGO sensor is made of three solid zirconia substrates. The first substrate is the oxygen pumping cell. The second is the oxygen galvanic cell element, and the third substrate is the wall that composes the oxygen reference cavity. Pt electrodes are printed on both the first and second solid zirconia substrate element, composing the I_p cell and the V_s/I_{cp} cell. By pumping oxygen, the I_p cell controls the partial oxygen pressure in the detecting cavity, which is surrounded by the inner electrode of the I_p cell and the V_s/I_{cp} cell. The V_s/I_{cp} cell made from the oxygen galvanic cell element works as a conventional oxygen sensor, but without any reference oxygen from atmosphere. By supplying a very small constant pumping current I_{cp} to the V_s/I_{cp} cell, oxygen is pumped to the reference oxygen cavity from the detecting cavity, resulting in a constant self-generated oxygen partial pressure in the cavity. The pumping current I_p is controlled by using a feedback circuit to maintain the V_s cell voltage at 450 mV [7].

The output of the UEGO sensor, the pumping current I_p, can be expressed as a sum of two current components as follows.

$$I_p = I_p^{lean} + I_p^{rich} \tag{3.1}$$

where I_p^{lean} is a positive current proportional to the partial pressure of oxygen in the exhaust gas, and I_p^{rich} is a negative current proportional to the partial pressures of the combustible gases, e.g., hydrocarbons, hydrogen and carbon monoxide. Under normal combustion without fuel reforming, I_p^{rich} can be ignored for lean combustion conditions since the concentrations of hydrogen and carbon monoxide in the exhaust gas are insignificant and I_p^{rich} is approximately equal to zero as a result. On the other hand, the pumping current I_p is approximately equal to I_p^{rich} for rich combustion conditions since oxygen concentration in the exhaust is negligible, resulting in I_p^{lean} approximately equal to zero. Also, it can be equivalently thought that the I_p^{lean} and I_p^{rich} are proportional to the amount of oxygen in the exhaust gas and to the amount of oxygen required for the complete combustion reaction of the combustible gases in the exhaust gas respectively.

Thus, for normal combustion, the pumping current corresponds to the air/fuel ratio in the exhaust gas, i.e., $I_p = I_p^{lean} > 0$, $I_p^{rich} = 0$ under a lean combustion condition, and $I_p = I_p^{rich} < 0$, $I_p^{lean} = 0$ under a rich combustion condition. However, the sensitivities of I_p^{lean} for various oxygen concentrations and I_p^{rich} for various combustible gas concentrations are not the same. In fact, it is observed that the sensitivity of I_p^{lean} is about four times less than that of I_p^{rich} around the stoichiometric air/fuel ratio. This is due to the fact that the diffusion rates of hydrogen, carbon monoxide and oxygen inside the sensor are different. For example, carbon monoxide has a mass very similar to oxygen and so both molecules diffuse equally rapidly through the porous layer of the sensor while hydrogen has a much higher rate of diffusion compared with oxygen. Thus, if non-negligible combustible gases, such as carbon monoxide and hydrogen, exist in a lean combustion condition, I_p^{rich} no longer can be ignored. An excess of oxygen (more oxygen than required for complete combustion of the combustible gases due to a higher diffusion rate of hydrogen) is required to compensate the negative current I_p^{rich} owing to the carbon monoxide and hydrogen concentrations in the

porous layer, resulting in a lower pumping current I_p than what would be without the combustible gases. The result is that air/fuel ratio reading from the sensor is lower than the true air/fuel ratio in the exhaust gas. Due to the significant levels of combustible gases (HC, CO and H_2) in the overall lean mixture of engine-out exhaust gas and secondary air, the UEGO lambda reading values could be significantly different from the actual lambda values in the experimental work, as described above.

UEGO sensors are normally calibrated for the typical exhaust gas at fully warmed-up engine conditions. Lambda reading values are acquired from corresponding I_p values based on the ideally calibrated lambda-I_p curve. Since lambda reading values were acquired from a Horiba MEXA-700 analyzer, the output values of UEGO pumping current were estimated by matching the lambda reading values to the ideally calibrated lambda-I_p curve shown in Figure 3-12. These I_p values were then inserted into Equation (3.2), which replaced the water-gas shift reaction equation in the exhaust gas composition calculation.

$$I_p = -k_{H_2} \cdot \tilde{x}_{H_2} - k_{CO} \cdot \tilde{x}_{CO} - k_{HC} \cdot \tilde{x}_{HC} + k_{O_2} \cdot \tilde{x}_{O_2} \tag{3.2}$$

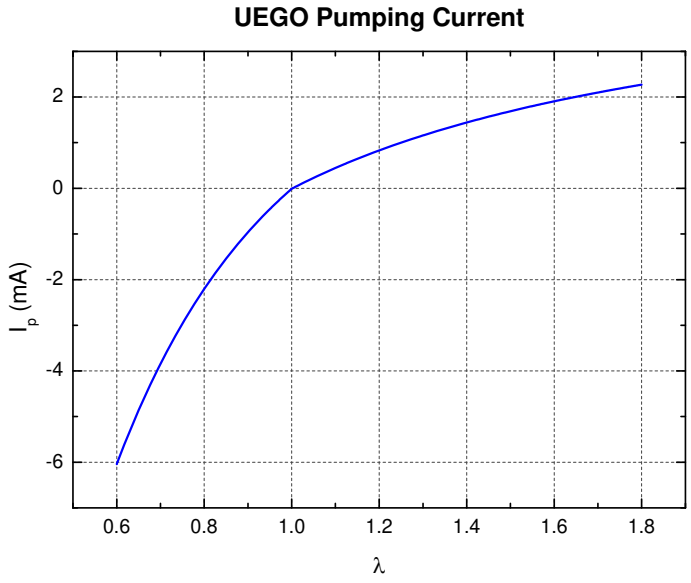

Figure 3-12 UEGO sensor pumping current characteristics, I_p as a function of engine lambda.

3.5.3 Composition Calculation

A general formula for the composition of fuel can be represented as $C_nH_mO_r$. For conventional petroleum-based fuels, oxygen is absent. Since Indolene (UTG-91) also has no oxygen in its composition, CH_y (c.f. y = m/n) was used for the following combustion reactions. The overall combustion reaction can be written explicitly as:

$$\begin{aligned} & CH_y + n_{O_2} \cdot (O_2 + 3.773 \cdot N_2) \\ & + n_r \cdot \{\tilde{x}'_{CO_2} \cdot CO_2 + \tilde{x}'_{CO} \cdot CO + \tilde{x}'_{CH_y} \cdot CH_y + \tilde{x}'_{H_2O} \cdot H_2O + \tilde{x}'_{NO} \cdot NO + \tilde{x}'_{H_2} \cdot H_2 + \tilde{x}'_{N_2} \cdot N_2 + \tilde{x}'_{O_2} \cdot O_2\} \\ & \Rightarrow n_p \cdot \{\tilde{x}_{CO_2} \cdot CO_2 + \tilde{x}_{CO} \cdot CO + \tilde{x}_{CH_y} \cdot CH_y + \tilde{x}_{H_2O} \cdot H_2O + \tilde{x}_{NO} \cdot NO + \tilde{x}_{H_2} \cdot H_2 + \tilde{x}_{N_2} \cdot N_2 + \tilde{x}_{O_2} \cdot O_2\} \end{aligned} \tag{3.3}$$

n_{O_2} : moles of O_2 per mole CH_y

n_r : moles of residual gas per mole CH_y

n_p : moles of exhaust products per mole CH_y

$\tilde{x}'$: mole fraction of residual gas component

$\tilde{x}$: mole fraction of exhaust gas component

A residual gas fraction model was combined with this combustion equation in order to provide the mole fraction of residual gas. Throughout the calculation, it has been assumed that the unburned hydrocarbons have the same H/C ratio as the fuel. Since NO_x concentrations are usually sufficiently low during the cold start-up process, NO and NO_2 were neglected for this gas composition calculation.

Combining Equation (3.2) with five equations from the atomic balance for each element (C, H, O, N) and the definition of mole fraction (mole fractions add up to 1), the exhaust gas composition was successfully calculated as shown in Figures 3-13~3-15. A carbon balance air/fuel ratio was also derived from this exhaust gas composition. It was found that the lambda reading values from the UEGO sensor were significantly different from the actual exhaust lambda values with SAI due to non-negligible HC, CO and H_2

concentrations in the overall lean mixture of engine-out exhaust gas and secondary air as shown in Figure 3-16. However, as the engine block and exhaust manifold were warmed up, the differences between UEGO reading and actual lambda values decreased, mainly due to the significant post oxidation with SAI upstream of the UEGO sensor, in which case the gas more closely resembled the ideal calibration condition for the sensor.

$$\frac{A}{F} = \frac{M_{air}}{M_{fuel}}\left[\frac{W}{C_t} + \left(\frac{C_T' W - C_T W'}{C_T}\right)\cdot n_r - \frac{y}{2}\right] \tag{3.4}$$

$$C_T = \tilde{x}_{CO_2} + \tilde{x}_{CO} + \tilde{x}_{CH_y}$$

$$C_T' = \tilde{x}'_{CO_2} + \tilde{x}'_{CO} + \tilde{x}'_{CH_y}$$

$$W = 1 - \frac{1}{2}\tilde{x}_{CO} + \frac{1}{2}\tilde{x}_{H_2O} + \left(\frac{y}{2} - \frac{1}{n}\right)\tilde{x}_{CH_y}$$

$$W' = 1 - \frac{1}{2}\tilde{x}'_{CO} + \frac{1}{2}\tilde{x}'_{H_2O} + \left(\frac{y}{2} - \frac{1}{n}\right)\tilde{x}'_{CH_y}$$

M_{air}, M_{fuel} : molecular weight

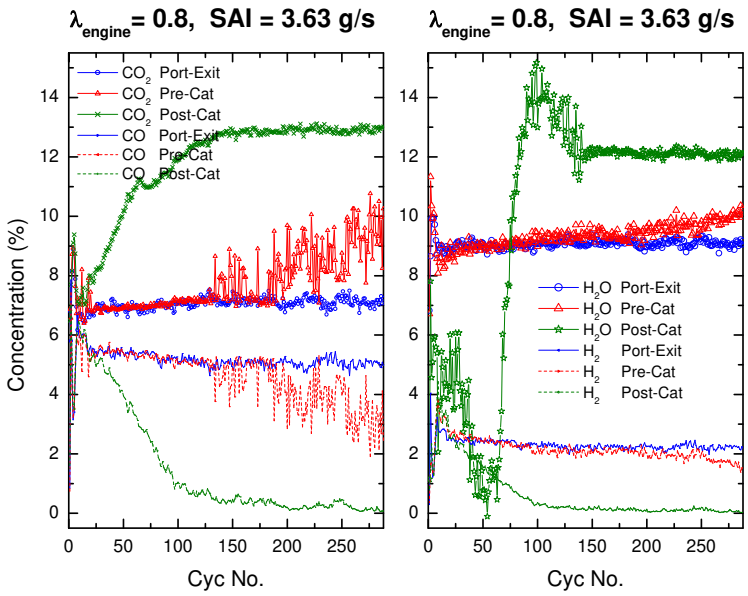

Figure 3-13 Cycle-averaged CO, CO_2, H_2 and H_2O concentrations as a function of cycle number at various locations in the exhaust system (λ_{engine} = 0.8, SAI = 3.63 g/s).

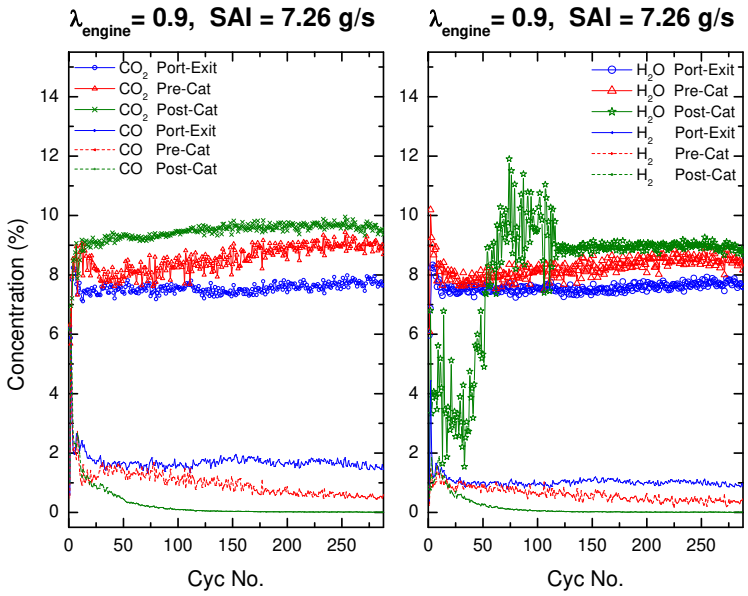

Figure 3-14 Cycle-averaged CO, CO_2, H_2 and H_2O concentrations as a function of cycle number at various locations in the exhaust system (λ_{engine} = 0.9, SAI = 7.26 g/s).

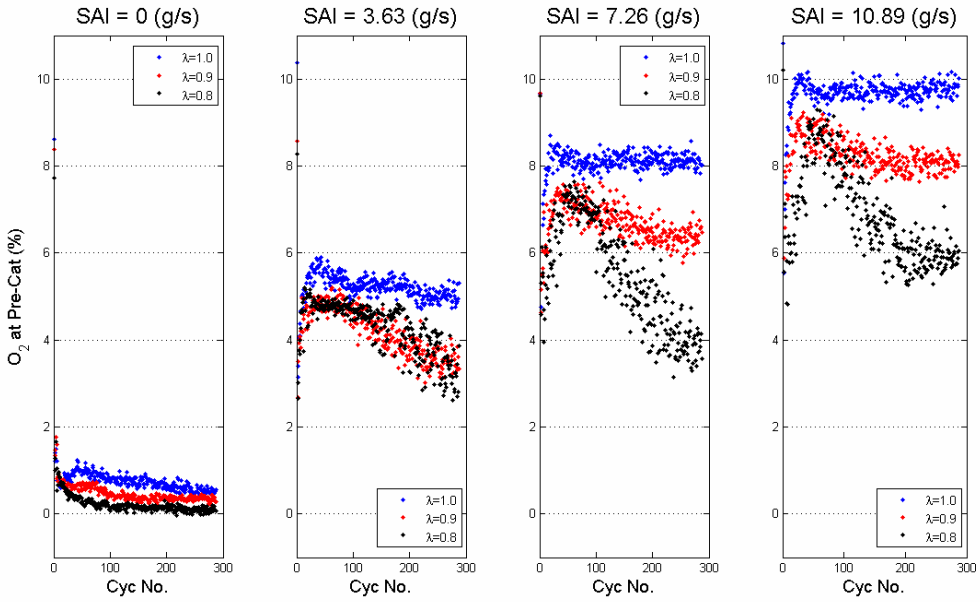

Figure 3-15 Cycle-averaged O_2 concentrations as a function of cycle number at the pre-catalyst with different levels of SAI and engine lambda.

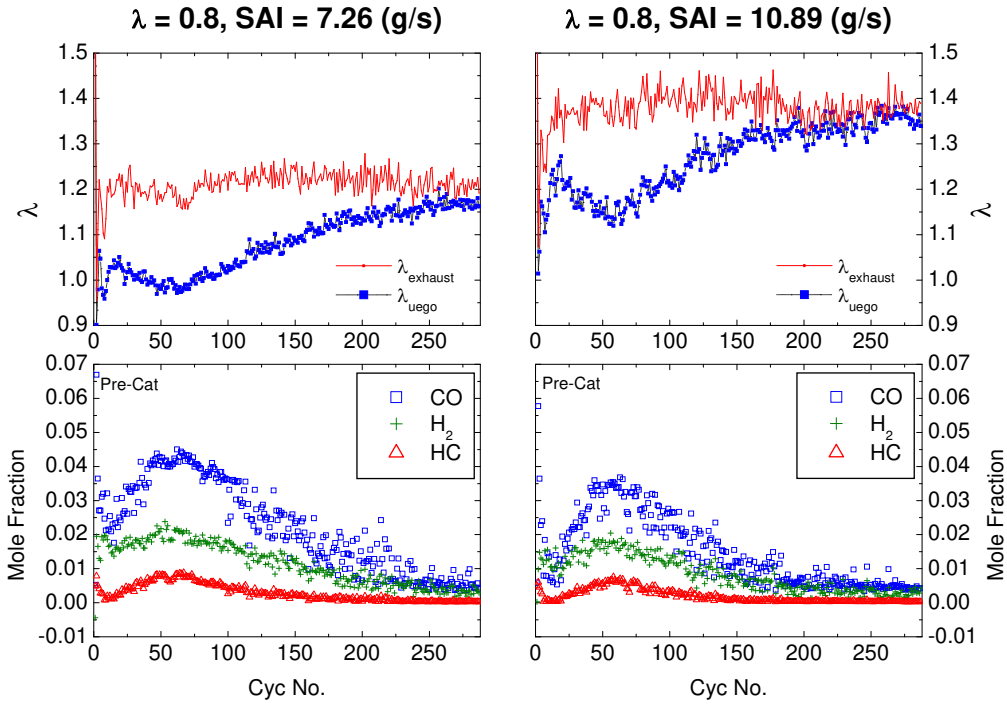

Figure 3-16 Differences between UEGO lambda values and calculated lambda values due to the significant levels of combustible gases in an overall lean mixture.

3.5.4 Quenching Experiments

In order to determine the extent of HC, CO and H_2 oxidation within the exhaust port, gas emissions at the cylinder exit were investigated using exhaust quenching experiments. Exhaust gas reactions were frozen by rapidly reducing exhaust gas temperatures at the exit plane of the exhaust valves with cold N_2. Experiments were performed using a fixed N_2 injection flow rate that was optimized for a stable and repeatable injection event. The amount of quenching gas was increased until cylinder-exit HC emissions were found to reach a plateau. Results from the quenching experiments provided exhaust gas emissions at the cylinder exit as shown in Figures 3-17~3-22. These initial conditions and compositions were used to drive the exhaust plug flow heat transfer model, which is discussed in Section 5.

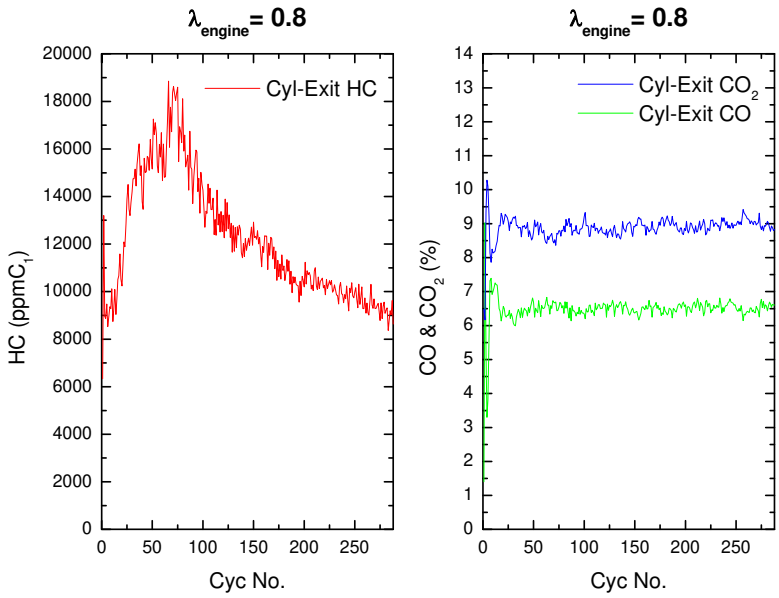

Figure 3-17 Measured HC, CO and CO_2 concentrations at the cylinder exit as a function of cycle number (λ_{engine} = 0.8).

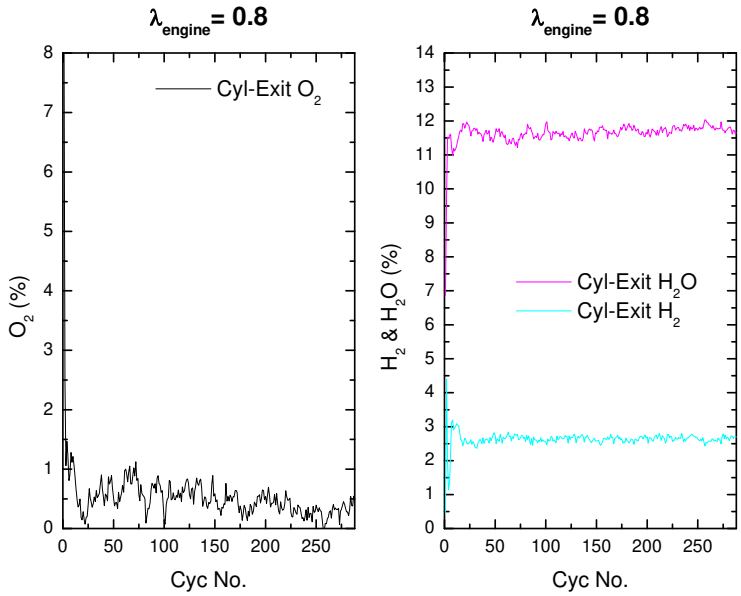

Figure 3-18 Calculated O_2, H_2 and H_2O concentrations at the cylinder exit as a function of cycle number ($\lambda_{engine} = 0.8$).

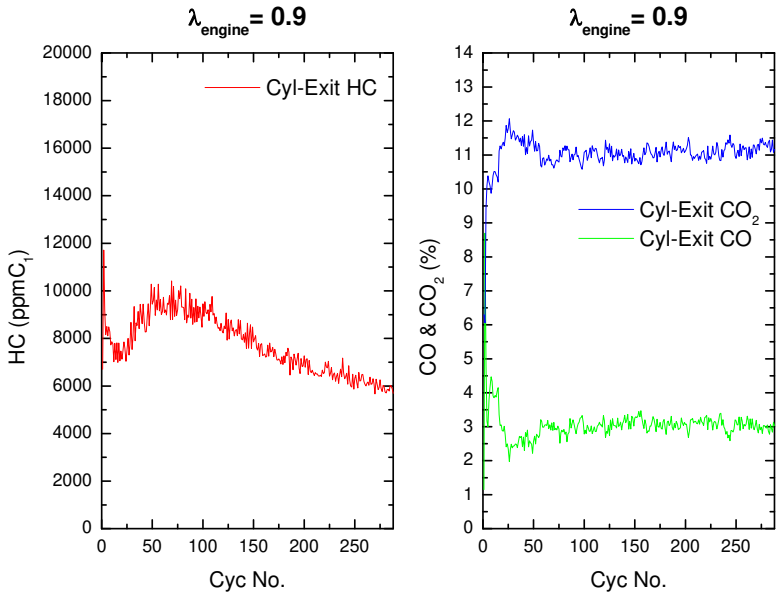

Figure 3-19 Measured HC, CO and CO_2 concentrations at the cylinder exit as a function of cycle number ($\lambda_{engine} = 0.9$).

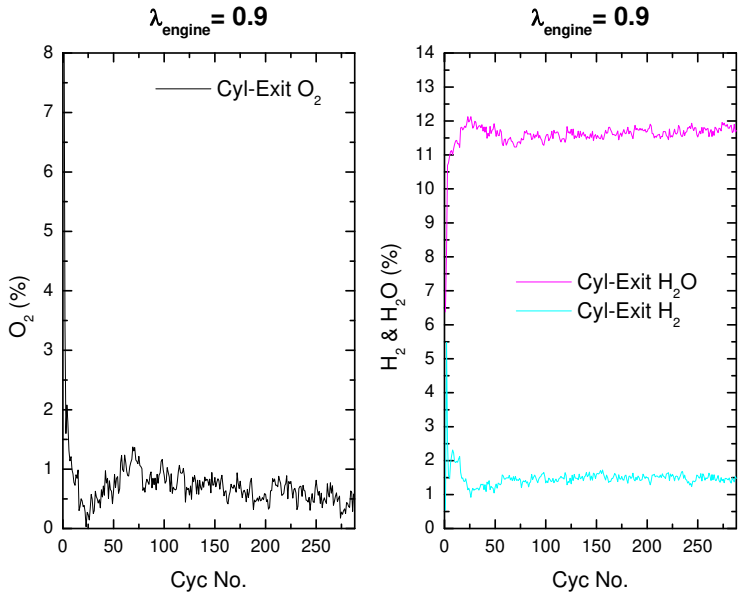

Figure 3-20 Calculated O_2, H_2 and H_2O concentrations at the cylinder exit as a function of cycle number ($\lambda_{engine} = 0.9$).

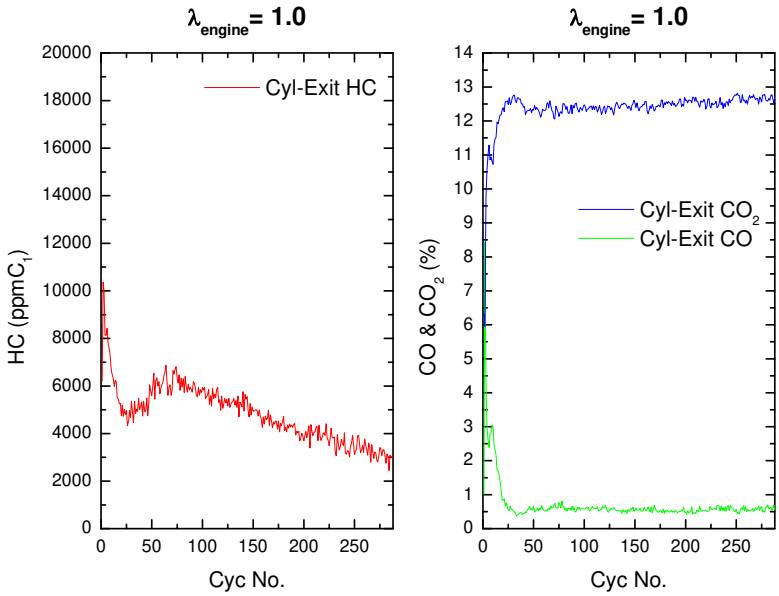

Figure 3-21 Measured HC, CO and CO_2 concentrations at the cylinder exit as a function of cycle number ($\lambda_{engine} = 1.0$).

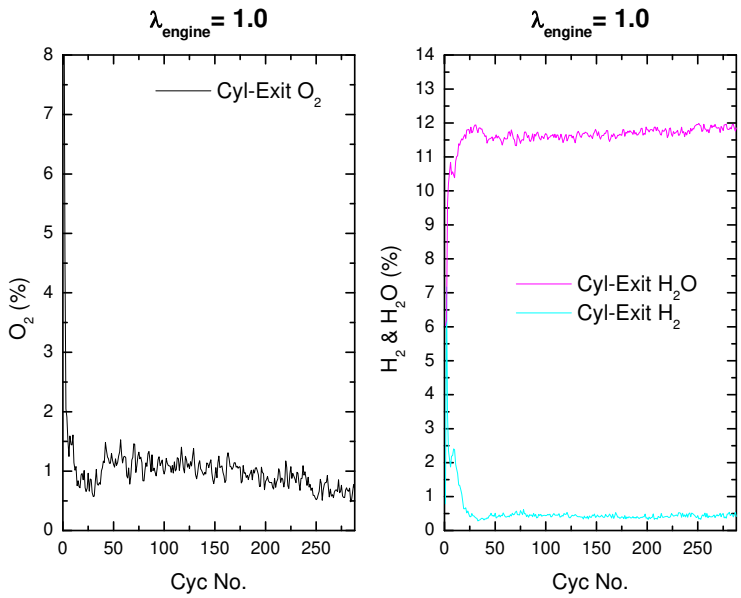

Figure 3-22 Calculated O_2, H_2 and H_2O concentrations at the cylinder exit as a function of cycle number ($\lambda_{engine} = 1.0$).

Chapter 4

Analysis of Exhaust Emissions

4.1 Exhaust Mass Flow Rate

4.1.1 Time-resolved HC Concentration

Hydrocarbon concentrations were measured with a fast-response flame ionization detector (FFID). The FFID measures total HC concentrations with a 10-90 % response time of approximately 1 ms. This very fast response time permitted the observation of the HC variations occurring during the engine cycle. To better understand exhaust system oxidation, time-resolved HC concentrations were recorded at each exhaust port exit, 8 cm from the exhaust valves. Figure 4-1 and Figure 4-2 shows the cylinder #1 port exit hydrocarbon concentrations as a function of crank angle for three different constant lambda start-up processes. The details of the HC variations during the engine cycle were related to the exhaust flow behavior. Before exhaust valve opening (EVO), the sample was drawn from a stagnant volume of gas giving a constant signal. At the time of EVO, an initial peak was observed during the blowdown phase as head gasket, spark plug, and valve seat crevice gases were exhausted. As the blowdown process continued, there was a rapid decrease in HC concentration as the bulk of the burned gas was expelled. After the blowdown flow, the brief flow reversal period caused the tail-end of the previous slug of hydrocarbons to move backward and forward around the sampling point and contributed to the following small peak [19]. As in-cylinder pressure equilibrated during the exhaust displacement period, an increase in HC levels was observed due to several possible mechanisms: release of hydrocarbons from the piston top land crevice and out-gassing of hydrocarbons from lubricant on the liner and in-cylinder deposits. Towards the end of the exhaust stroke, the concentration increased and constituted another peak as the hydrocarbons in the ‘roll-up’ vortex between the rising piston and the liner were expelled. This was followed by a brief

period of back flow during valve overlap prior to exhaust valve closing (EVC). After EVC, the gas was stagnant and the signal remained constant until another cycle.

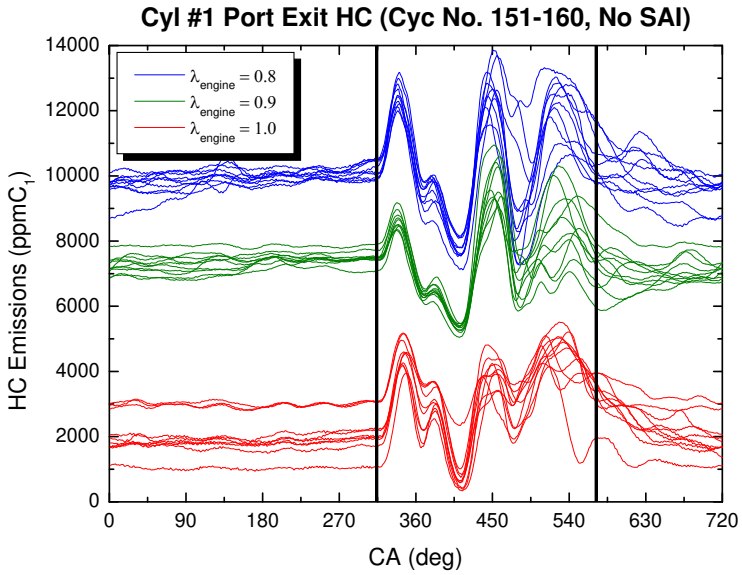

Figure 4-1 Cylinder #1 port exit HC concentrations as a function of crank angle for three different constant lambda start-up processes (cyc no. 151-160).

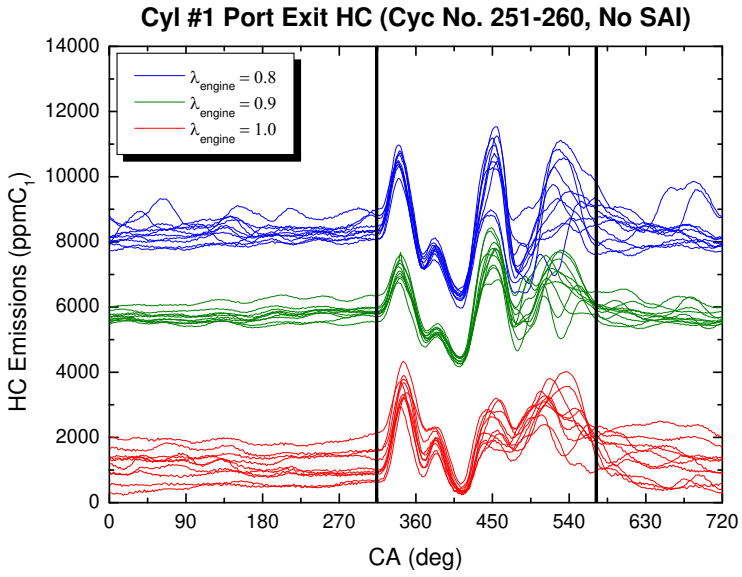

Figure 4-2 Cylinder #1 port exit HC concentrations as a function of crank angle for three different constant lambda start-up processes (cyc no. 251-260).

4.1.2 Instantaneous Exhaust Mass Flow Rate Model

Since the exhaust gas was highly diluted by the secondary air, the gas concentration was not a proper indication of emission levels. Thus, an instantaneous exhaust mass flow rate model was developed to evaluate mass based emission levels. The time-resolved mass emissions were achieved from weighting the instantaneous emission concentrations by the instantaneous exhaust mass flow rate.

The mass flow rate through the exhaust valve was calculated from the equation for compressible flow through a flow restriction. A set of equations was derived from a one-dimensional flow analysis assuming that the flow was a quasi-steady, adiabatic and isentropic flow of a perfect gas, and then real gas flow effects were included by the use of a discharge coefficient C_D. The experimental data based on valve lift to diameter ratios were used to determine the valve discharge coefficient. Equation (4.1) was used when the pressure ratio across the valve exceeded the critical value. Equation (4.2) was used when the pressure ratio was less than the critical value.

$$if \qquad \left(\frac{P_{EXH}}{P_{CYL}}\right) \le \left(\frac{2}{\gamma+1}\right)^{\frac{\gamma}{\gamma-1}}$$

$$\dot{m}_{EXH} = \frac{C_D A_R P_{CYL}}{\sqrt{\gamma R T_{CYL}}} \gamma \left(\frac{2}{\gamma+1}\right)^{\frac{\gamma+1}{2(\gamma-1)}} \tag{4.1}$$

$$if \qquad \left(\frac{P_{EXH}}{P_{CYL}}\right) > \left(\frac{2}{\gamma+1}\right)^{\frac{\gamma}{\gamma-1}}$$

$$\dot{m}_{EXH} = \frac{C_D A_R P_{CYL}}{\sqrt{\gamma R T_{CYL}}} \gamma \left\{ \frac{2}{\gamma-1} \left[\left(\frac{P_{EXH}}{P_{CYL}}\right)^{\frac{2}{\gamma}} - \left(\frac{P_{EXH}}{P_{CYL}}\right)^{\frac{\gamma+1}{\gamma}} \right] \right\}^{\frac{1}{2}} \tag{4.2}$$

The compressible flow model applied the orifice flow equations to the flow across the exhaust valve using the measured cylinder pressure and calculated cylinder gas temperature for upstream stagnation conditions. The kinetic energy in the cylinder was assumed negligible and, therefore, the stagnation pressure and temperature were equal to the in-cylinder pressure and temperature [20]. The calculation was started at the instant prior to exhaust valve opening and, using the ideal gas law, the initial cylinder gas temperature was calculated from known quantities. These known quantities were cylinder volume (from engine geometry), pressure (from measurement), mass (from measured flow rate and calculated residual fraction) and gas stoichiometry.

From this initial state, the instantaneous temperature of the cylinder gas at the next crank angle was subsequently determined from the ideal gas relationship by combining the measured cylinder pressure and instantaneous exhaust mass flow rate. During the valve overlap period, the exhaust gas flows back into the cylinder. Since the engine in this experimental work had a relatively small valve overlap period (approximately 10 CA), this back flow was largely affected by the piston motion. To accurately determine the exhaust port and cylinder residuals, this back flow was accounted for by assuming a plug flow into the cylinder. Fox's model [21] was used to estimate the residual gas fraction during the engine start-up process since the model is applicable for low to medium engine speeds where the cylinder pressure does not substantially differ from the exhaust port pressure at IVO. In the model, the contribution of the back flow from the exhaust port to the cylinder during the valve overlap period is accounted for explicitly in terms of a valve overlap factor. Section B in the Appendix provides additional detailed information regarding the residual gas fraction.

Figure 4-3 and Figure 4-4 show the instantaneous exhaust mass flow rates and the calculated cylinder gas temperatures as a function of crank angle for three different periods of a cold start operation (cycle no. 41-50, 141-150, 241-250). The cylinder gas temperature falls rapidly during blowdown and continues to fall during the exhaust stroke due to heat transfer to the cylinder walls. In general, the characteristics of the cylinder gas temperatures during the exhaust process was similar for each cycle period, but the overall levels of gas temperatures increased at later cycle periods due to the increased engine block temperatures.

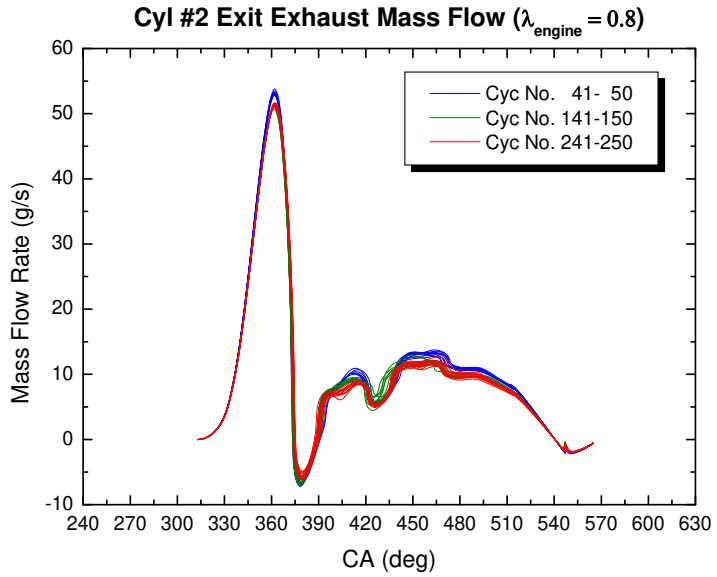

Figure 4-3 Exhaust gas mass flow rates of cylinder #2 as a function of crank angle for three different periods of a cold start operation (cycle no. 41-50, 141-150, 241-250).

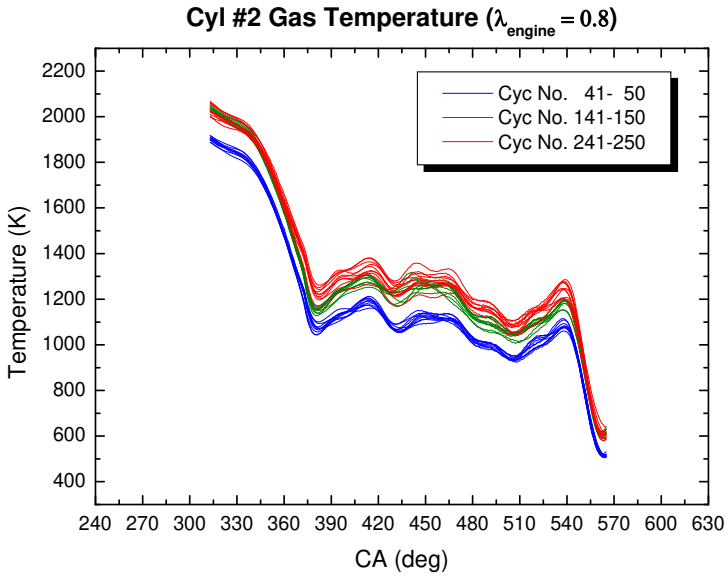

Figure 4-4 Gas temperatures of cylinder #2 as a function of crank angle for three different periods of a cold start operation (cycle no. 41-50, 141-150, 241-250).

4.1.3 Mass Flow Rate Model Validation

The exhaust mass flow model was validated with experimental data over a wide range of secondary air flow rates. Time-resolved HC, CO and CO_2 concentration data from the fast-response analyzers were combined with the exhaust mass flow model, yielding time-resolved mass flow rates. To evaluate the time-resolved mass emissions, care must be taken to account for both the sampling system delay and the gas displacement effect caused by the finite distance of the sample inlet from the cylinder exit. Therefore, this phase delay at each sampling location was corrected for the calculation of exhaust mass emissions by considering the transport time within the exhaust and sampling system and a characteristic response time associated with the analyzer.

In order to validate the exhaust mass flow rate model, cumulative carbon mass emissions were evaluated from the first 25 seconds of operations following engine cranking as shown in Figure 4-5 and Figure 4-6. By the use of the instantaneous exhaust mass flow rate model, agreement within 1.5% was achieved between the carbon mass emissions without SAI and those with different levels of SAI at each sampling point.

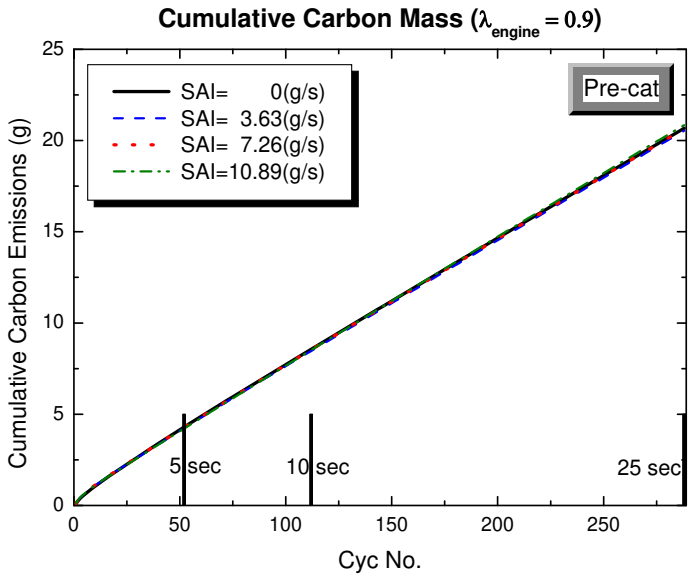

Figure 4-5 Cumulative carbon mass emissions without SAI and with different levels of SAI at the pre-catalyst.

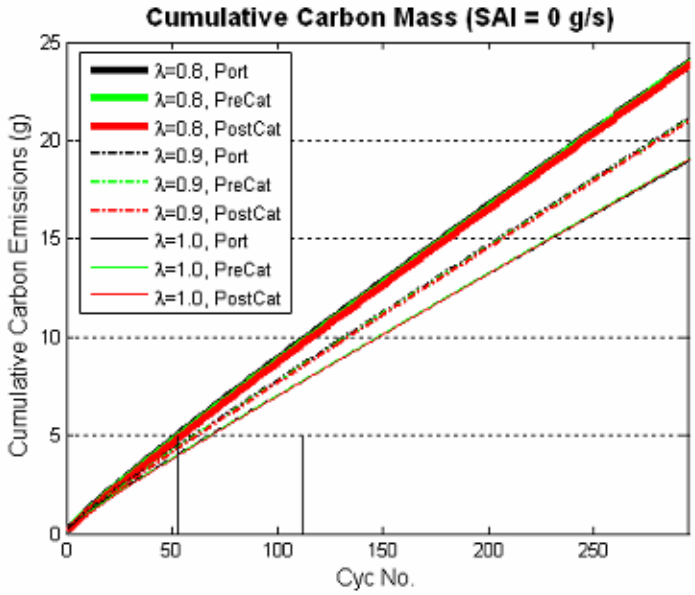

Figure 4-6 Cumulative carbon mass emissions at various locations in the exhaust system with different constant engine lambda operations.

4.2 Trapped HC and Condensed H_2O in Catalyst

HC storage and water condensation characteristics inside the catalytic converter were investigated to more precisely quantify mass emissions and the thermal states of the exhaust gas.

The trapping of HC is a property which catalysts themselves exhibit. Immediately after starting the engine, hydrocarbons (especially the heavier ones) adsorb onto the cold catalyst surface. This is known as the storage period. As the catalyst continues to heat up, but before light-off has been reached, the stored hydrocarbons desorb and then escape unoxidized. This is known as the release period. Figure 4-7 shows the amount of HC trapped in the catalyst with different secondary air injection rates. As the secondary air injection rate was increased, the amount of stored HC was decreased and the time for the storage and release period was also shortened considerably.

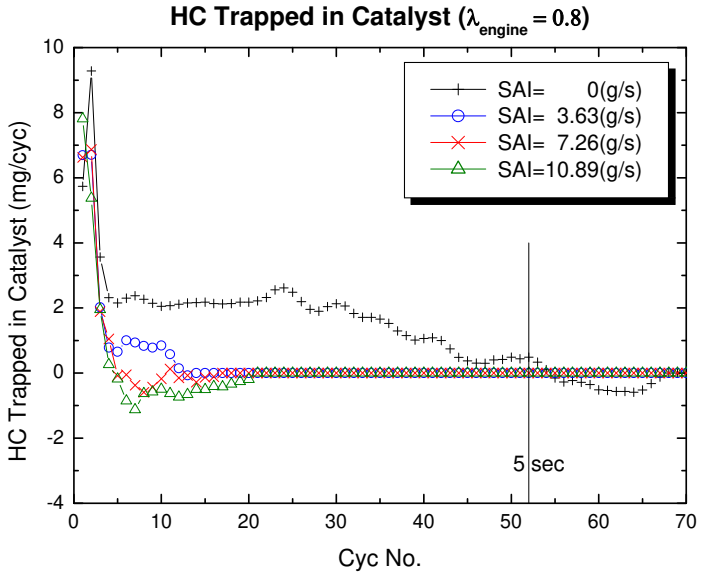

Figure 4-7 HC mass trapped inside the catalyst as a function of cycle number with different levels of SAI.

Due to the initially cold condition and the large surface area of the cells within the catalyst bricks, the exhaust gas temperature dropped significantly through the catalytic converter during cold start. A noticeable amount of water was also condensed inside the catalytic converter. It was found that quantification of condensed water inside the catalyst was required to precisely evaluate mass emissions and thermal states of exhaust gas due to the relatively low energy level of water at a given temperature. The amount of water condensed inside the catalyst was calculated from the pre-catalyst and post-catalyst HC, CO and CO_2 concentrations, as shown in Figure 4-9 and Figure 4-10. The time period of water condensation and its evaporation was shortened noticeably as the secondary air injection rate was increased. Since the exhaust gas flow forced condensed water out from the tilted catalytic converter, the amount of water condensed and evaporated did not add up to zero.

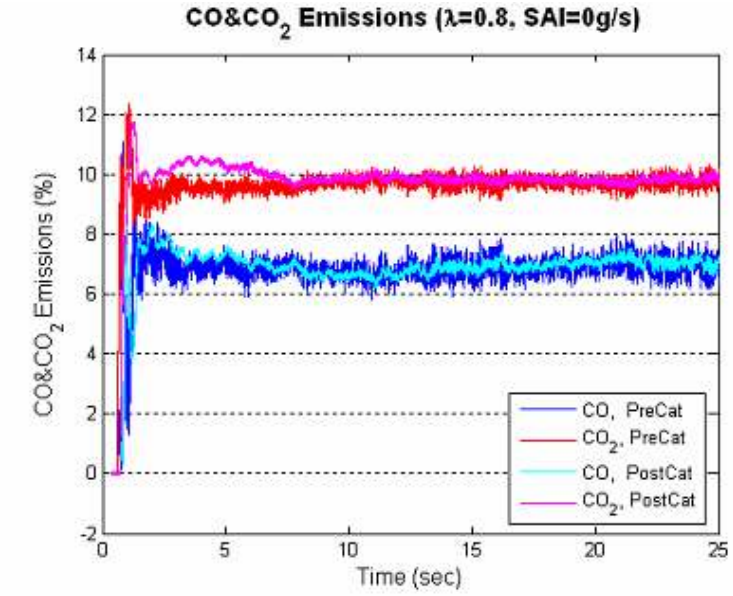

Figure 4-8 CO and CO_2 concentrations at the pre-catalyst and post-catalyst with an engine lambda of 0.8 and no SAI.

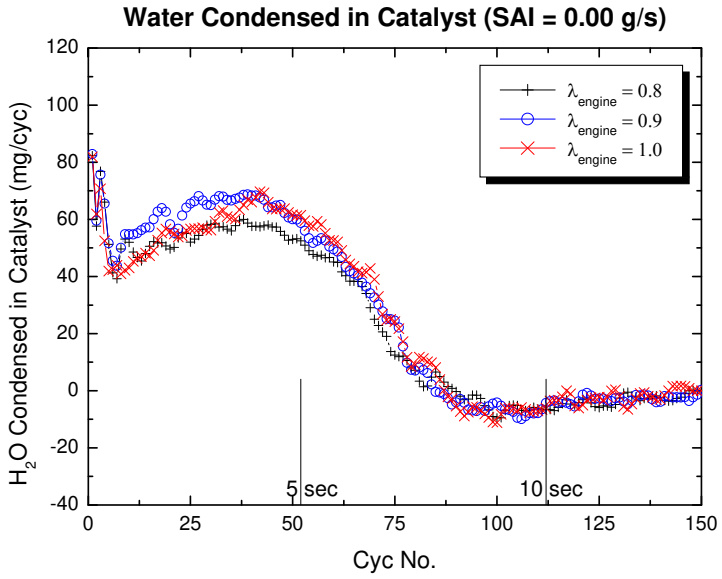

Figure 4-9 Water mass condensed inside the catalyst as a function of cycle number with three constant engine lambda operations.

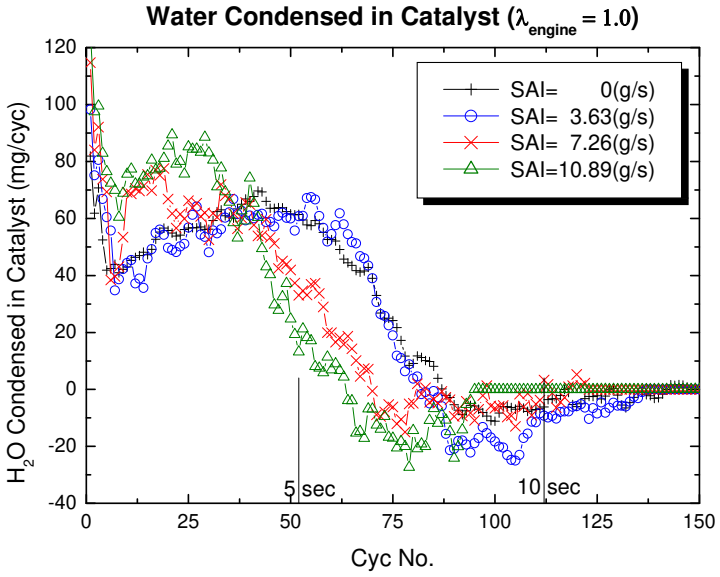

Figure 4-10 Water mass condensed inside the catalyst as a function of cycle number with different levels of SAI.

4.3 Effect of Secondary Air Injection Location

The thermal oxidation reaction is characterized by a dramatic increase in the exhaust gas temperature and a corresponding reduction in the HC and CO concentrations of the exhaust gas prior to the catalyst. The catalytic oxidation reaction is characterized by an increase in the rate of catalyst temperature rise when compared with a standard exhaust system. In general, catalytic oxidation occurs with secondary air injected into a rich mixture, once the catalyst reaches its light-off temperature. Thermal oxidation only occurs when secondary air injection conditions are optimized. Catalytic oxidation always accompanies thermal oxidation. For successful thermal oxidation, the secondary air should be injected as close to the exhaust valve as possible. Since the exhaust gas cool rapidly after leaving the cylinder, mixing the secondary air into the exhaust gas as soon as possible is crucial. However, in order to only achieve the catalytic oxidation reaction, the secondary air can be injected further downstream as long as sufficient mixing of the secondary air and exhaust gas can take place prior to catalyst entry [7,8].

A previous study found that the oxidation reaction in the exhaust gas could not be achieved with the open-end tube design which directed secondary air straight towards the valve [8]. It was considered that the pressure from the exhaust gas during the blowdown period was enough to shut off the flow of secondary air out of the tube and leave the exhaust gas largely unmixed with secondary air. Therefore, to avoid this possible back flow effect, the tube design in this study had a closed-end and two holes drilled on the side of the tube such that the secondary air flowed out of the tube perpendicular to the exhaust gas flow.

A preliminary experiment was conducted to compare the effect of secondary air injection location on HC and CO emissions. Figure 4-11 shows two locations in the port, 5mm and 40mm from the valve seat, respectively. Figure 4-12 and Figure 4-13 show the pre-catalyst and post-catalyst HC emissions with these two different air injection locations. The test clearly confirmed that injecting secondary air as close to the exhaust valve as possible was beneficial since the closer injection location strategy had the opportunity to enhance thermal oxidation of engine-out emissions which further sped up catalyst light-off and reduced the converter-in and converter-out emissions. Figure 4-14 and Figure 4-15 show the pre-catalyst and post-catalyst CO emissions with two different air injection locations and the results confirmed essentially the same trends with HC emissions.

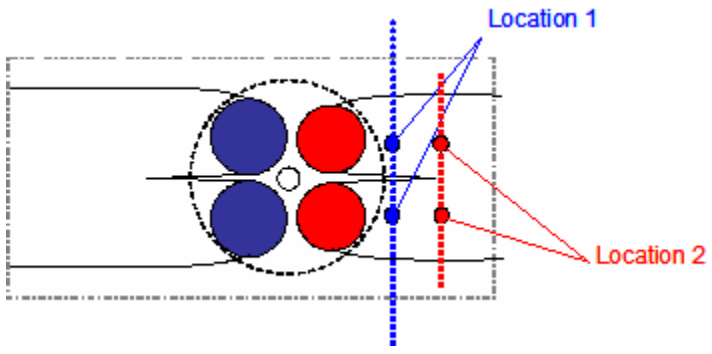

Figure 4-11 Diagram showing two secondary air injection locations (Location 1: 5mm from the valve seat, Location 2: 40mm from the valve seat).

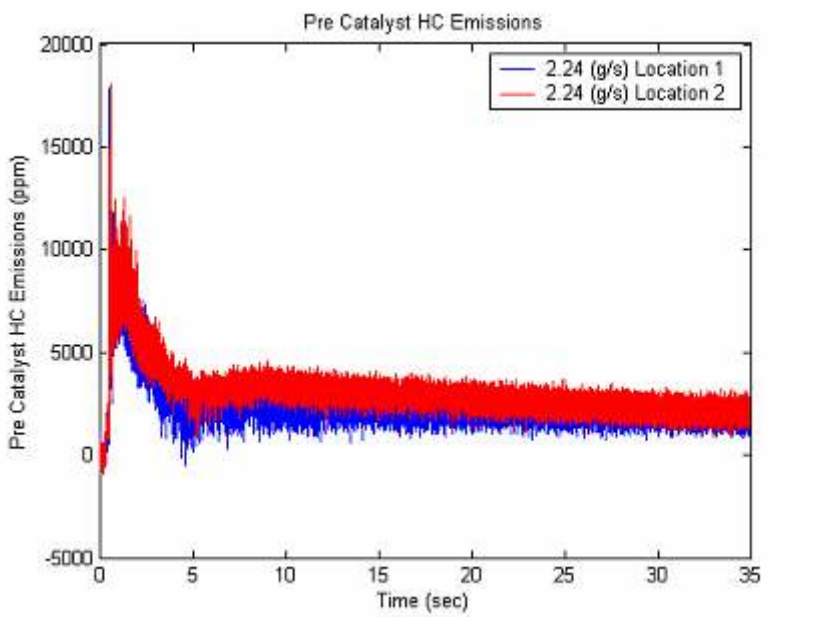

Figure 4-12 Pre-catalyst HC concentrations (ppmC_1) with two different injection locations for the first 35 seconds following a 20°C start.

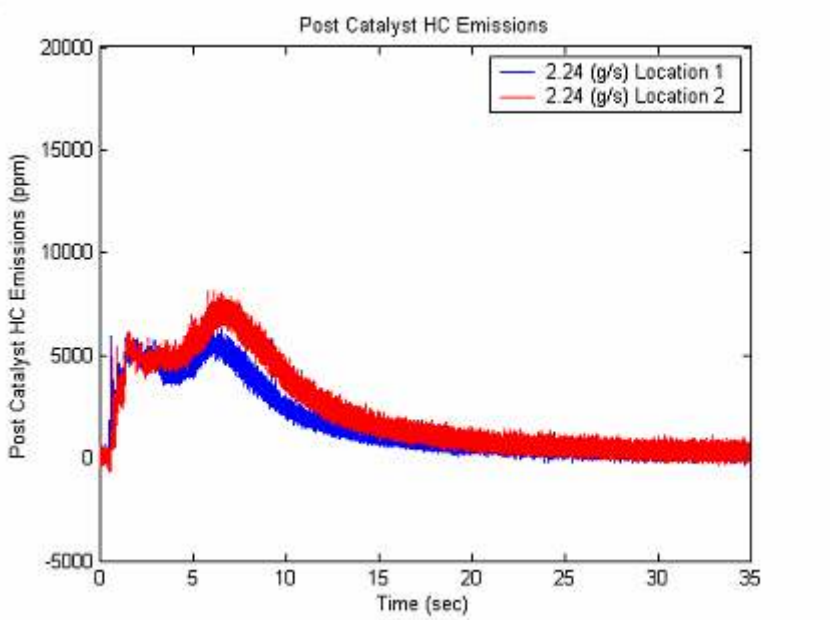

Figure 4-13 Post-catalyst HC concentrations (ppmC_1) with two different injection locations for the first 35 seconds following a 20°C start.

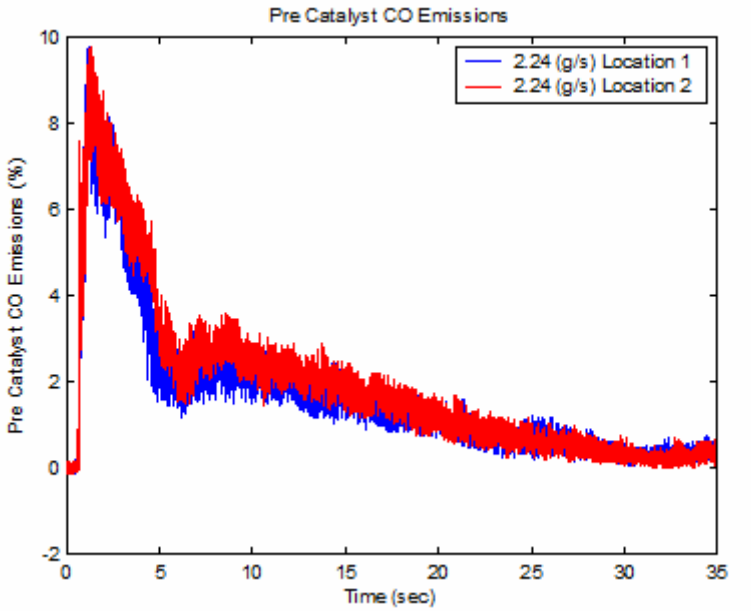

Figure 4-14 Pre-catalyst CO concentrations (%) with two different injection locations for the first 35 seconds following a 20°C start.

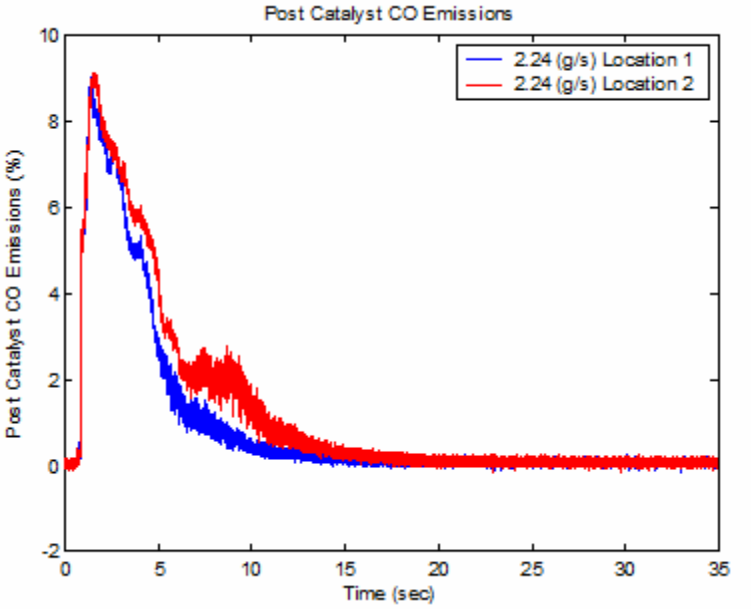

Figure 4-15 Post-catalyst CO concentrations (%) with two different injection locations for the first 35 seconds following a 20°C start.

4.4 Effect of Secondary Air Flow Rate

In order to investigate the effect of secondary air flow rate, HC and CO mass emissions were evaluated for various secondary air flow rates with three constant lambda conditions. The results from the mass flow rate model were analyzed in conjunction with the time-resolved emission measurements to obtain the instantaneous HC and CO mass flow rates from the cylinder exit to the post-catalyst location. The mass emissions per cycle were then calculated from the time integral of the mass emission flow rates. Figures 4-16 ~4-19 show HC and CO mass emissions per cycle as a function of cycle number with different levels of secondary air injection rate for the constant engine lambda of 0.8. Significant emissions reduction was achieved by the thermal oxidation process prior to the catalyst. This resulted in enhancing the chemical process inside the catalyst by faster catalyst light-off.

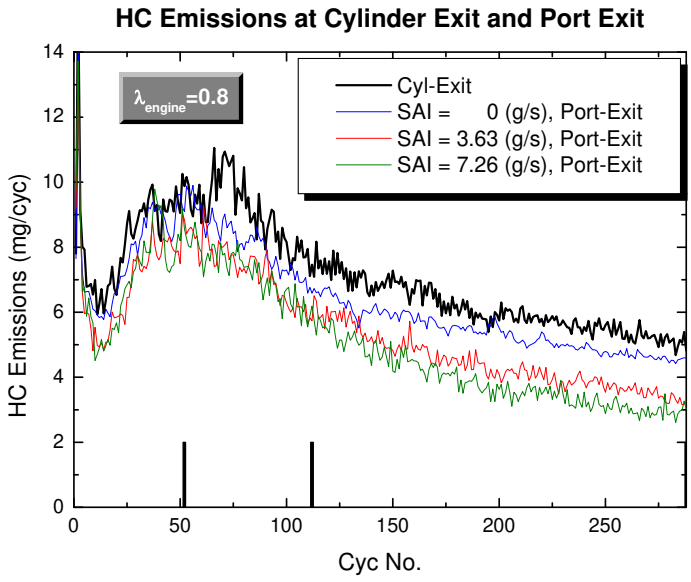

Figure 4-16 HC mass emissions per cycle as a function of cycle number at the cylinder exit and port exit with different levels of secondary air injection rate for the constant engine lambda of 0.8.

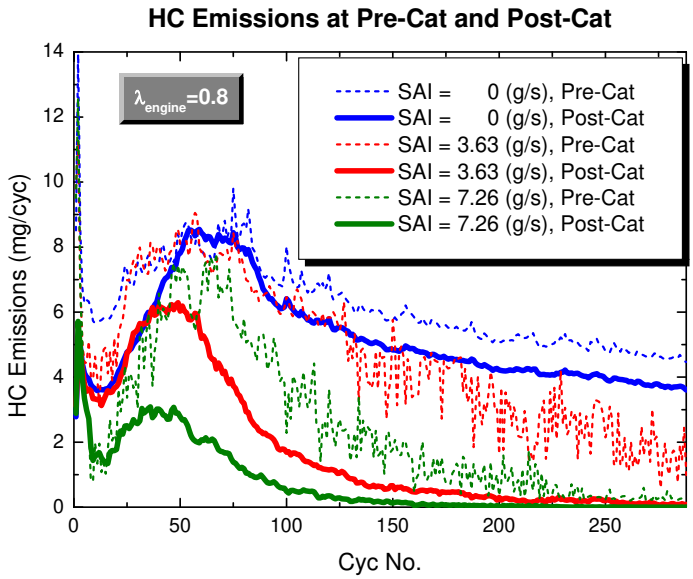

Figure 4-17 HC mass emissions per cycle as a function of cycle number at the pre-cat and post-cat with different levels of secondary air injection rate for the constant engine lambda of 0.8.

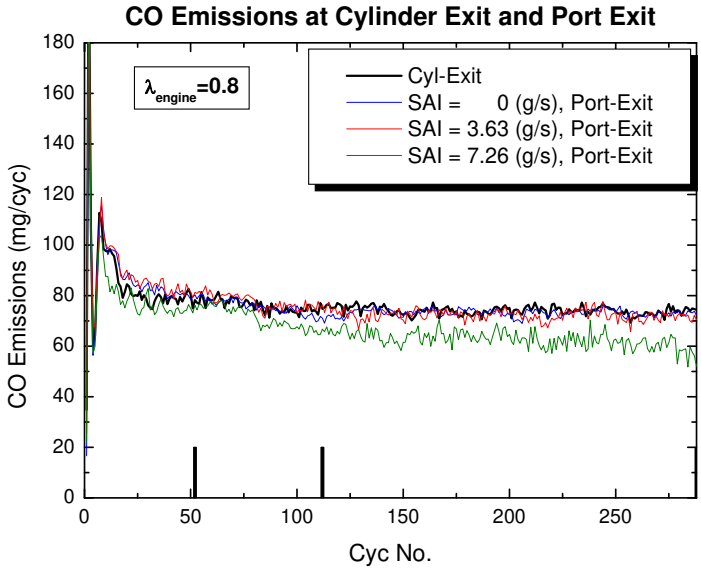

Figure 4-18 CO mass emissions per cycle as a function of cycle number at the cylinder exit and port exit with different levels of secondary air injection rate for the constant engine lambda of 0.8.

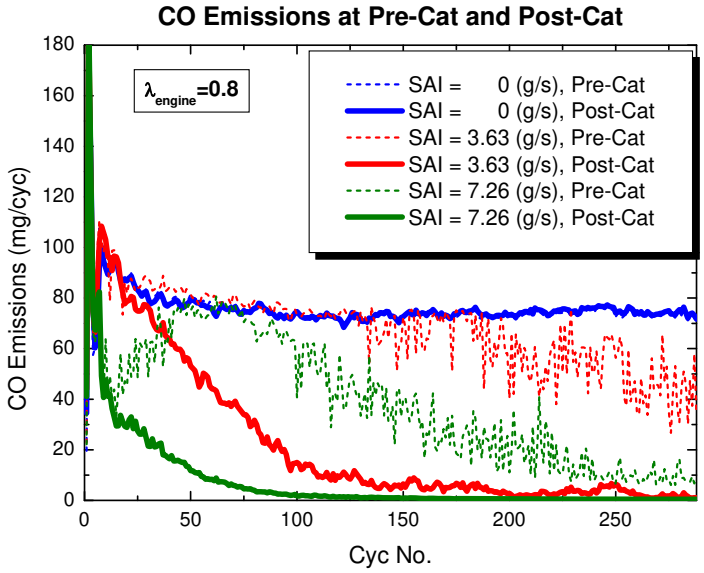

Figure 4-19 CO mass emissions per cycle as a function of cycle number at the pre-cat and post-cat with different levels of secondary air injection rate for the constant engine lambda of 0.8.

Cumulative HC and CO mass emissions were also evaluated for various secondary air flow rates with three constant lambda conditions. With the richest condition (engine lambda = 0.8), the post-catalyst HC emissions continued to decrease as the secondary air flow rate increased in the air flow range tested, as shown in Figure 4-20. However, Figure 4-21 and Figure 4-22 show that, with the conditions of engine lambda = 0.9 and 1.0, the post-catalyst HC emissions only continued to decrease up to SAI = 7.26 (g/s) and SAI = 3.63 (g/s), respectively. Similar trends were also observed in CO emissions as shown in Figures 4-23~4-25. Thermal oxidation was observed to decrease in the exhaust port and increase in the exhaust runner as the secondary air flow rate increased. The overall fraction of thermal oxidation was found to increase in the exhaust port and runner as the secondary air flow rate increased.

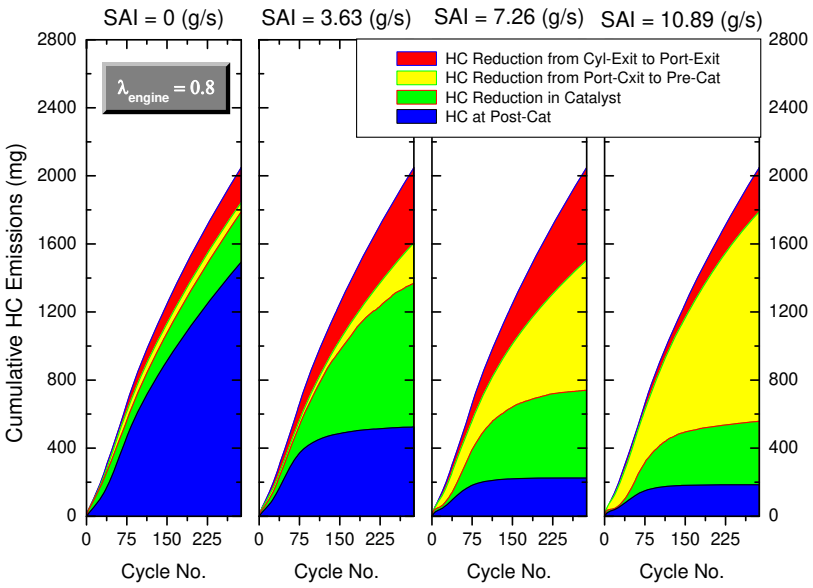

Figure 4-20 Cumulative HC mass emissions measured at the exhaust port exits of four cylinders, pre-catalyst and post-catalyst as a function of cycle number (λ_{engine}=0.8).

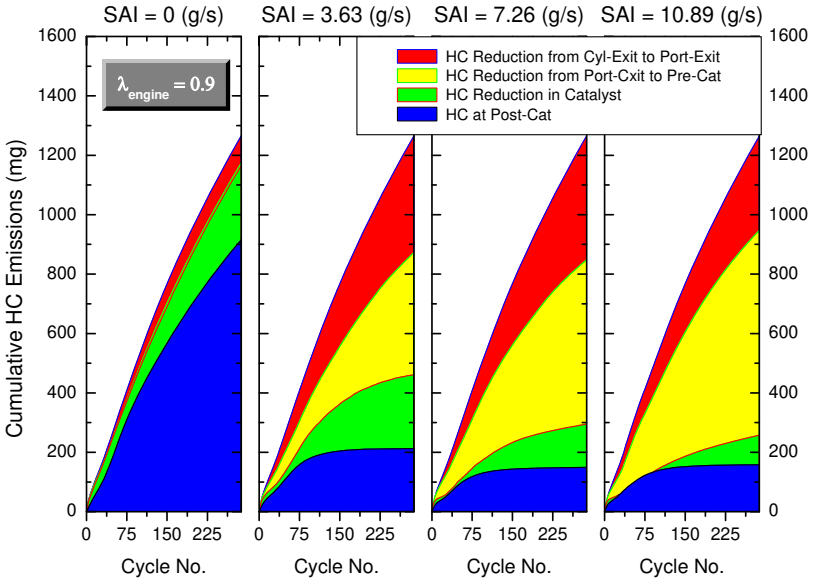

Figure 4-21 Cumulative HC mass emissions measured at the exhaust port exits of four cylinders, pre-catalyst and post-catalyst as a function of cycle number (λ_{engine}=0.9).

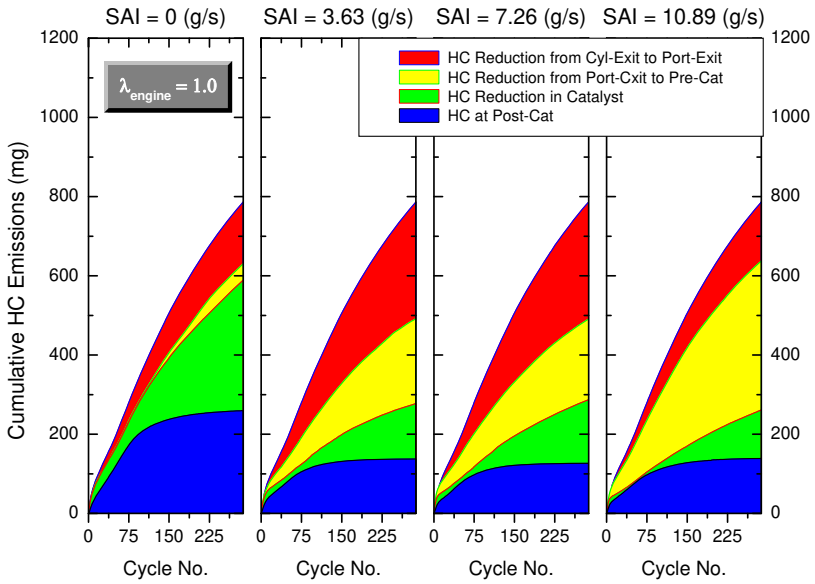

Figure 4-22 Cumulative HC mass emissions measured at the exhaust port exits of four cylinders, pre-catalyst and post-catalyst as a function of cycle number (λ_{engine}=1.0).

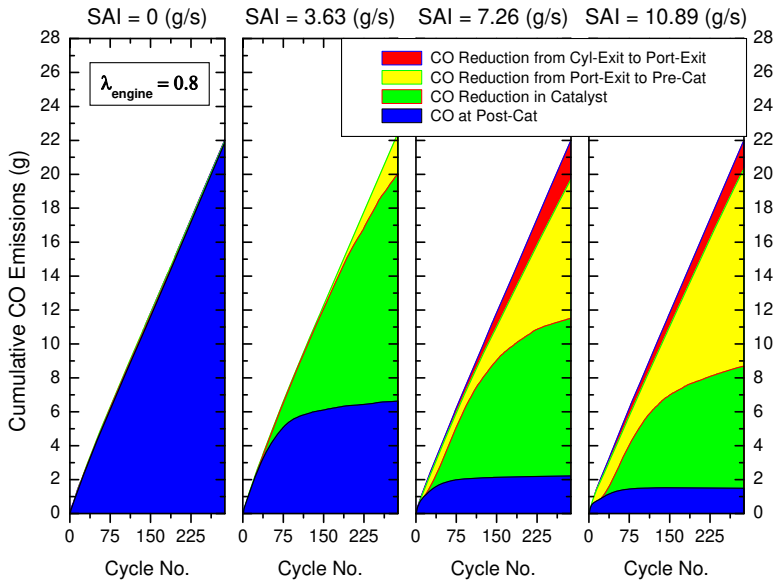

Figure 4-23 Cumulative CO mass emissions measured at the exhaust port exits of four cylinders, pre-catalyst and post-catalyst as a function of cycle number (λ_{engine}=0.8).

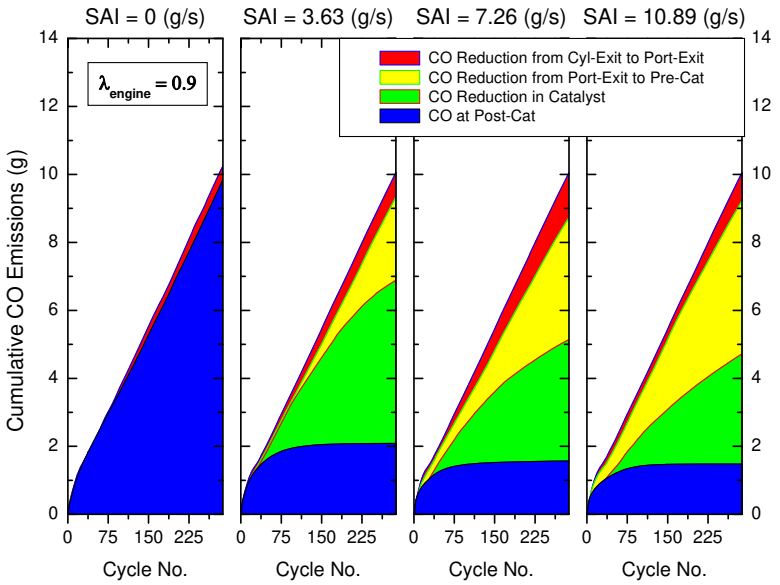

Figure 4-24 Cumulative CO mass emissions measured at the exhaust port exits of four cylinders, pre-catalyst and post-catalyst as a function of cycle number (λ_{engine}=0.9).

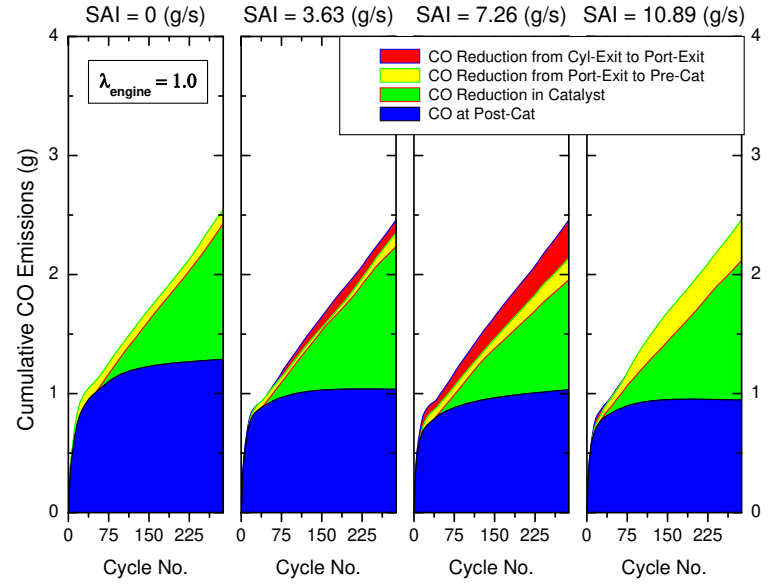

Figure 4-25 Cumulative CO mass emissions measured at the exhaust port exits of four cylinders, pre-catalyst and post-catalyst as a function of cycle number (λ_{engine}=1.0).

4.5 Effect of Exhaust Lambda

To quantify the effect of the exhaust lambda, HC and CO mass emissions were normalized by the amount of injected fuel. Figure 4-26 and Figure 4-27 show the mass fractions of cumulative HC and CO emissions normalized by the amount of injected fuel at the post-catalyst location as a function of cumulative exhaust lambda for each time period (0-5, 0-10 and 0-25 seconds). The mass fractions of HC and CO emissions were observed to decrease up to an exhaust lambda of 1.3 as the secondary air injection rates increased. However, in the region of exhaust lambda higher than 1.3, there were no noticeable benefits on the post-catalyst emissions. The overall analysis of the experimental data showed that the post-catalyst HC emissions levels were optimized with a secondary air flow rate corresponding to an overall exhaust lambda of 1.3.

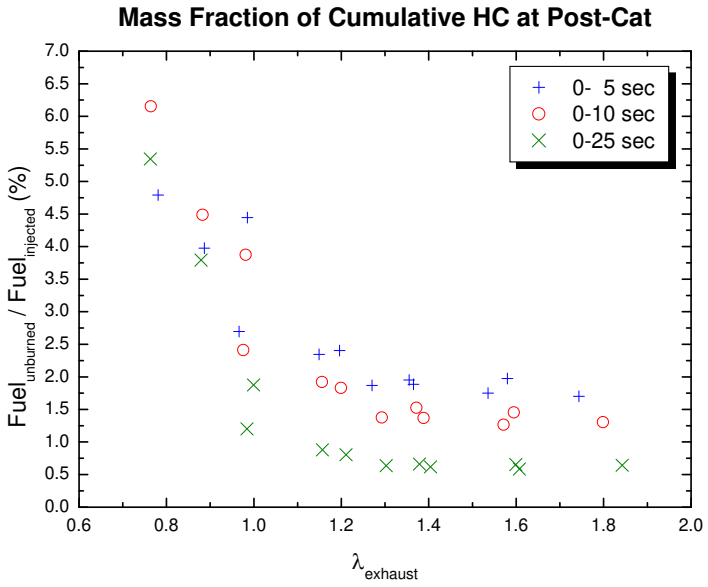

Figure 4-26 Mass fraction of cumulative HC emissions normalized by the amount of injected fuel at the post-catalyst location as a function of cumulative exhaust lambda for each time period (0-5, 0-10 and 0-25 seconds).

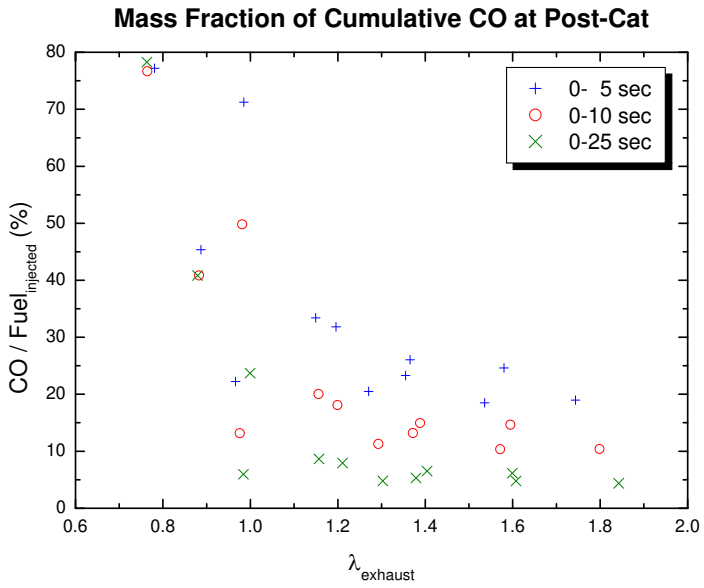

Figure 4-27 Mass fraction of cumulative CO emissions normalized by the amount of injected fuel at the post-catalyst location as a function of cumulative exhaust lambda for each time period (0-5, 0-10 and 0-25 seconds).

4.6 Catalyst Light-off Performance

Catalyst light-off experiments were conducted with a 50k mile aged ULEV catalyst. Hydrocarbon concentrations were monitored at the pre-catalyst and post-catalyst utilizing the Cambustion fast-response FID analyzer. Catalyst light-off was defined as the 50% conversion efficiency of hydrocarbons (η_{HC} = 50%). Figure 4-28 and Figure 4-29 show the exhaust gas temperatures at the 1st and 2nd catalyst brick with various SAI strategies as a function of cycle number during the first 25 seconds following engine cranking. The 50% light-off temperatures were observed to decrease greatly with SAI under fuel-rich engine operations. The engine operation, with a relative air/fuel ratio 20% rich of stoichiometric and 100% secondary air, yielded the highest catalyst feed-gas temperature prior to catalyst light-off, and the fastest catalyst light-off (4.2 sec) as shown in Figure 4-30 and Figure 4-31. However, an improvement in the thermal oxidation reaction at the later period of cold start-up caused a decrease in the catalytic oxidation reaction due to the increased consumption of reactants upstream of the catalyst.

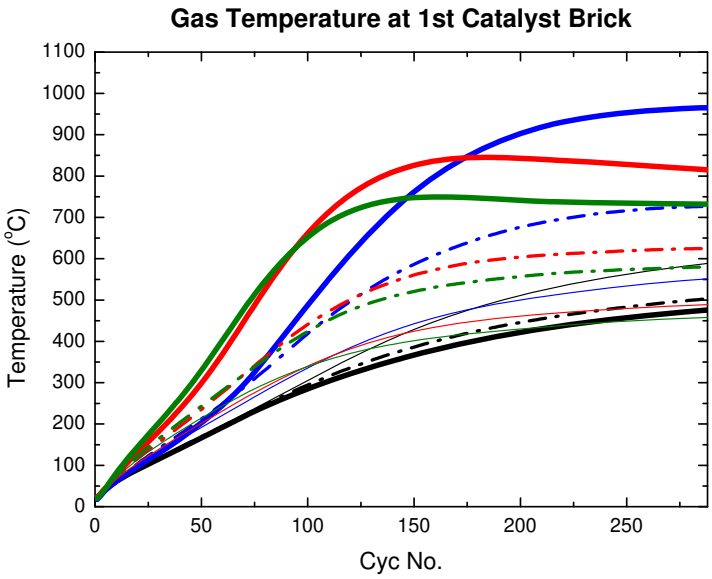

Figure 4-28 Exhaust gas temperatures at 1st catalyst brick as a function of cycle number for various secondary air flow rates with three constant lambda conditions.

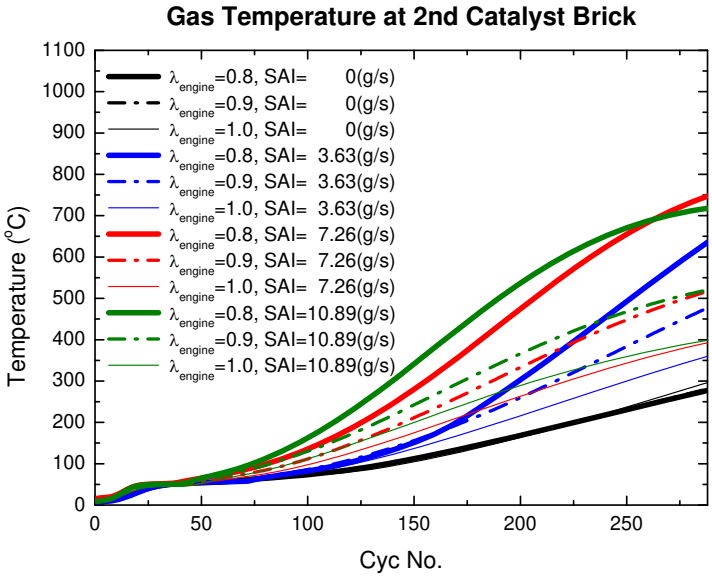

Figure 4-29 Exhaust gas temperatures at 2nd catalyst brick as a function of cycle number for various secondary air flow rates with three constant lambda conditions.

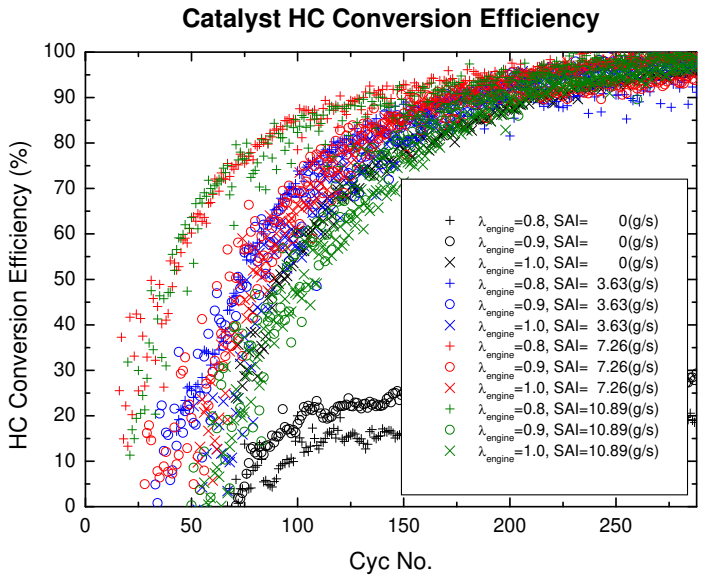

Figure 4-30 HC conversion efficiency as a function of cycle number for various secondary air flow rates with three constant lambda conditions.

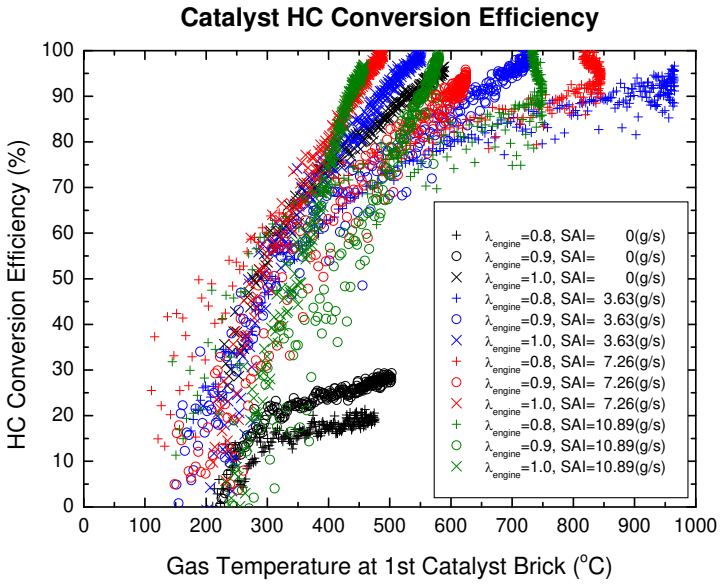

Figure 4-31 HC conversion efficiency as a function of gas temperature at 1st catalyst brick for various secondary air flow rates with three constant lambda conditions.

It should be noted that there is a difference between light-off time and light-off temperature. The distinction is that a reduction in light-off temperature generally means a reduction in light-off time, but not necessarily vice versa. A prevalent confounding influence here is space velocity, since it cannot readily be controlled independently of the other variables at least on an engine [7]. Increased oxygen concentration in the feed gas has been to have a favorable effect on lowering the catalyst light-off temperatures with catalysts having a high Pd content [22]. However, with 100% secondary air, the catalyst light-off temperatures were increased due to the reduced energy released directly inside the catalyst.

Table 4-1 Catalyst light-off time (sec)

SAI / Lambda	0 (g/s)	3.63 (g/s)	7.26 (g/s)	10.89 (g/s)
0.8	> 25	6.9	4.3	4.2
0.9	> 25	6.9	7.0	9.0
1.0	8.4	7.7	7.5	9.2

4.7 Overall Assessment of SAI

In order to assess the impact of secondary air injection, cumulative HC and CO emissions were evaluated from the first 5, 10 and 25 seconds of three different lambda start-up processes. Cumulative emissions were calculated based upon the exhaust mass flow model. Cumulative HC and CO mass emissions as a function of secondary air injection rate are shown in Figures 4-32~4-37. The highest emissions were observed at the cylinder exit and decreased with distance from the exhaust valves. Thermal oxidation was observed to transition from the exhaust port to the exhaust runner as the secondary air flow rate increased. The overall fractions of HC and CO oxidized in the exhaust port and runner were increased with higher injection rates of secondary air. Promoting thermal oxidation in the port and runner effectively increased the exhaust gas temperature and also decreased the converter-in emissions. However, an improvement in the thermal oxidation reaction caused a decrease in the catalytic oxidation reaction, due to the increased consumption of reactants upstream of the catalyst. There was a trade-off between the amount of thermal and catalytic oxidation reaction occurring in the different parts of the exhaust system. Comparable overall HC emissions reductions were achieved over an engine lambda range of 0.8 to 0.9 and secondary air flow rate range of 67% to 33%.

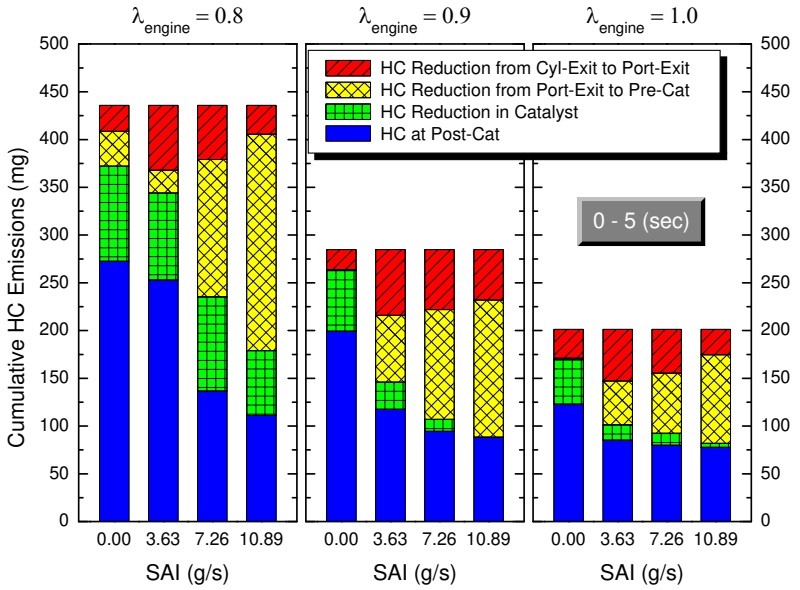

Figure 4-32 Cumulative HC mass emissions from the cylinder exit to the post-catalyst as a function of secondary air injection rate during the first 5 seconds of three constant lambda start-up operations.

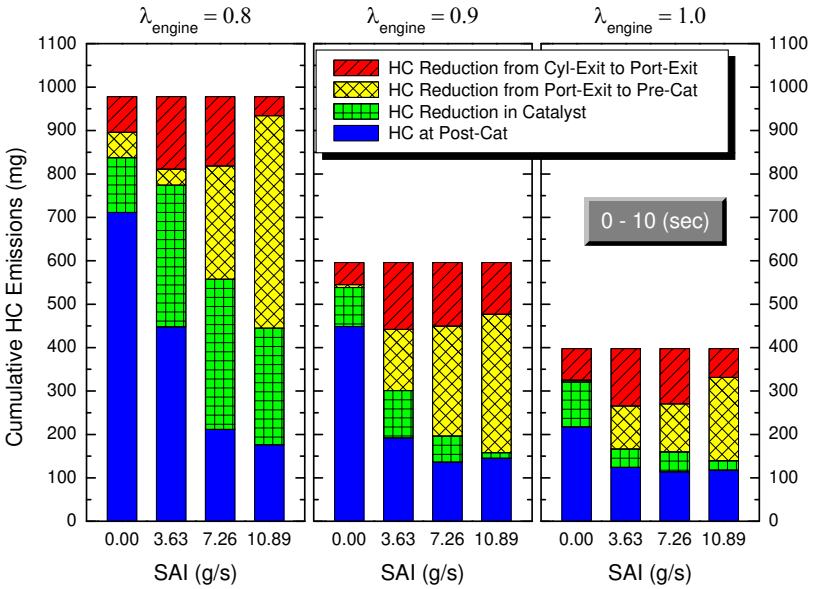

Figure 4-33 Cumulative HC mass emissions from the cylinder exit to the post-catalyst as a function of secondary air injection rate during the first 10 seconds of three constant lambda start-up operations.

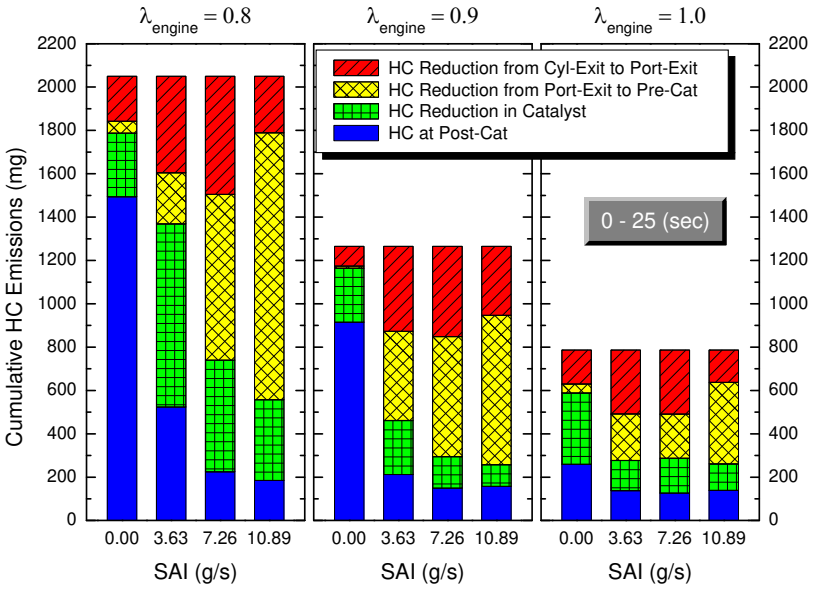

Figure 4-34 Cumulative HC mass emissions from the cylinder exit to the post-catalyst as a function of secondary air injection rate during the first 25 seconds of three constant lambda start-up operations.

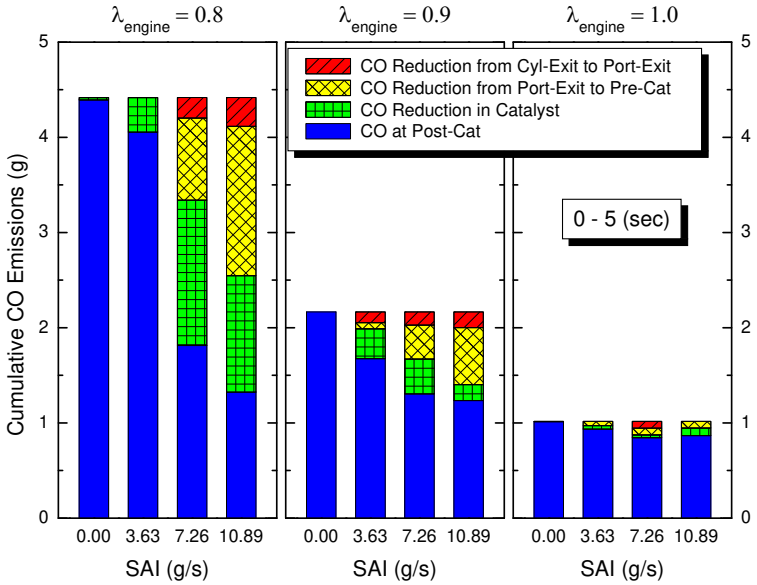

Figure 4-35 Cumulative CO mass emissions from the cylinder exit to the post-catalyst as a function of secondary air injection rate during the first 5 seconds of three constant lambda start-up operations.

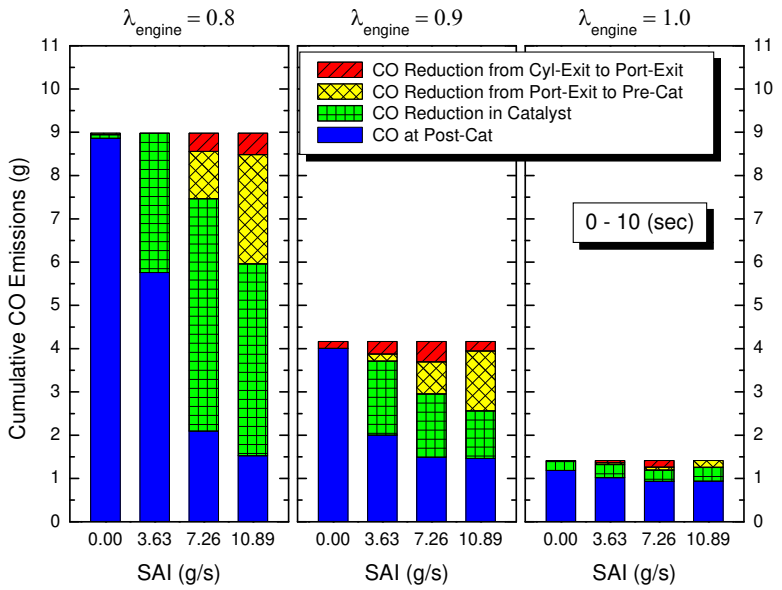

Figure 4-36 Cumulative CO mass emissions from the cylinder exit to the post-catalyst as a function of secondary air injection rate during the first 10 seconds of three constant lambda start-up operations.

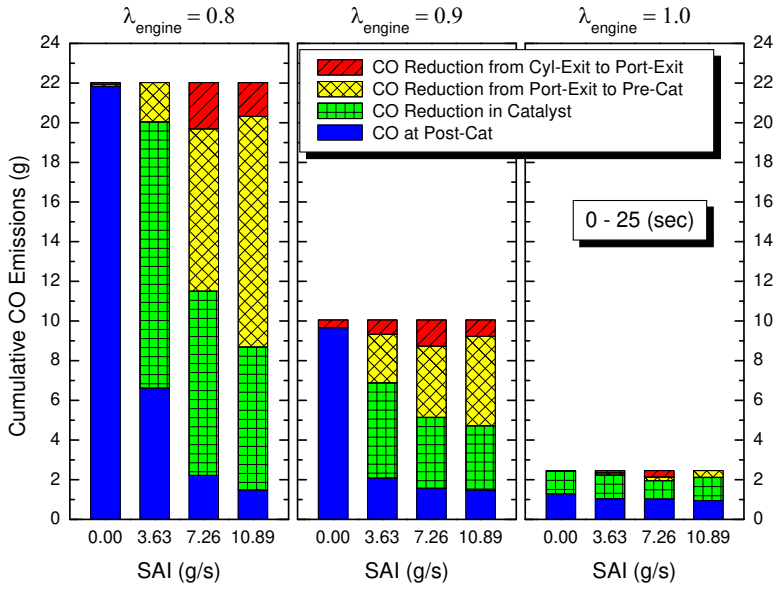

Figure 4-37 Cumulative CO mass emissions from the cylinder exit to the post-catalyst as a function of secondary air injection rate during the first 25 seconds of three constant lambda start-up operations.

An increase in the amount of secondary air permits a faster mixing of the exhaust gas with secondary air. The conditions at the port are favorable for higher oxidation reactions with increased mixing rates. However, the more effective cooling and less amount of combustible gas prior to the catalyst with the higher amount of secondary air have offsetting effects on the catalytic oxidation inside the catalyst. Therefore, the post-catalyst HC emission levels were not strongly affected by the mixing rates in the air flow range tested.

The results reported here show that an overall exhaust lambda of 1.3 is required to achieve the minimum post-catalyst HC emissions level with secondary air injection. Based on this conclusion, the amounts of optimum secondary air were also suggested at given engine lambda conditions as shown in Figure 4-38.

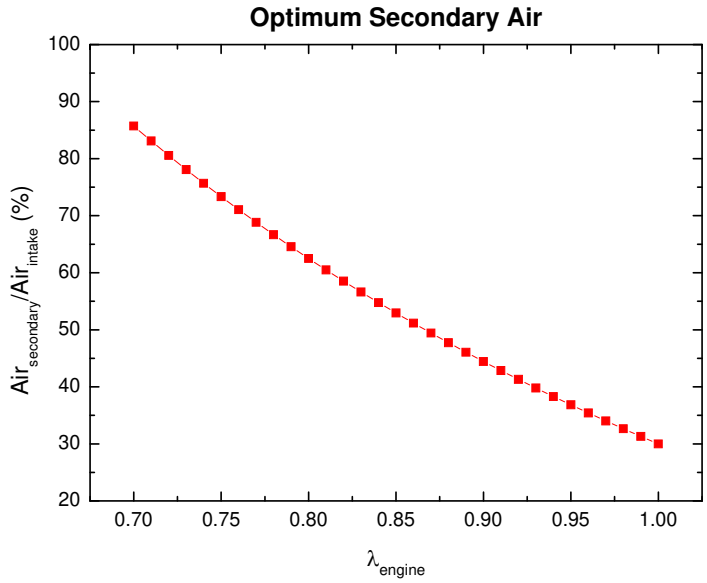

Figure 4-38 Optimum secondary air amount recommended for minimum emissions during cold start as a function of engine lambda.

Chapter 5

Thermal Analysis of Exhaust System

5.1 Exhaust Gas Temperature

The local oxidation rate depends on the pressure, temperature and composition of the mixture. The pressure in the exhaust system is virtually constant and atmospheric. The combustion process is complicated and involves a variety of reaction paths and elementary reactions. However, the most important parameters influencing the oxidation rate are the temperature and the presence of oxygen and combustible gases. A simple correlation for the hydrocarbon oxidation rate (shown below) gives an idea of how the oxidation rate varies. However, it is necessary to consider more detailed reaction schemes for accurate results, especially at low temperatures.

$$\frac{dHC}{dt} = -3.36 \cdot 10^{10} \cdot \exp\left(\frac{-31000}{RT}\right) \cdot [HC] \cdot [O_2]^{0.25} \tag{5.1}$$

The cold start-up process produces a variety of different conditions with regard to gas composition and temperature in the exhaust port and manifold at any instant in time. The HC oxidation rate depends on the environment that HC molecules encounter on their way downstream to the catalyst. Equation (5.1) implies that the hydrocarbons only oxidize in the exhaust system upstream of the catalyst if oxygen molecules are present at sufficiently high temperatures. Since the temperature is exponentially correlated with the oxidation rate, one major parameter influencing the HC oxidation rate is the mixture temperature.

Therefore, the average exhaust gas temperature can be an important quantity for determining the performance of exhaust gas oxidation by the secondary air injection. The time-averaged exhaust gas temperature does not correspond to the average energy of the exhaust gas because the flow rate varies substantially. An enthalpy-averaged temperature is the best indicator of exhaust thermal energy.

$$\overline{T}_h = \frac{\int_{EVO}^{EVC} \dot{m} c_p T_g \, dt}{\int_{EVO}^{EVC} \dot{m} c_p \, dt} \tag{5.2}$$

Average exhaust gas temperatures are usually measured with a thermocouple. Thermocouple-averaged temperatures are close to time-averaged temperatures. Mass-averaged temperatures (which are close to enthalpy-averaged temperatures if c_p variations are small) for a spark-ignition engine at the exhaust port exit are about 100 K higher than time-averaged or thermocouple-determined temperatures [1].

5.2 Exhaust Gas Heat Transfer Model

5.2.1 Model Overview

Since the thermodynamic state of the exhaust mixture was difficult to measure experimentally, a simplified heat transfer model combined with a mass flow rate model was used to calculate exhaust gas mass-averaged temperatures from the cylinder exit to the catalytic converter inlet. This heat transfer model employed two zones; the exhaust port zone and the runner zone. Each zone had a specific exhaust geometry and heat transfer correlation.

The flow was approximated as plug flow in order to formulate the heat transfer model of exhaust gas from cylinder-exit to converter-in. The physical processes in the exhaust system were approximated as quasi-steady and one-dimensional. Cylinder-exit gas was discretized into three constant mass elements, shown in Figure 5-1. The first element contained mass expelled during the compressible blowdown period (EVO to 19^{o}ABDC), the second mass element held mass from the incompressible displacement period

(20°ABDC to EVC) and the third mass element contained mass displaced by secondary air during the valve closed period. Each element was an isolated moving control volume with infinitely fast mixing; uniform properties with no pressure, temperature, or concentration gradient [23].

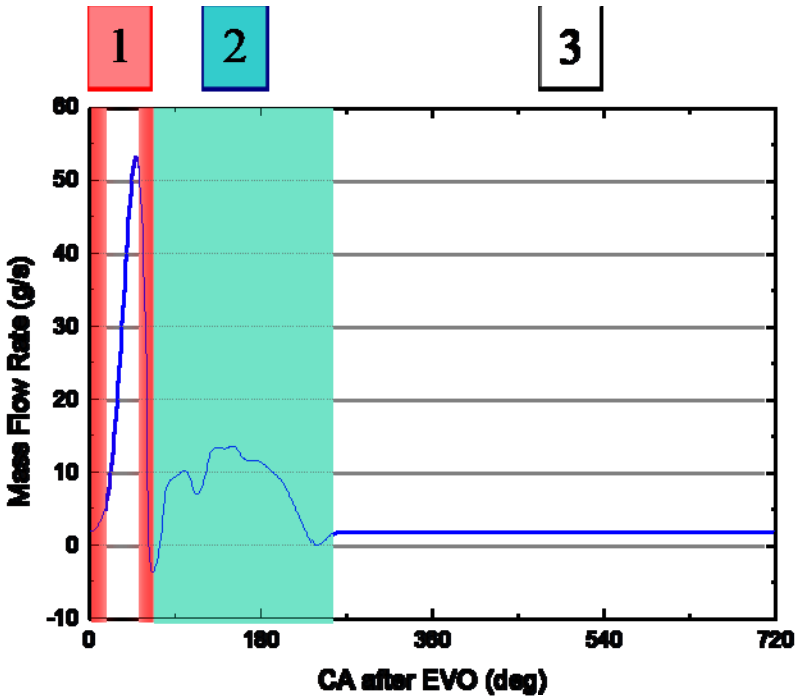

Figure 5-1 Schematic of three mass elements in the exhaust gas flow after EVO.

As each mass segment evolved, heat transfer to the inner pipe wall was modeled, but no interactions were allowed between elements. Heat transfer was assumed to be perpendicular to the surface and circumferentially uniform. In addition, the exhaust gas was assumed to satisfy the ideal gas relationship and to have average thermodynamic properties, which were calculated using a mole fraction weighted average of the individual specific properties. For exhaust gas temperatures above 1000K, thermodynamic properties were determined from approximated data which allowed for chemical dissociation [20].

5.2.2 Initial Conditions

The thermodynamic state of the cylinder gas during the exhaust process was required to estimate the exhaust gas temperature at the port exit and subsequent downstream positions. The cylinder gas enthalpy during the exhaust process was calculated from the cylinder gas temperature and species composition. The cylinder gas temperature was calculated from the ideal gas relationship using the measured cylinder pressure data and the instantaneous exhaust mass flow rate as described in Section 4.1. The cylinder gas composition was also quantified from direct measurements of exhaust HC, CO and CO_2 concentrations, and stoichiometry by utilizing nitrogen quenching experiments.

The thermodynamic state of the cylinder gas was also discretized into two mass elements; the first element for the compressible blowdown period and the second element for the incompressible displacement period. Each element had a mass-averaged temperature and exhaust gas composition obtained from time-resolved emission measurements and species balances described in Section 3 and 4.

5.2.3 Exhaust Port Heat Transfer

The heat transfer process in the exhaust port was governed by different mechanisms depending on the exhaust valve lift. Caton *et al.* [20] noted the exhaust port heat transfer for the blowdown process was dominated by a large scale motion which was approximated as convergent conical jet flow. High jet velocities produced large scale eddies in the exhaust port that scaled approximately with half of the port diameter. The Nusselt number (Nu) was calculated from a simple power law empirical correlation using the Reynolds number (Re) based on half of the port diameter and a Prandtl number (Pr) of 0.65. During the exhaust displacement period, the Nusselt number was established from turbulent pipe flow correlations (Pr=0.65) with empirical constants C_1 and C_2 for pipe roughness and developing flow [24]. During the exhaust valve closed period, heat transfer occurs between the exhaust gas and port surfaces, mainly due to the gas motion which persists after the exhaust valve closed. The heat transfer during the exhaust valve closed period was assumed to be primarily the result of wall-generated turbulence and hence the empirical correlation for heat transfer in a pipe was used. In this case, the velocity of the

residual motion was approximated by the average velocity for the time period of the complete four stroke engine cycle. This is a pseudo-exhaust flow rate since the valve is closed for roughly two-thirds of the total time. Even though the Reynolds numbers during the valve closed period are generally low, the correlation for turbulent flow was used because the gas motion is highly unstable due to flow reversal, thermal gradient and external vibration [20].

Table 5-1 Nusselt-Reynolds number correlations for the exhaust port heat transfer.

Exhaust Port	
Blowdown	$Nu_1 = 0.4*Re_j^{0.6}$
Displacement	$Nu_2 = 1.0\{0.0194*C_1*C_2*Re_D^{0.8}\}$
Valve closed	$Nu_3 = 1.0\{0.0194*C_1*C_2*Re_D^{0.8}\}$

5.2.4 Exhaust Runner Heat Transfer

The previous investigation found that the large scale motion was not a significant feature of the flow after 3or 4 diameters downstream of the exhaust valve [20]. Therefore, an empirical heat transfer coefficient for turbulent, fully developed pipe flow was adequate for the exhaust runner. Effects of exhaust pulsations and pipe bends were accounted for by augmenting factors F_{pulse} and F_{bend}, respectively, which were used to modify the Nusselt number [23].

Table 5-2 Nusselt-Reynolds number correlations for the exhaust runner heat transfer.

Exhaust Runner
$Nu_{runner} = 1.0\{0.0194*C_1*C_2*Re_D^{0.8}\}$

5.2.5 Model Validation

After quantifying the thermodynamic state of cylinder gas, the chemical energy released from combustible species (HC, CO, H_2) was added as an internal heat source to the port and runner region in the heat transfer model. An iteration process was applied to

determine the gas temperature of each mass element at the port exit and the pre-catalyst position.

Model predictions of the average temperatures were evaluated to insure that the model adequately predicted the heat transfer processes in the exhaust port and runner. Cylinder exit conditions drove the heat transfer sub-routine with correlations based upon empirical data. The model assumed that the wall boundary layer and core gases were homogeneous in temperature and composition. Agreement within 50 K was achieved between time-averaged temperatures predicted by the heat transfer model and direct time-averaged temperatures measured from the experiments, as shown in Figure 5-2 and Figure 5-3.

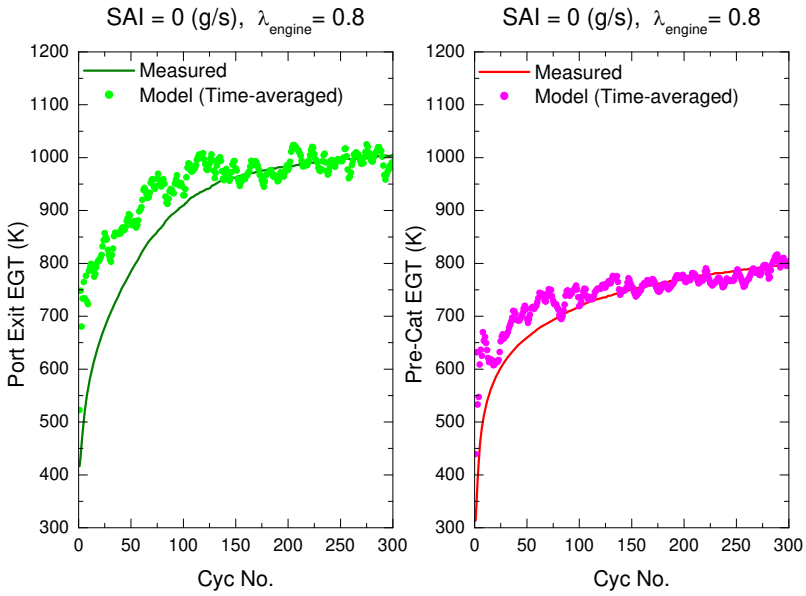

Figure 5-2 Measured and predicted time-averaged exhaust gas temperature as a function of cycle number at the port exit and the pre-catalyst (λ_{engine} = 0.8, SAI = 0.00 g/s).

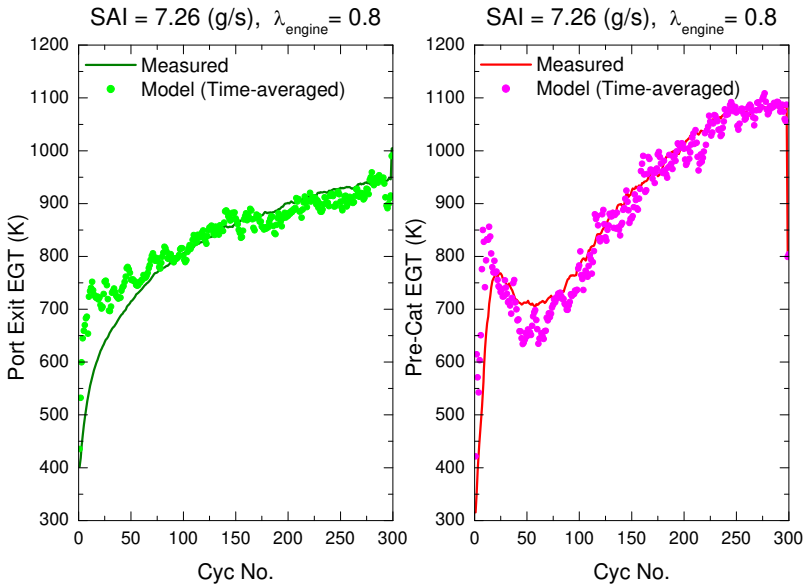

Figure 5-3 Measured and predicted time-averaged exhaust gas temperature as a function of cycle number at the port exit and the pre-catalyst (λ_{engine} = 0.8, SAI = 7.26 g/s).

Figure 5-4 and Figure 5-5 compares measured and mass-averaged predicted temperatures at the exhaust port and the pre-catalyst. Previous investigations have indicated that the mass-averaged (enthalpic) temperatures are generally 10-20% higher than the time-averaged temperatures obtained with thermocouple sensors [25]. Agreement was achieved between the experiments and the heat transfer model.

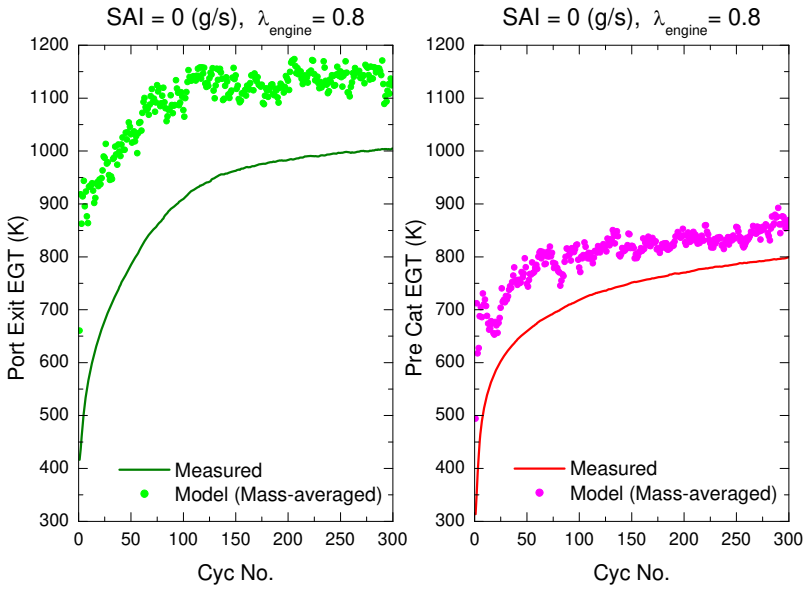

Figure 5-4 Predicted mass-averaged exhaust gas temperature versus thermocouple-measured exhaust gas temperature as a function of cycle number at the port exit and the pre-catalyst (λ_{engine} = 0.8, SAI = 0.00 g/s).

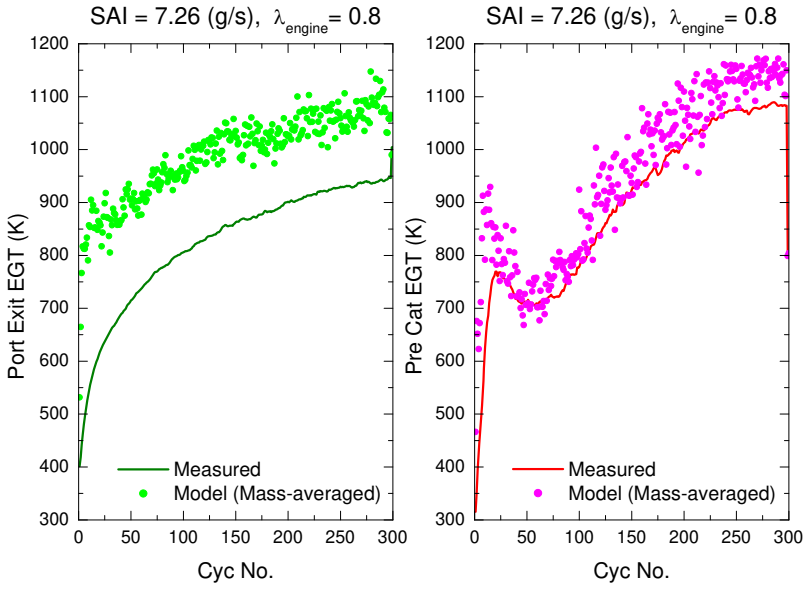

Figure 5-5 Predicted mass-averaged exhaust gas temperature versus thermocouple-measured exhaust gas temperature as a function of cycle number at the port exit and the pre-catalyst (λ_{engine} = 0.8, SAI = 7.26 g/s).

5.3 Chemical Energy Release and Heat Loss

In order to investigate the chemical energy release and heat loss in the exhaust gas with SAI, the mass-averaged exhaust gas temperatures predicted by the heat transfer model were analyzed in conjunction with the mass elements obtained by the exhaust mass flow rate model. Cumulative chemical energy release and heat loss were evaluated for various secondary air flow rates with three constant lambda conditions as shown in Figures 5-6~5-11. Promoting thermal oxidation in the exhaust port and runner was effective in increasing the release rate of chemical energy and therefore was also effective in raising the exhaust gas temperature. The amount of chemical energy released from the exhaust oxidation was observed to increase significantly with higher levels of fuel enrichment at each secondary air flow rate condition. However, the heat loss from the cylinder exit to the pre-catalyst was not sensitive to the engine lambda and secondary air flow rate. Higher heat transfer rates from increased temperatures and mass flow rates with SAI were compensated by the increased chemical energy released from the oxidation of HC, CO and H_2 with SAI.

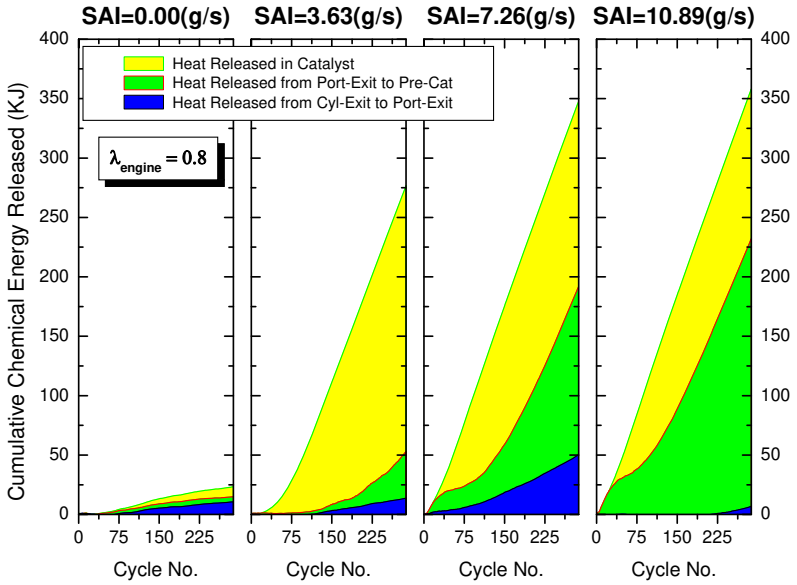

Figure 5-6 Cumulative chemical energy released from the cylinder exit to the post-catalyst as a function of cycle number with different levels of secondary air injection rate for the constant engine lambda of 0.8.

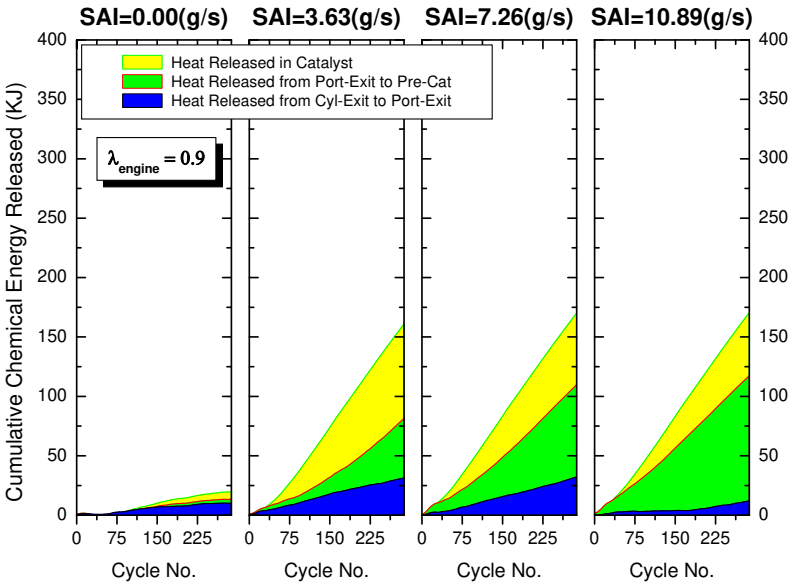

Figure 5-7 Cumulative chemical energy released from the cylinder exit to the post-catalyst as a function of cycle number with different levels of secondary air injection rate for the constant engine lambda of 0.9.

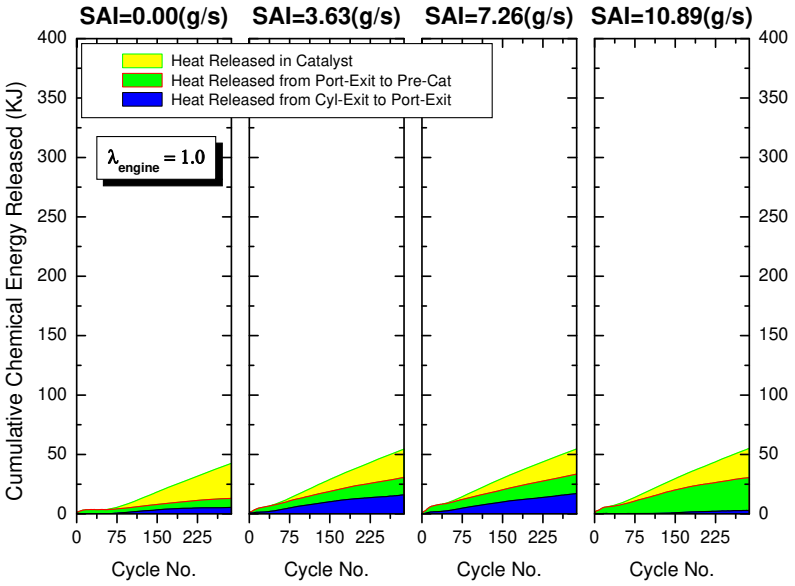

Figure 5-8 Cumulative chemical energy released from the cylinder exit to the post-catalyst as a function of cycle number with different levels of secondary air injection rate for the constant engine lambda of 1.0.

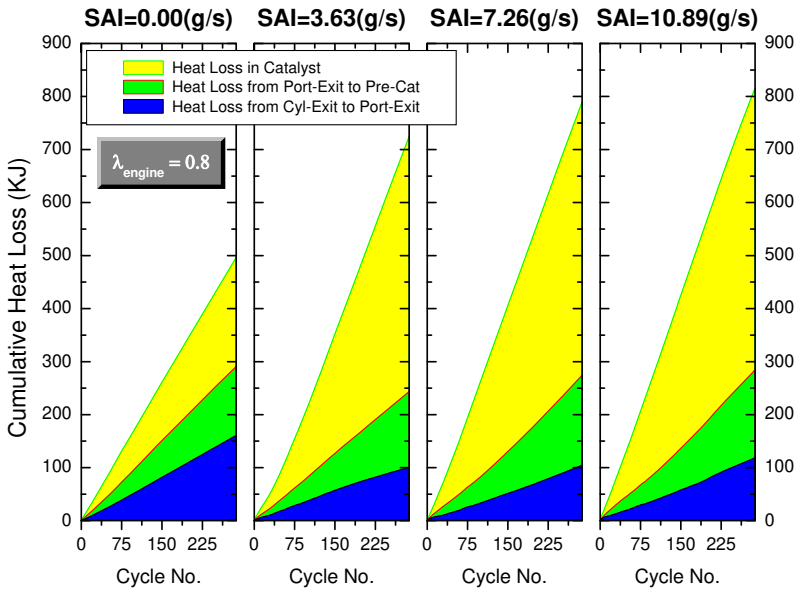

Figure 5-9 Cumulative heat losses from the cylinder exit to the post-catalyst as a function of cycle number with different levels of secondary air injection rate for the constant engine lambda of 0.8.

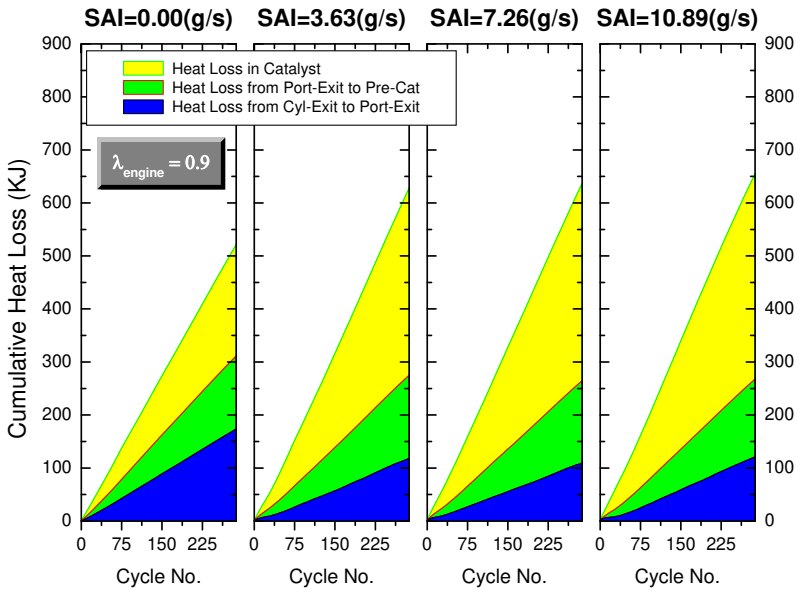

Figure 5-10 Cumulative heat losses from the cylinder exit to the post-catalyst as a function of cycle number with different levels of secondary air injection rate for the constant engine lambda of 0.9.

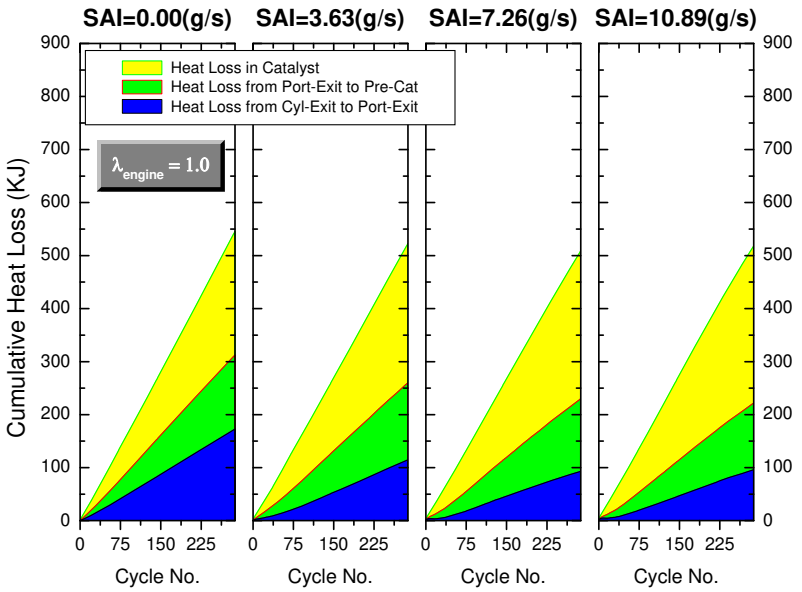

Figure 5-11 Cumulative heat losses from the cylinder exit to the post-catalyst as a function of cycle number with different levels of secondary air injection rate for the constant engine lambda of 1.0.

Figure 5-12 shows chemical energy released from the cylinder exit to the post-catalyst as a function of cycle number with different secondary air injection rates at each constant engine lambda condition. It was found that secondary air could utilize more than 90% of cylinder-out exhaust gas chemical energy by promoting the burn-up process in the exhaust system.

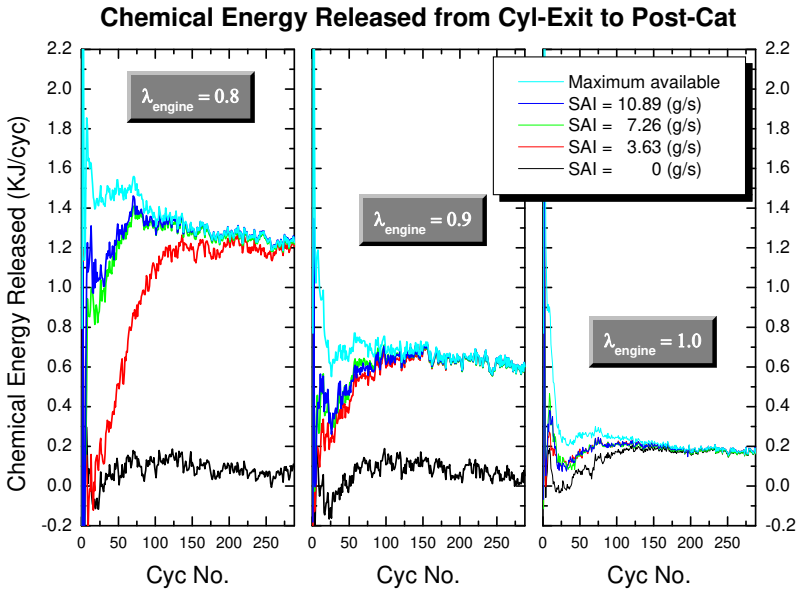

Figure 5-12 Chemical energy released from the cylinder exit to the post-catalyst as a function of cycle number with different secondary air injection rates at each engine lambda condition.

Chapter 6

Findings and Conclusions

6.1 Overview

An experimental study was performed to develop a more fundamental understanding of the effects of SAI on exhaust gas emissions and catalyst light-off characteristics during cold start of a modern SI engine. The effects of several design and operating parameters such as spark retardation, fuel enrichment, secondary air flow rate and air injection location were investigated to understand the mixing, heat loss, and thermal and catalytic oxidation processes associated with SAI. Time-resolved HC, CO and CO_2 concentrations were tracked from the cylinder exit to the catalytic converter outlet and converted to mass flow rates by applying an instantaneous exhaust mass flow rate model. A phenomenological model of exhaust heat transfer combined with the gas composition analysis was also developed to define the thermal and chemical energy state of the exhaust gas with SAI.

6.2 Findings

Engine start-up experiments were conducted with three different constant lambda start-up strategies. Exhaust gas emissions, gas heat transfer, and catalyst light-off performance were evaluated with various secondary air injection strategies during the first 25 seconds following engine cranking. The following findings were obtained from the results of those engine start-up experiments and their analysis.

- The engine operation, with a relative air/fuel ratio 20% rich of stoichiometric and 100% secondary air, yielded the highest catalyst feed-gas temperature prior to catalyst light-off and the fastest catalyst light-off (4.2 sec).

- The SAI system reduced HC emissions by 46% to 88% and CO emissions by 37% to 93% compared with operation without any secondary air during the first 25 seconds of the engine start-up process for the conditions studied (λ_{engine} = 0.8-1.0, up to 100% SAI).

- Thermal oxidation was observed to decrease in the exhaust port and increase in the exhaust runner as the secondary air flow rate increased. The overall fraction of thermal oxidation was also found to increase in the exhaust port and runner as the secondary air flow rate increased.

- Analysis of the experimental data showed that the post-catalyst HC emissions levels were optimized with secondary air flow rates corresponding to an overall exhaust lambda of 1.3.

- The UEGO reading lambda values were significantly different from the actual lambda values with SAI, due to the significant levels of combustible gases (HC, CO and H_2) in an overall lean mixture of engine-out exhaust gas and secondary air.

- Quantification of trapped HC and condensed water inside the catalyst was required to precisely evaluate mass emissions and thermal states of the exhaust gas.

- Higher levels of HC appeared to reduce the extent of the CO oxidation reaction prior to the catalyst. However, CO oxidation occurred more rapidly than HC oxidation in general.

- Agreement within 50 K was achieved between time-averaged temperatures predicted by the heat transfer model and direct time-averaged temperatures measured from the experiments.

- The amount of chemical energy released from exhaust oxidation was observed to increase significantly with higher levels of fuel enrichment at each secondary air flow rate condition. However, the heat loss from the cylinder exit to the pre-catalyst location was not sensitive to the engine lambda and secondary air flow rate. Higher heat transfer rates from increased temperatures and mass flow rates with SAI were compensated by the increased chemical energy released from the oxidation of HC, CO and H_2 with SAI.

6.3 Conclusions

A careful optimization of SAI system can maximize the simultaneous benefit of reducing converter-in emissions and improving catalyst light-off performance during cold start. A variety of experimental techniques quantified exhaust gas emissions at several exhaust locations, from the cylinder exit to the catalytic converter outlet. A phenomenological model of exhaust heat transfer combined with the gas composition analysis provided additional insight into the thermal and chemical processes of the exhaust gas with SAI. The following conclusions were based on the results of those engine start-up experiments and their analysis.

- Significant emissions reduction can be achieved with secondary air injection by the thermal oxidation process prior to the catalyst, which results in higher exhaust gas temperatures and therefore enhances the chemical process inside the catalyst by faster catalyst light-off. The catalytic converter light-off performance is affected by both thermal and catalytic oxidation reactions of HC, CO and H_2 with SAI.

- The analysis shows a trade-off between the amount of thermal and catalytic oxidation reactions occurring in the different parts of the exhaust system. Enhancing thermal oxidation in the exhaust port and runner effectively raises the exhaust gas temperature and also lowers the converter-in emission level. However, an increase in the thermal oxidation reaction can cause a decrease in

the catalytic oxidation reaction due to the increased consumption of reactants upstream of the catalyst. Comparable overall HC emissions reductions are achieved over an engine lambda range of 0.8 to 0.9 and secondary air flow rate range of 67% to 33%.

- Substantial spark retard is required to initiate the thermal oxidation reaction. Holding retarded spark during the catalyst warm-up period (~10 sec) of engine operation will add more energy into the exhaust gas and enhance thermal oxidation in the exhaust port and runner.

- To maximize thermal oxidation, the secondary air should be injected as close to the exhaust valve as possible. The chemical energy released in this way out-weighs the cooling effect of cold secondary air.

- An increase of the amount of secondary air permits a faster mixing of the exhaust gas with secondary air. The conditions at the port are favorable for higher oxidation reactions with increased mixing rates. However, the more effective cooling and less amount of combustible gas prior to the catalyst with the higher amount of secondary air have offsetting effects on the catalytic oxidation reaction inside the catalyst. Therefore, the post-catalyst HC emission levels are not strongly affected by the mixing rates.

- Carbon-based species tracking and exhaust gas quenching experiments provide the quantitative information that can be used in a reacting plug flow heat transfer model.

- Secondary air can utilize more than 90% of cylinder-out exhaust gas chemical energy by promoting the burn-up process in the exhaust system during the cold start-up process.

- The results reported here show that an overall exhaust lambda of 1.3 is required to achieve the minimum post-catalyst HC emissions level with secondary air injection during cold start.

References

1. Heywood, J.B., *Internal Combustion Engine Fundamentals*, McGraw-Hill, New York, 1988.
2. Cheng, W.K. and Santoso, H., "Mixture preparation and hydrocarbon emissions behaviors in the first cycle of SI engine cranking", SAE Paper 2002-01-2805, 2002.
3. Takeda, K., Yaegashi, T., Sekiguchi, K., Saito, K., and Imatake, N., "Mixture preparation and HC emissions of a 4-valve engine during cold starting and warm-up", SAE Paper 950074, 1995.
4. Meyer, R. and Heywood, J.B., "Evaporation of in-cylinder liquid fuel droplets in an SI engine: A diagnostic-based modeling study", SAE Paper 1999-01-0567, 1999.
5. Heck, R.M. and Farrauto, R.J., *Catalytic Air Pollution Control*, Van Nostrand Reinhold, New York, 1995.
6. EPA420-F-99-017, *Emission Facts*, May 1999.
7. Eastwood, P., *Critical Topics in Exhaust Gas Aftertreatment*, Research Studies Press Ltd., UK, 2000.
8. Borland, M. and Zhao, F., "Application of Secondary Air Injection for Simultaneously Reducing Converter-In Emissions and Improving Catalyst Light-Off Performance", SAE Paper 2002-01-2803, 2002.
9. Nishizawa, K., Yamada, T., Ishizuka, Y., and Inoue, T., "Technologies for Reducing Cold-Start Emissions of V6 ULEVs", SAE Paper 971022, 1977.
10. Crane, M.E., Thring, R.H., Podnar D.J., Dodge, L.G., "Reduced Cold-Start Emissions Using Rapid Exhaust Port Oxidation (REPO) in a Spark-Ignition Engine", SAE Paper 970264, 1977.
11. Development Instrumentation Group, *Delco Modular Development System Manual,* Delco Electronics Corporation, 1997.
12. Cambustion HFR400, September 2005 <http://www.cambustion.co.uk/instruments/hfr400>.

13. Cambustion NDIR500, September 2005 <http://www.cambustion.co.uk/instruments/ndir500/ndirprinciples.html>.
14. UTG-91 Fuel Properties, Chevron Phillips Chemical Company LLC, October 2005 <http://www.cpchem.com/enu/tds_unsecured/UTG-91.pdf>.
15. Klein, D. and Cheng, W.K., "Spark ignition engine hydrocarbon emissions behaviors in stopping and restarting", SAE Paper, 2002-01-2804, 2002.
16. Henein, N.A., Tagomori, M.K., Yassine, M.K., Asmus, T.W., Thomas, C.P., and Hartman, P.G., "Cycle-by-cycle analysis of HC emissions during cold start of gasoline engines", SAE Paper 952402, 1995.
17. Castaing, B.M., Coward, J.S., and Cheng, W.K., "Fuel metering effects on hydrocarbon emissions and engine stability during cranking and start-up in a port fuel injected spark ignition engine", SAE Paper 2000-01-2836, 2000.
18. Katashiba, H., Nishiyama, R., Nishimura, Y., Hosoya, Y., Arai, H., and Washino, S., "Development of an Effective Air-Injection System with Heated Air for LEV/ULEV", SAE Paper 950411, 1995.
19. Cheng, W.K., Summers, T., and Collings, N., "The Fast-Response Flame Ionization Detector", Progress in Energy and Combustion Science, Volume 24, Issue 2, 1998, Pages 89-124.
20. Caton, J., "Heat Transfer, Mixing and Hydrocarbon Oxidation in an Engine Exhaust Port", Ph.D. Thesis, MIT Department of Mechanical Engineering, 1979.
21. Fox, J.W., Cheng, W.K., and Heywood, J.B., "A model for predicting residual gas fraction in spark-ignition engines", SAE Paper 931025, 1993.
22. Nakayama, Y., Maruya, T., Oikawa, T. Kawamata, M., Fujiwara, M., "Reduction on HC Emission from VTEC Engine During Cold-Start Condition," SAE Paper 940481, 1994.
23. Hallgren, B.E., "Impact of Retarded Spark Timing on Engine Combustion, Hydrocarbon Emissions, and Fast Catalyst Light-Off", Ph.D. Thesis, MIT Department of Mechanical Engineering, 2005.
24. Mills, A.F., *Heat Transfer*, Prentice Hall, New Jersey, 1999.

25. Caton, J., "Comparisons of Thermocouple,Time-averaged and Mass-Averaged Exhaust Gas Temperatures for a Spark-Ignited Engine," SAE Paper 820050, 1982.

Appendix A

Emissions Data

A.1 Time-resolved HC, CO and CO_2 Data

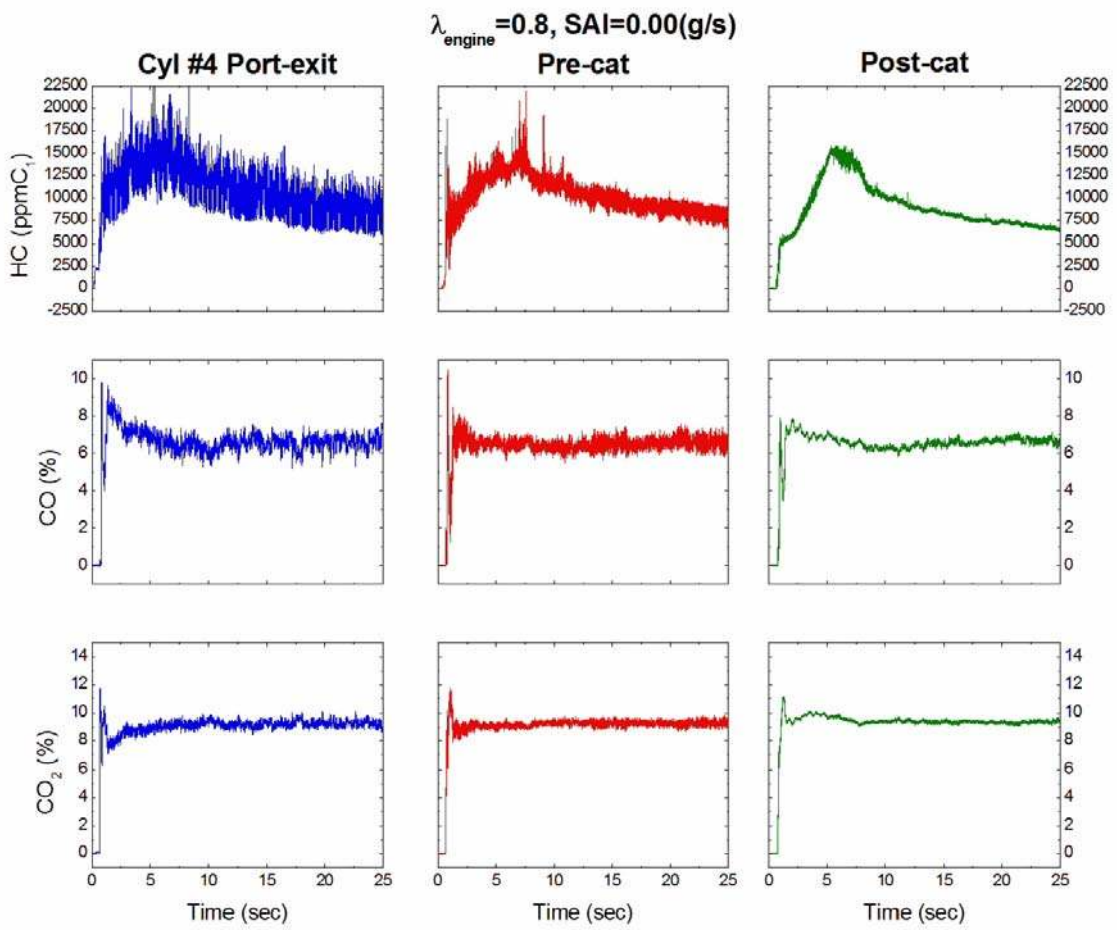

Figure A-1 HC, CO and CO_2 concentrations as a function of cycle number at various locations in the exhaust system (λ_{engine} = 0.8, SAI = 0.00 g/s).

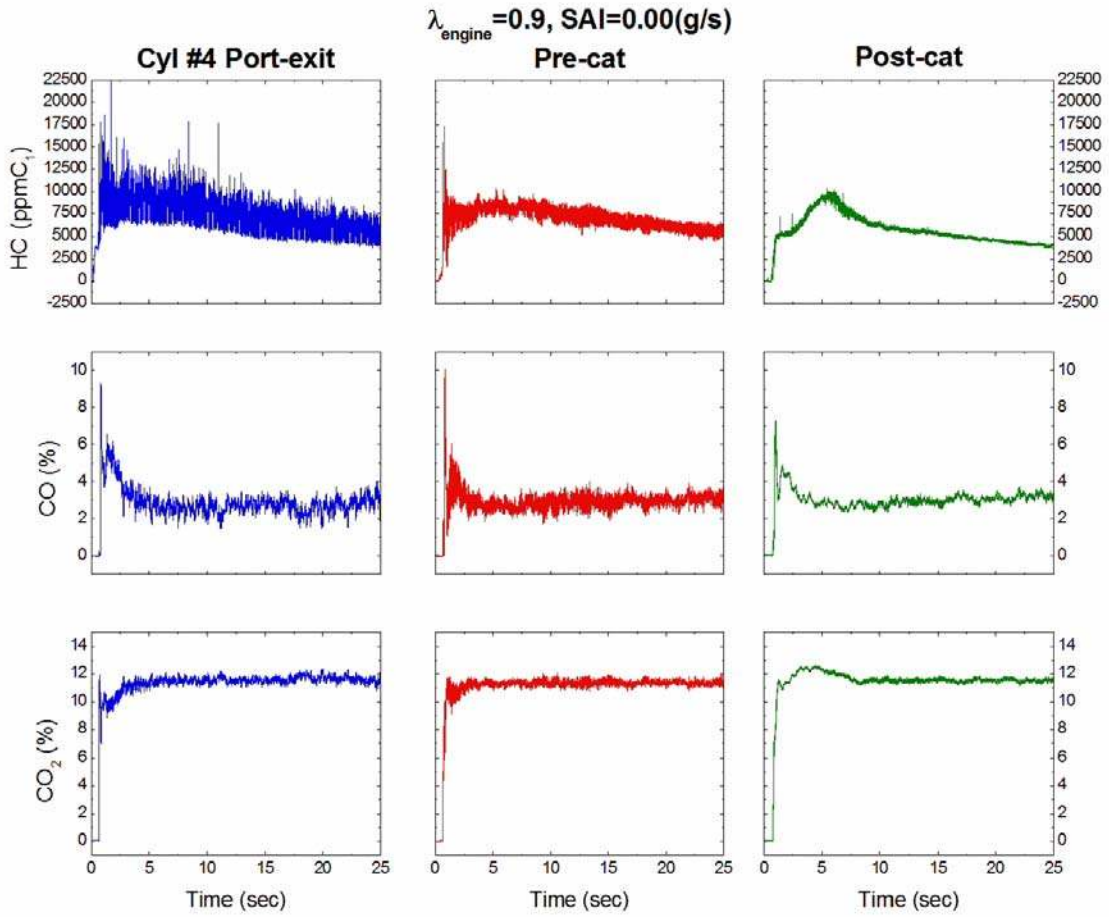

Figure A-2 HC, CO and CO_2 concentrations as a function of cycle number at various locations in the exhaust system (λ_{engine} = 0.9, SAI = 0.00 g/s).

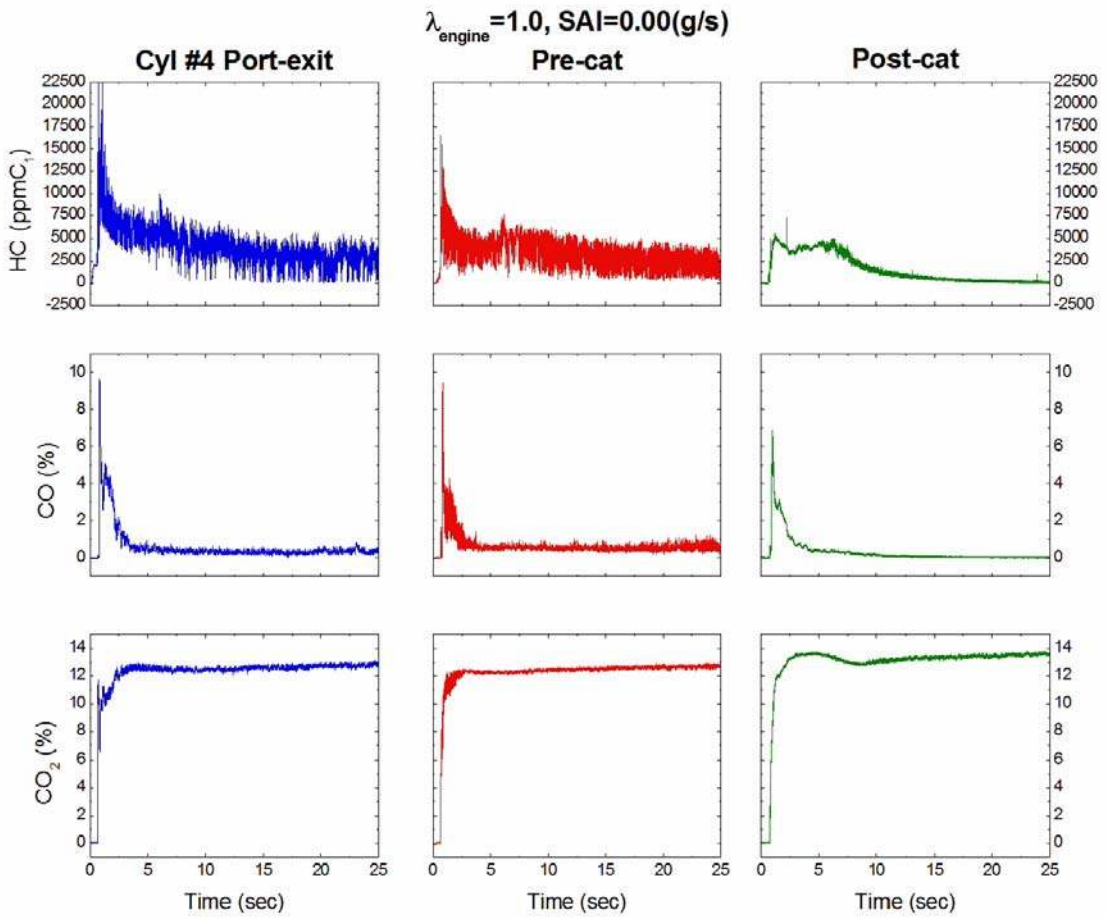

Figure A-3 HC, CO and CO_2 concentrations as a function of cycle number at various locations in the exhaust system (λ_{engine} = 1.0, SAI = 0.00 g/s).

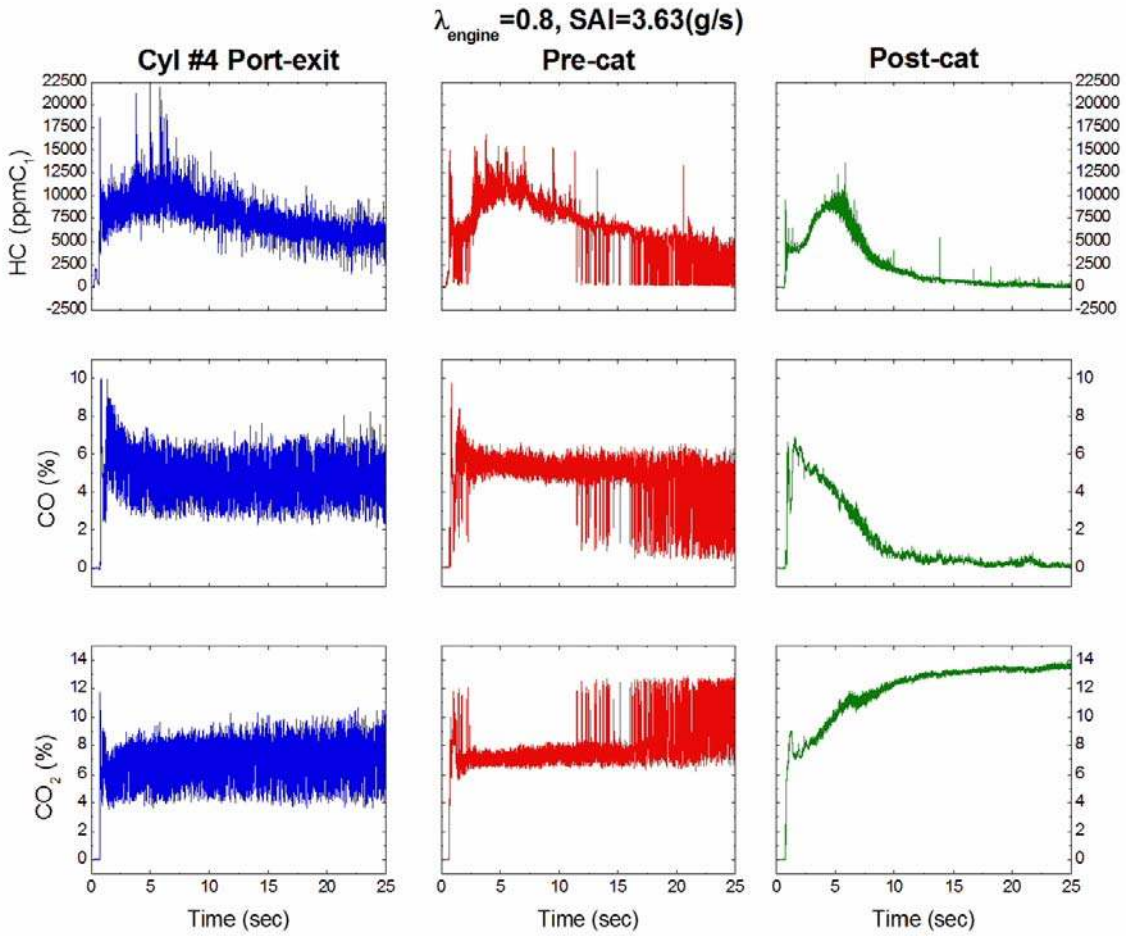

Figure A-4 HC, CO and CO_2 concentrations as a function of cycle number at various locations in the exhaust system (λ_{engine} = 0.8, SAI = 3.63 g/s).

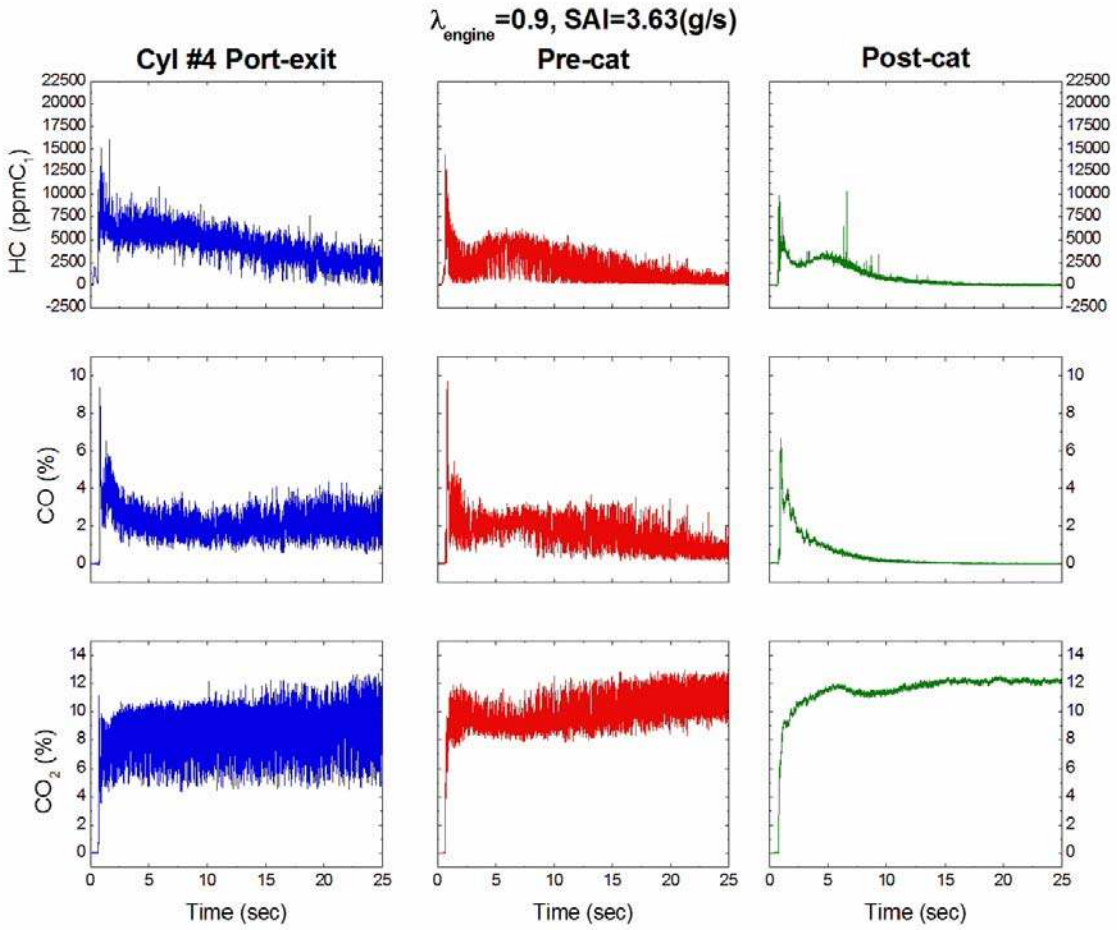

Figure A-5 HC, CO and CO_2 concentrations as a function of cycle number at various locations in the exhaust system (λ_{engine} = 0.9, SAI = 3.63 g/s).

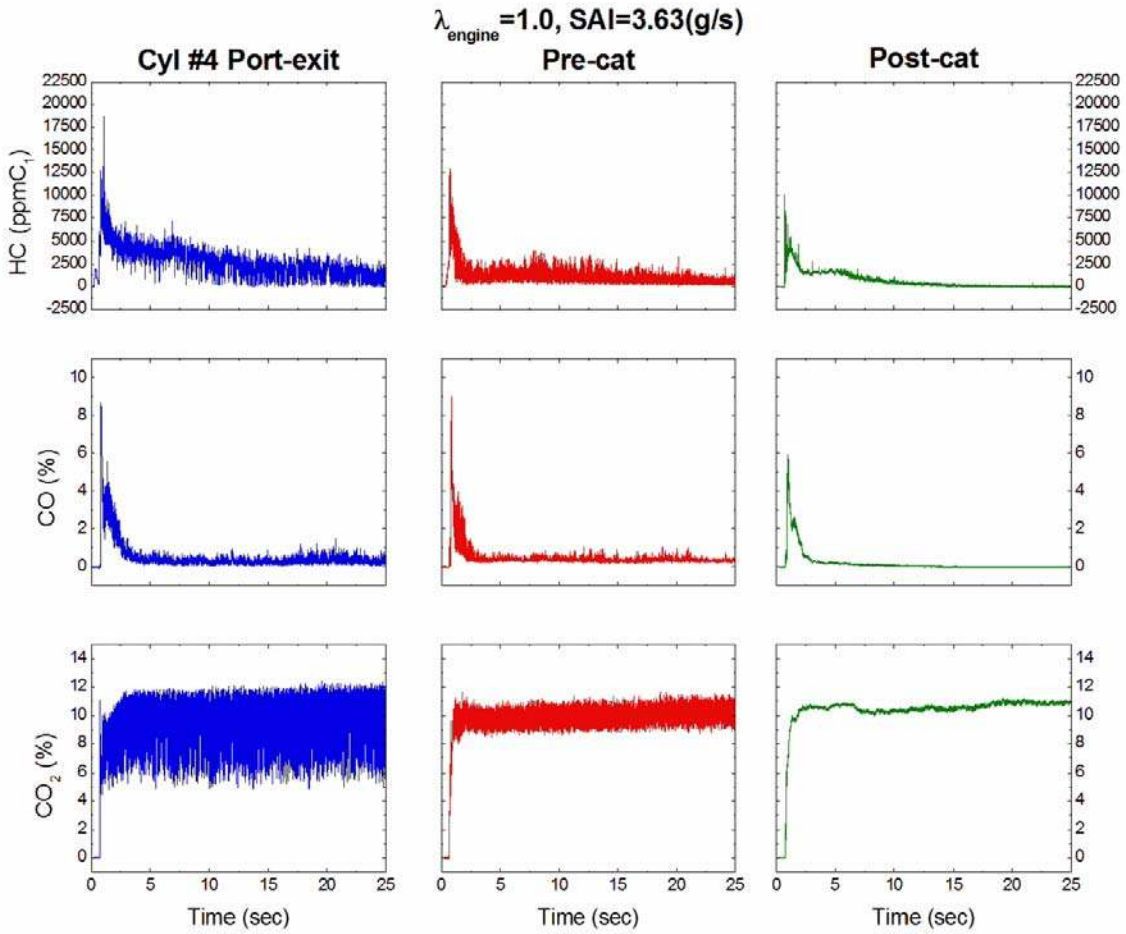

Figure A-6 HC, CO and CO_2 concentrations as a function of cycle number at various locations in the exhaust system (λ_{engine} = 1.0, SAI = 3.63 g/s).

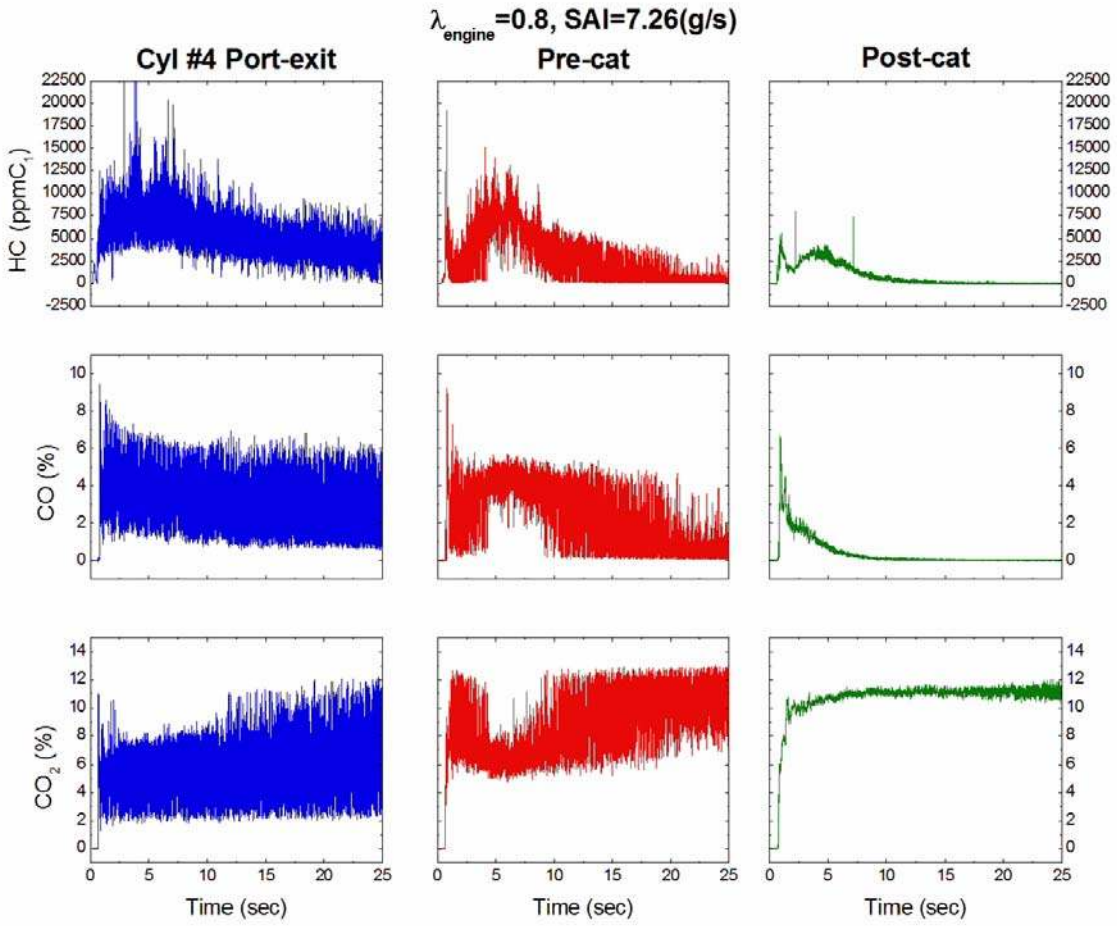

Figure A-7 HC, CO and CO_2 concentrations as a function of cycle number at various locations in the exhaust system (λ_{engine} = 0.8, SAI = 7.26 g/s).

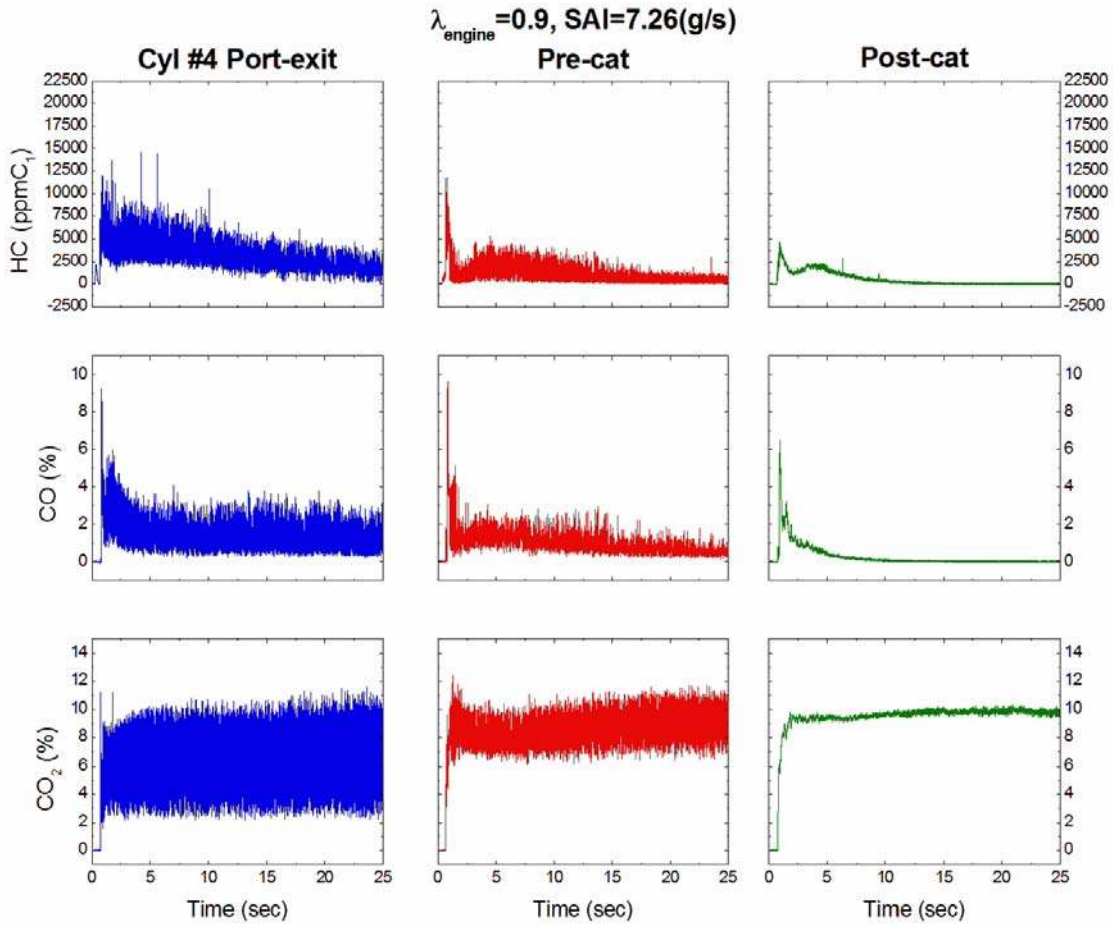

Figure A-8 HC, CO and CO_2 concentrations as a function of cycle number at various locations in the exhaust system (λ_{engine} = 0.9, SAI = 7.26 g/s).

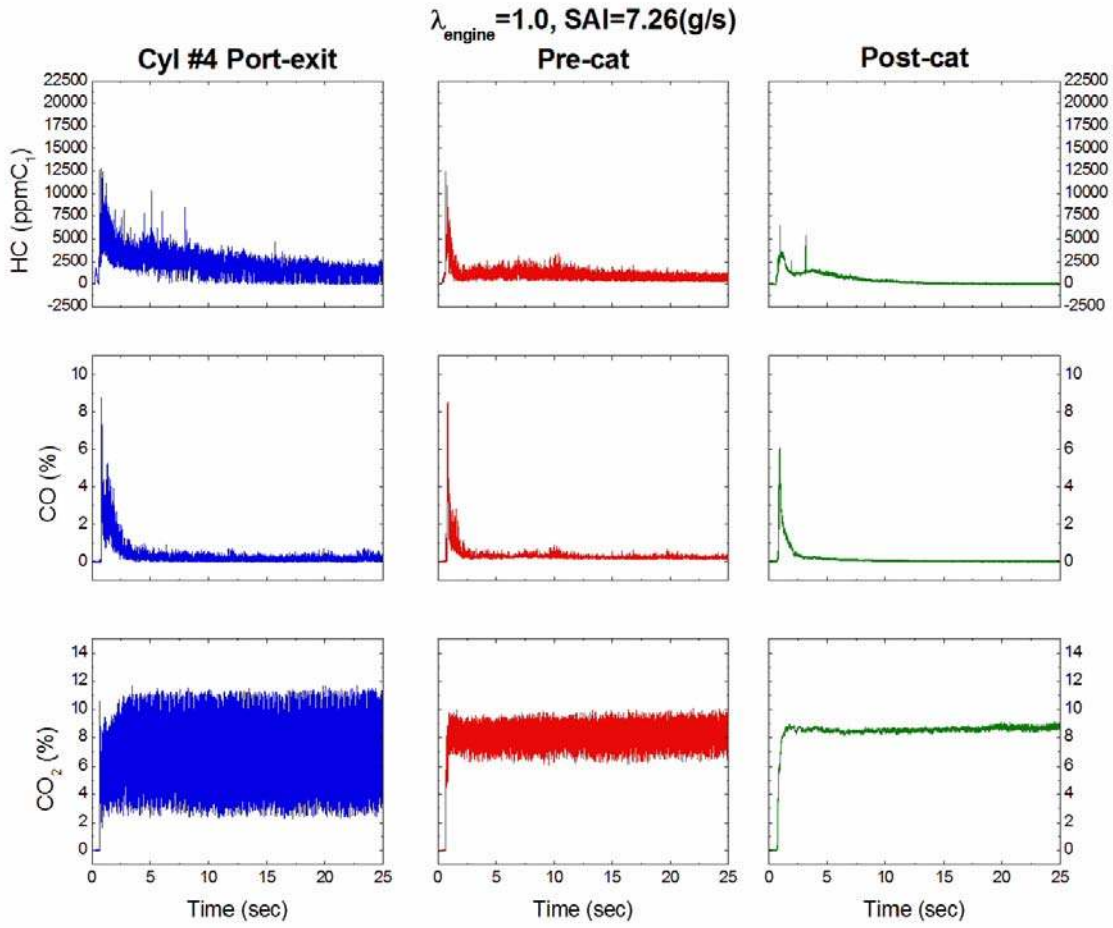

Figure A-9 HC, CO and CO_2 concentrations as a function of cycle number at various locations in the exhaust system (λ_{engine} = 1.0, SAI = 7.26 g/s).

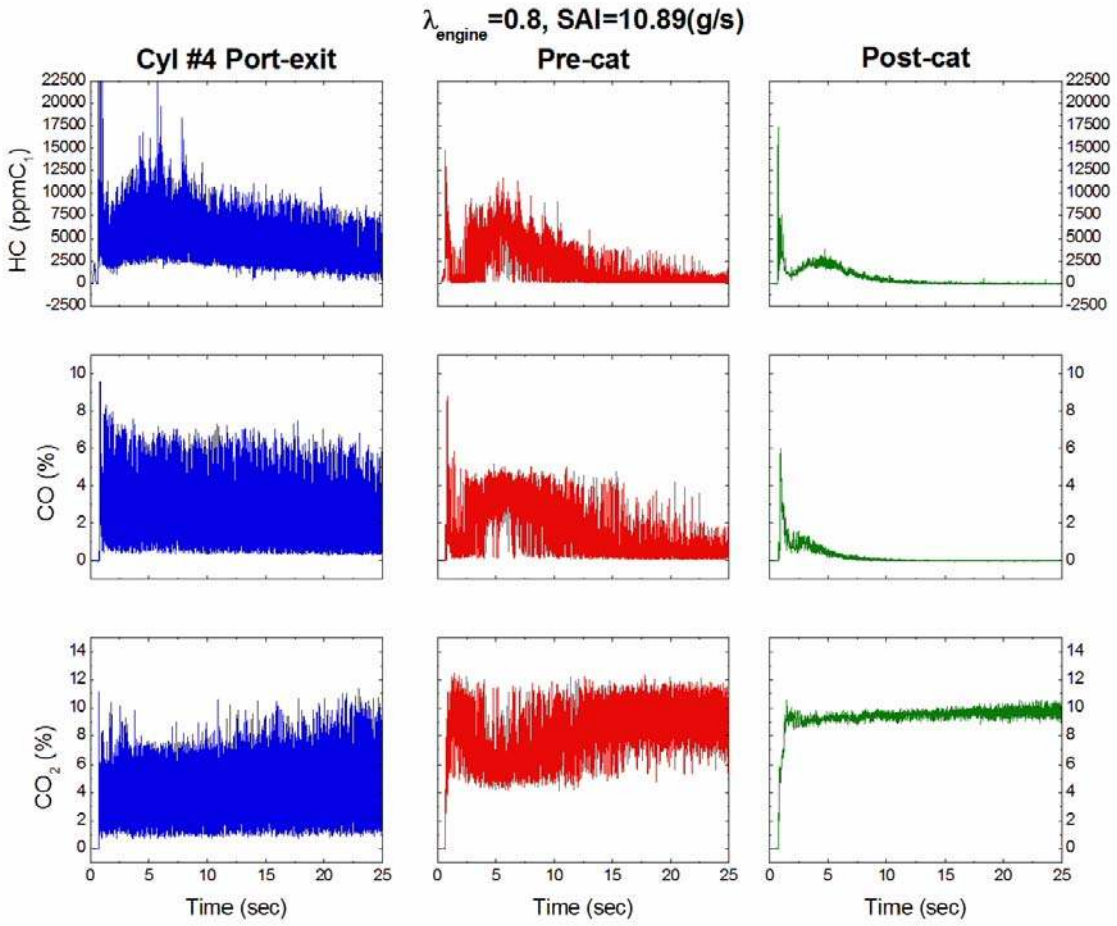

Figure A-10 HC, CO and CO_2 concentrations as a function of cycle number at various locations in the exhaust system (λ_{engine} = 0.8, SAI = 10.89 g/s).

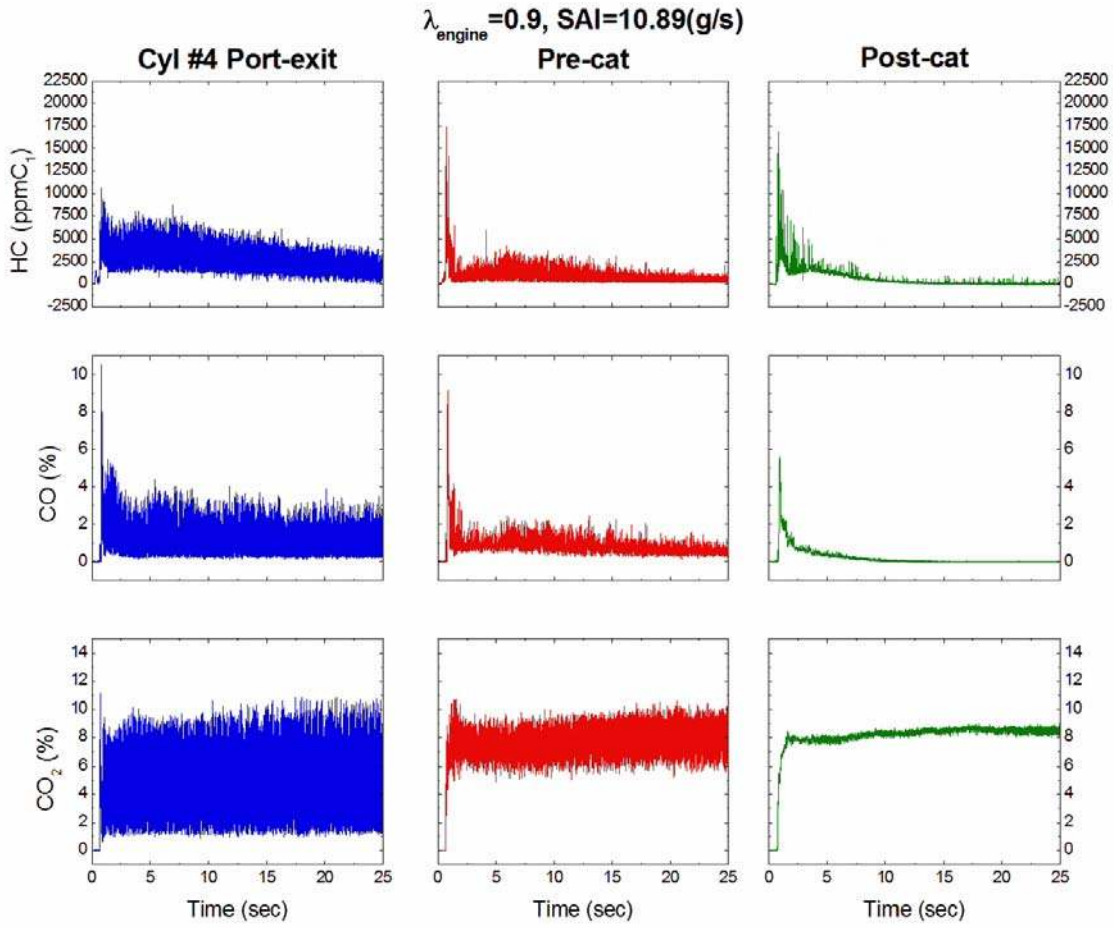

Figure A-11 HC, CO and CO_2 concentrations as a function of cycle number at various locations in the exhaust system (λ_{engine} = 0.9, SAI = 10.89 g/s).

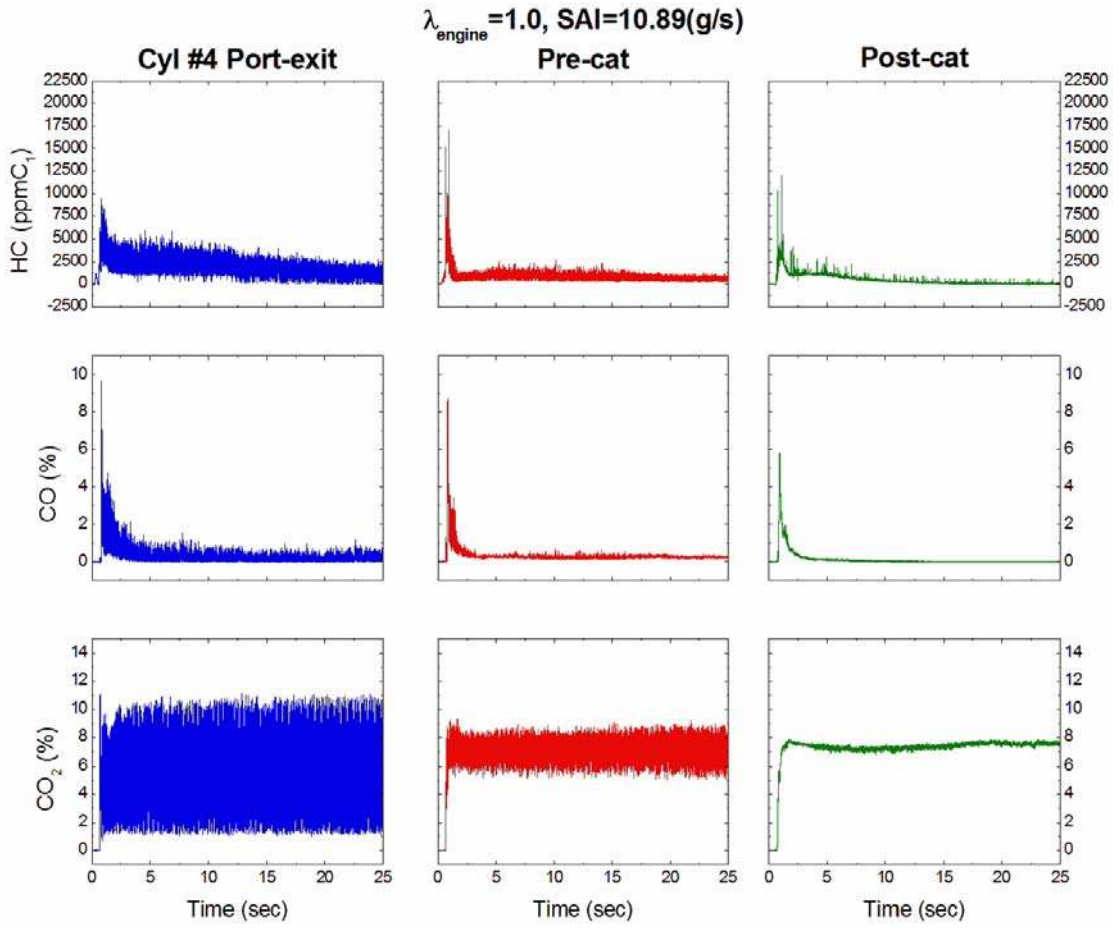

Figure A-12 HC, CO and CO_2 concentrations as a function of cycle number at various locations in the exhaust system (λ_{engine} = 1.0, SAI = 10.89 g/s).

A.2 Cycle-Averaged CO, CO_2, H_2 and H_2O Concentrations

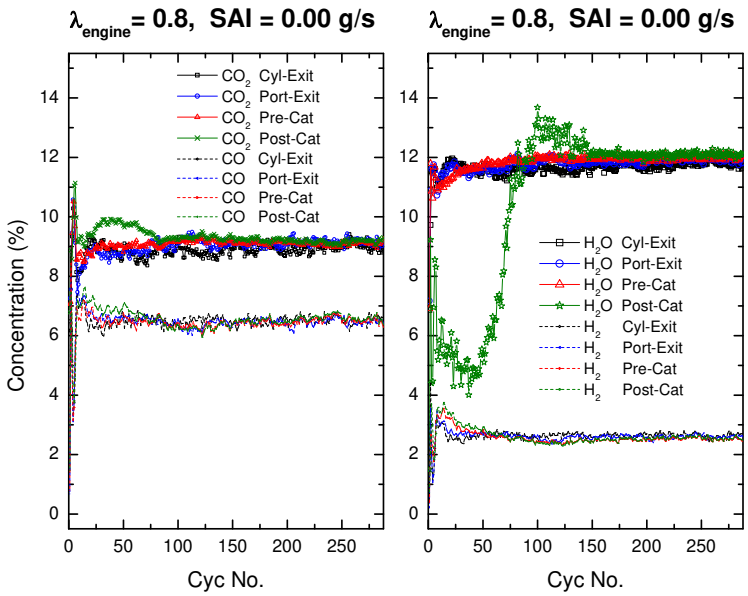

Figure A-13 Cycle-averaged CO, CO_2, H_2 and H_2O concentrations as a function of cycle number at various locations in the exhaust system (λ_{engine} = 0.8, SAI = 0.00 g/s).

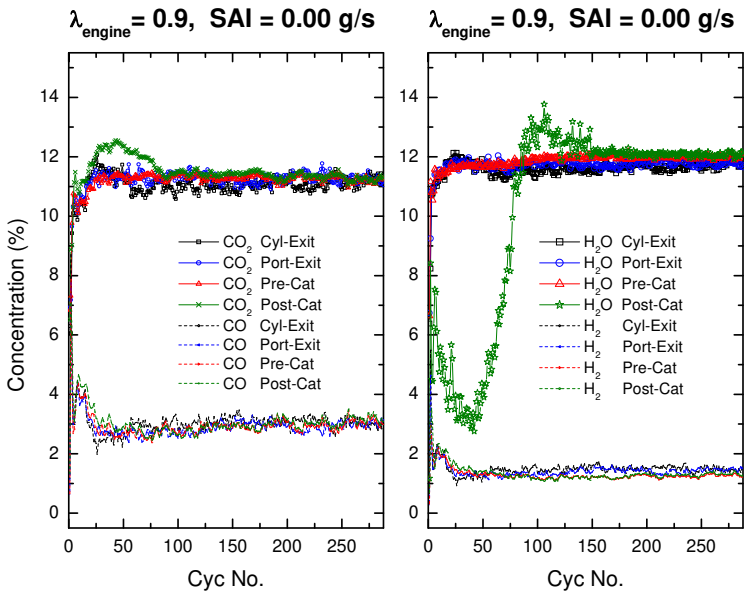

Figure A-14 Cycle-averaged CO, CO_2, H_2 and H_2O concentrations as a function of cycle number at various locations in the exhaust system (λ_{engine} = 0.9, SAI = 0.00 g/s).

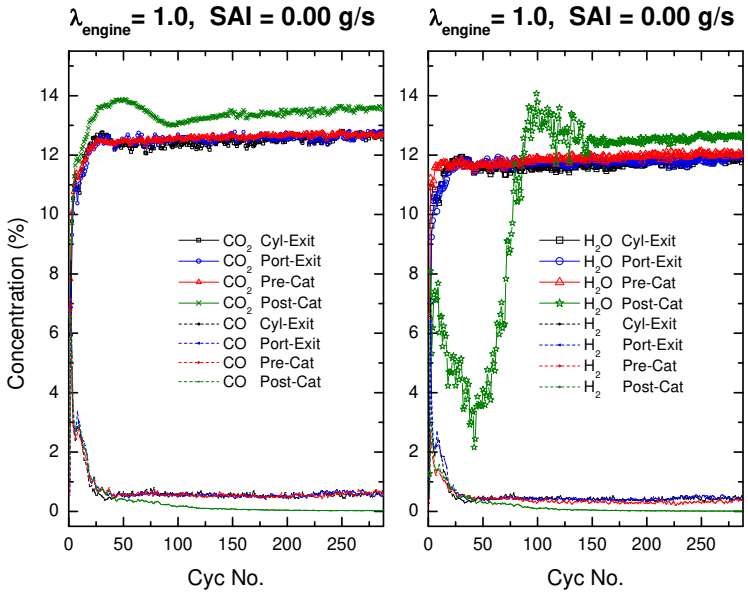

Figure A-15 Cycle-averaged CO, CO_2, H_2 and H_2O concentrations as a function of cycle number at various locations in the exhaust system (λ_{engine} = 1.0, SAI = 0.00 g/s).

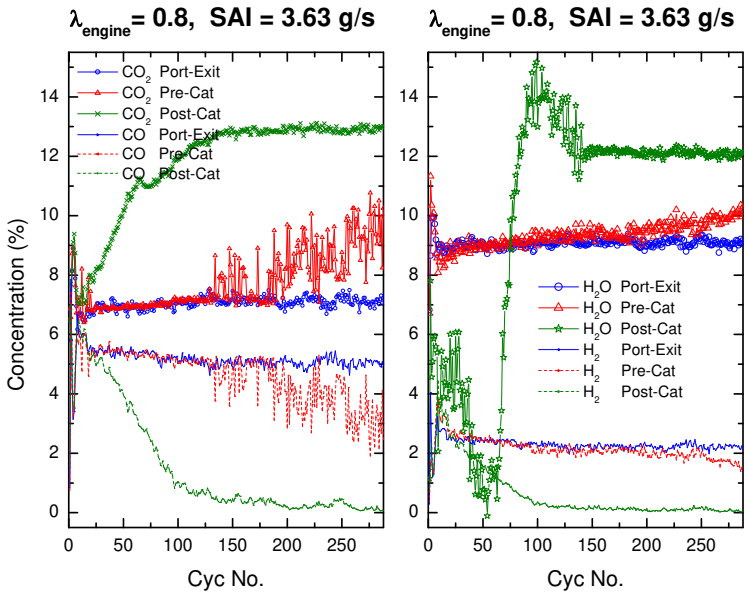

Figure A-16 Cycle-averaged CO, CO_2, H_2 and H_2O concentrations as a function of cycle number at various locations in the exhaust system (λ_{engine} = 0.8, SAI = 3.63 g/s).

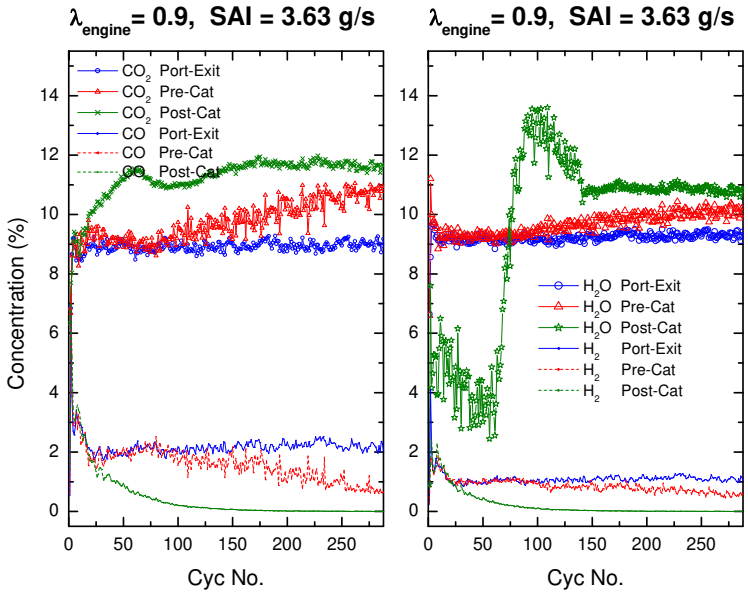

Figure A-17 Cycle-averaged CO, CO_2, H_2 and H_2O concentrations as a function of cycle number at various locations in the exhaust system (λ_{engine} = 0.9, SAI = 3.63 g/s).

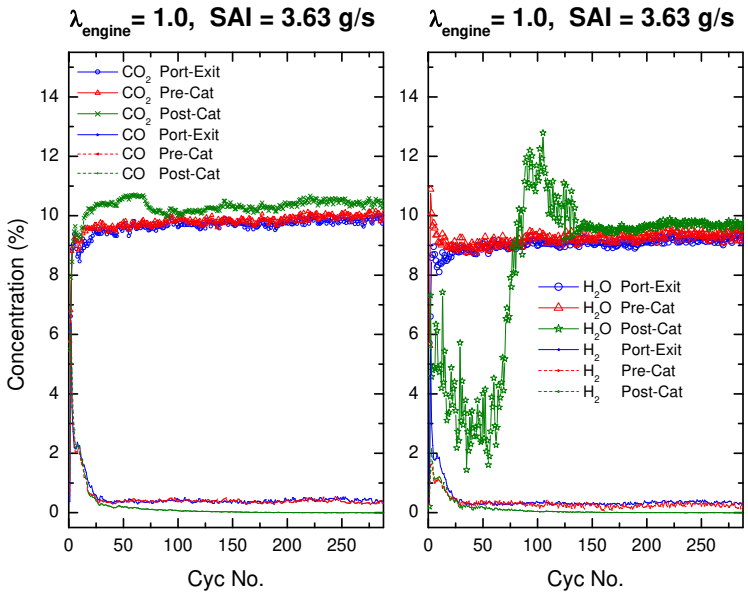

Figure A-18 Cycle-averaged CO, CO_2, H_2 and H_2O concentrations as a function of cycle number at various locations in the exhaust system (λ_{engine} = 1.0, SAI = 3.63 g/s).

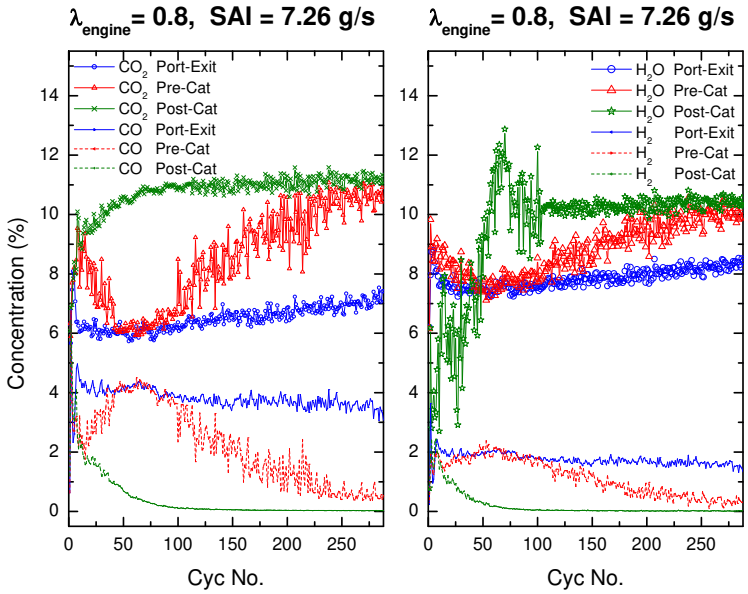

Figure A-19 Cycle-averaged CO, CO_2, H_2 and H_2O concentrations as a function of cycle number at various locations in the exhaust system (λ_{engine} = 0.8, SAI = 7.26 g/s).

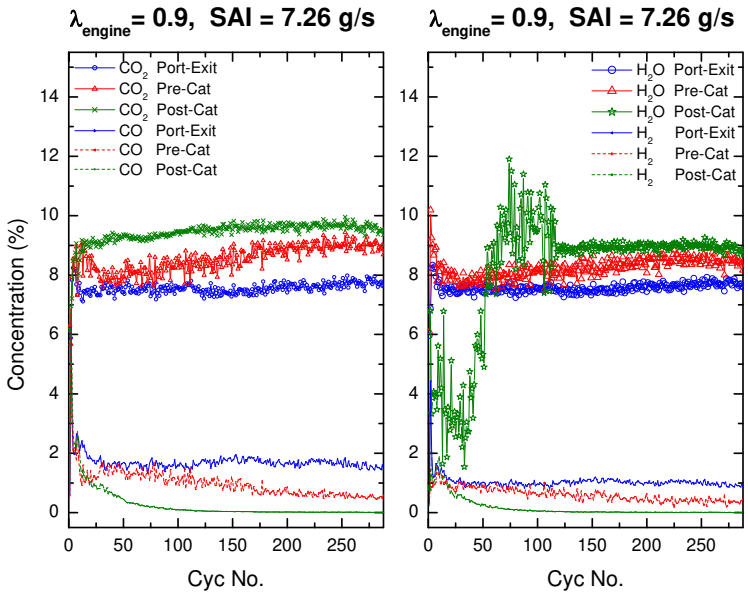

Figure A-20 Cycle-averaged CO, CO_2, H_2 and H_2O concentrations as a function of cycle number at various locations in the exhaust system (λ_{engine} = 0.9, SAI = 7.26 g/s).

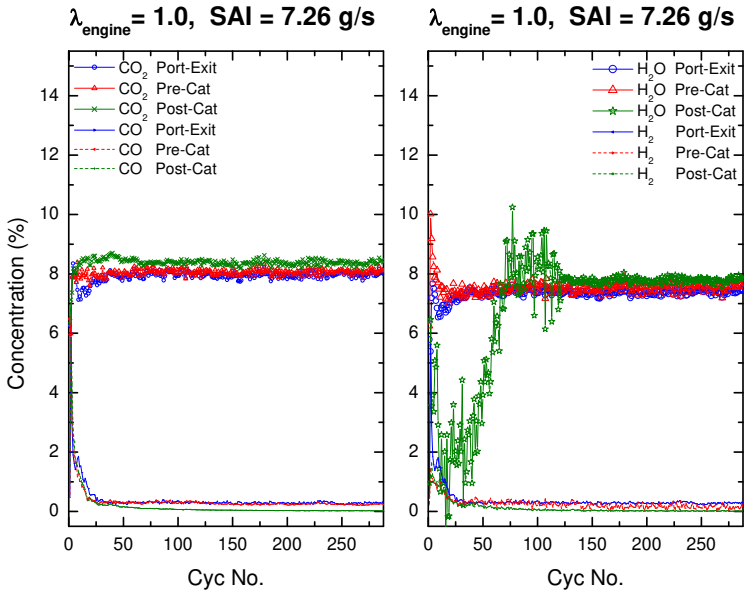

Figure A-21 Cycle-averaged CO, CO_2, H_2 and H_2O concentrations as a function of cycle number at various locations in the exhaust system (λ_{engine} = 1.0, SAI = 7.26 g/s).

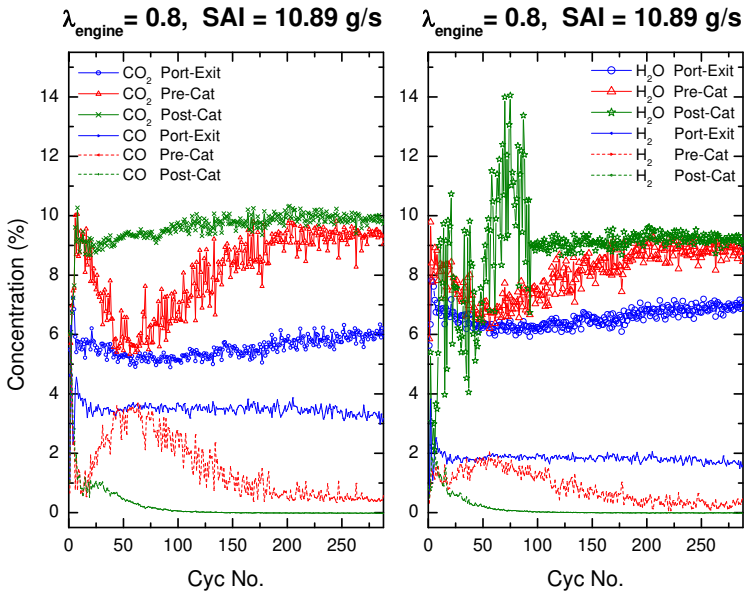

Figure A-22 Cycle-averaged CO, CO_2, H_2 and H_2O concentrations as a function of cycle number at various locations in the exhaust system (λ_{engine} = 0.8, SAI = 10.89 g/s).

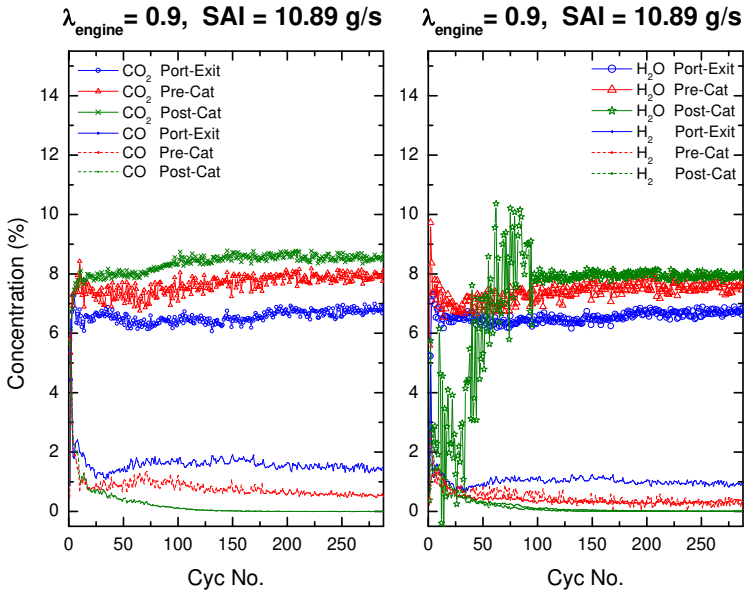

Figure A-23 Cycle-averaged CO, CO_2, H_2 and H_2O concentrations as a function of cycle number at various locations in the exhaust system (λ_{engine} = 0.9, SAI = 10.89 g/s).

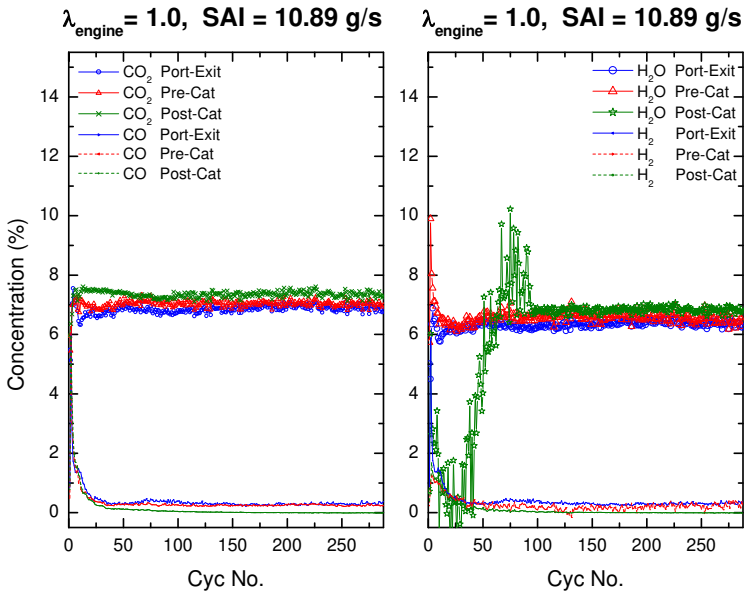

Figure A-24 Cycle-averaged CO, CO_2, H_2 and H_2O concentrations as a function of cycle number at various locations in the exhaust system (λ_{engine} = 1.0, SAI = 10.89 g/s).

A.3 Cycle-Averaged HC and CO Mass Emissions

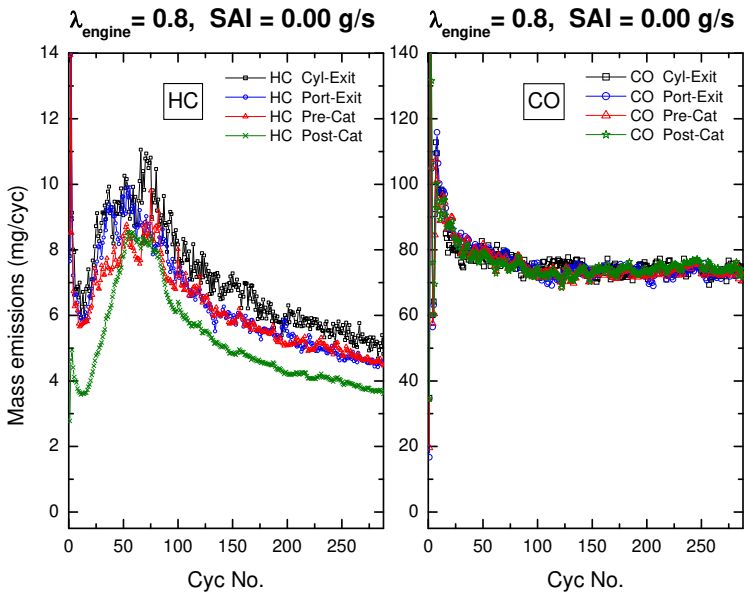

Figure A-25 Cycle-averaged HC and CO mass emissions as a function of cycle number at various locations in the exhaust system (λ_{engine} = 0.8, SAI = 0.00 g/s).

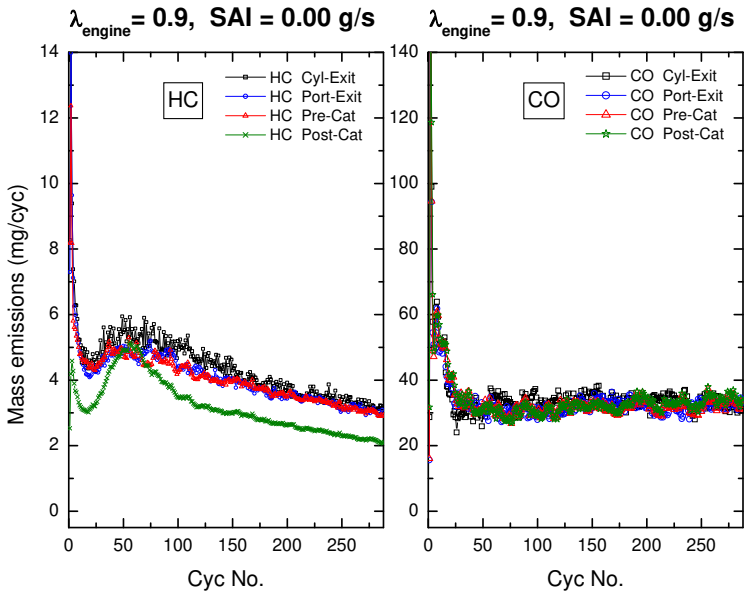

Figure A-26 Cycle-averaged HC and CO mass emissions as a function of cycle number at various locations in the exhaust system (λ_{engine} = 0.9, SAI = 0.00 g/s).

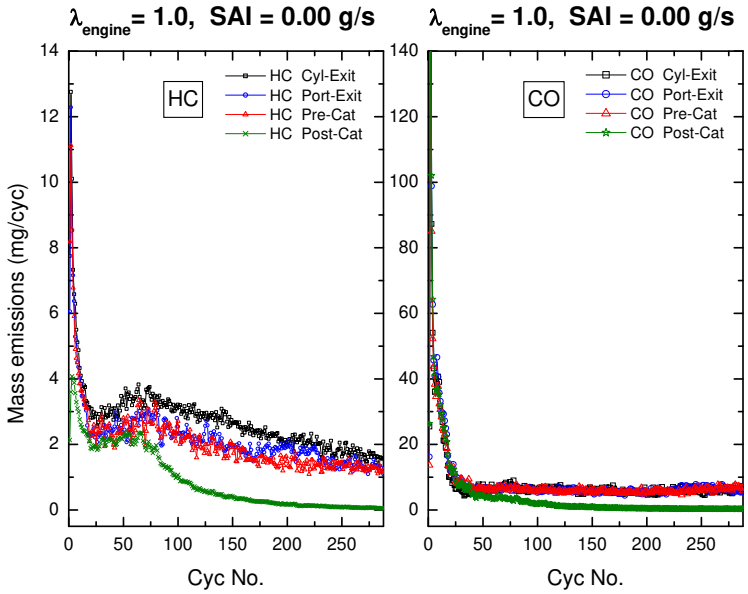

Figure A-27 Cycle-averaged HC and CO mass emissions as a function of cycle number at various locations in the exhaust system (λ_{engine} = 1.0, SAI = 0.00 g/s).

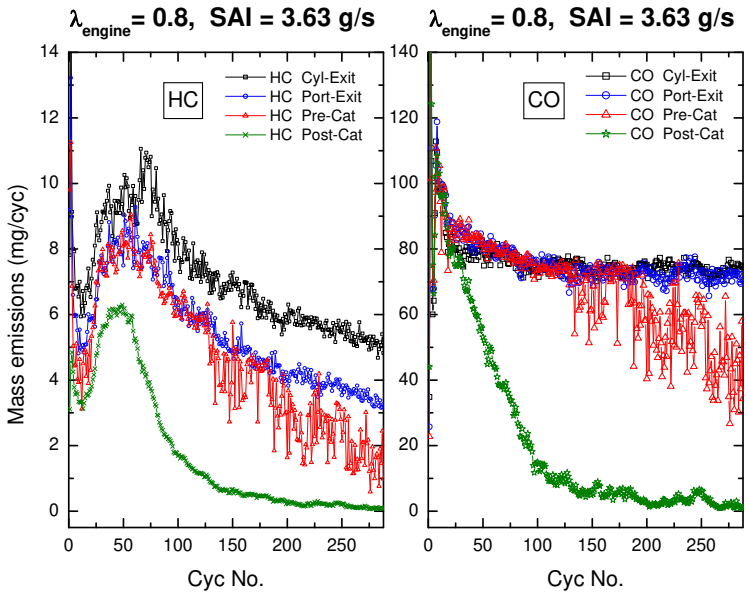

Figure A-28 Cycle-averaged HC and CO mass emissions as a function of cycle number at various locations in the exhaust system (λ_{engine} = 0.8, SAI = 3.63 g/s).

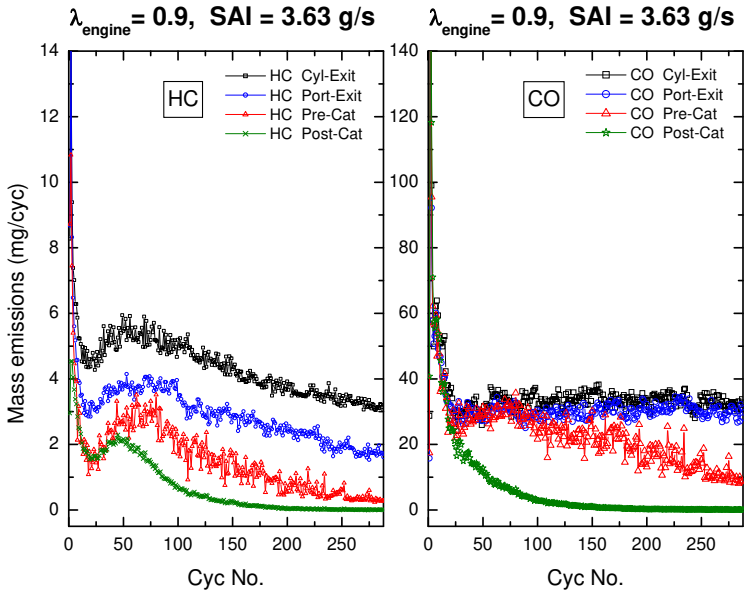

Figure A-29 Cycle-averaged HC and CO mass emissions as a function of cycle number at various locations in the exhaust system (λ_{engine} = 0.9, SAI = 3.63 g/s).

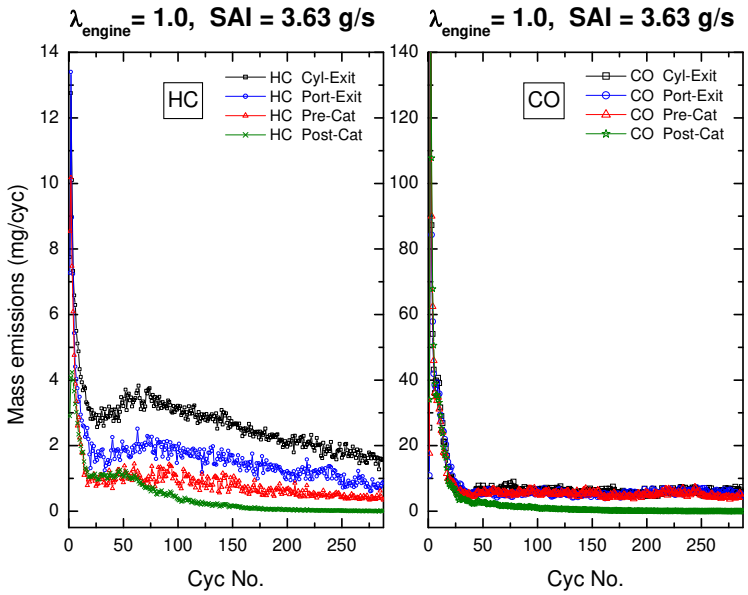

Figure A-30 Cycle-averaged HC and CO mass emissions as a function of cycle number at various locations in the exhaust system (λ_{engine} = 1.0, SAI = 3.63 g/s).

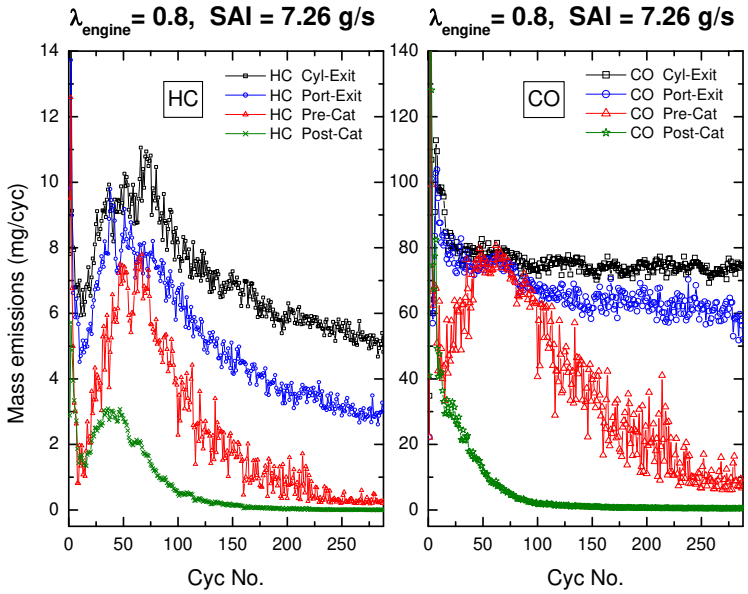

Figure A-31 Cycle-averaged HC and CO mass emissions as a function of cycle number at various locations in the exhaust system (λ_{engine} = 0.8, SAI = 7.26 g/s).

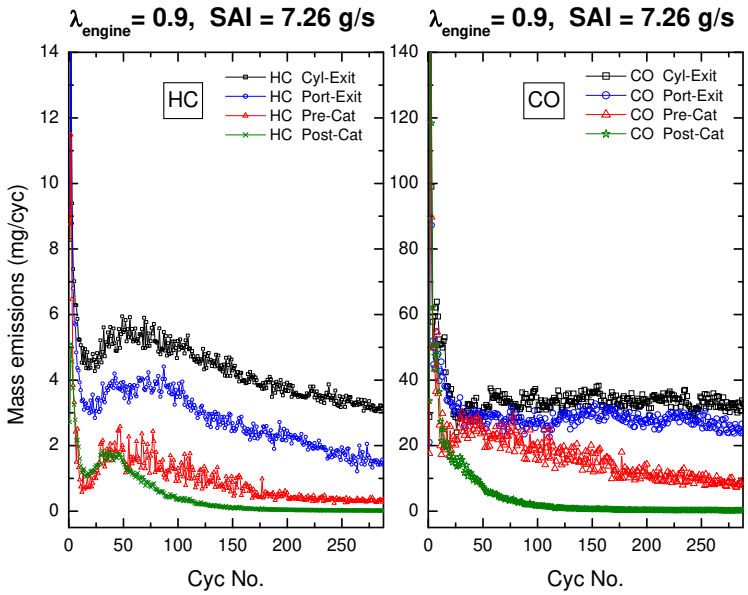

Figure A-32 Cycle-averaged HC and CO mass emissions as a function of cycle number at various locations in the exhaust system (λ_{engine} = 0.9, SAI = 7.26 g/s).

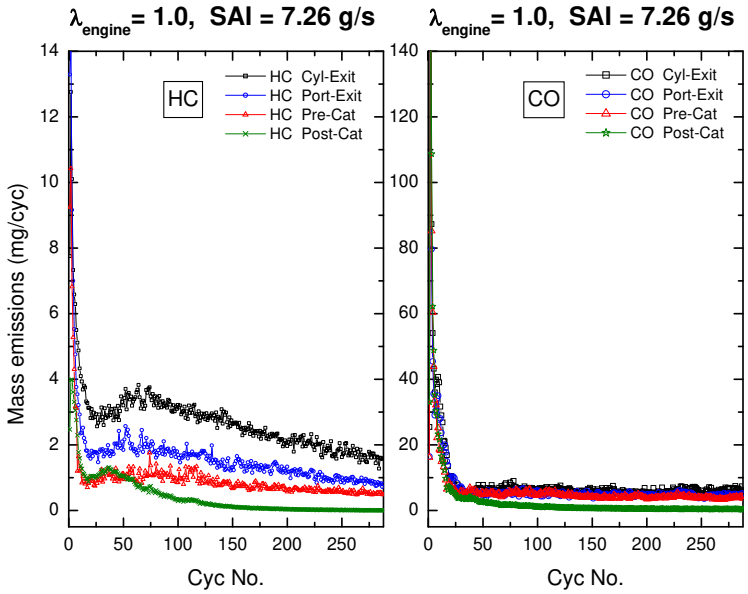

Figure A-33 Cycle-averaged HC and CO mass emissions as a function of cycle number at various locations in the exhaust system (λ_{engine} = 1.0, SAI = 7.26 g/s).

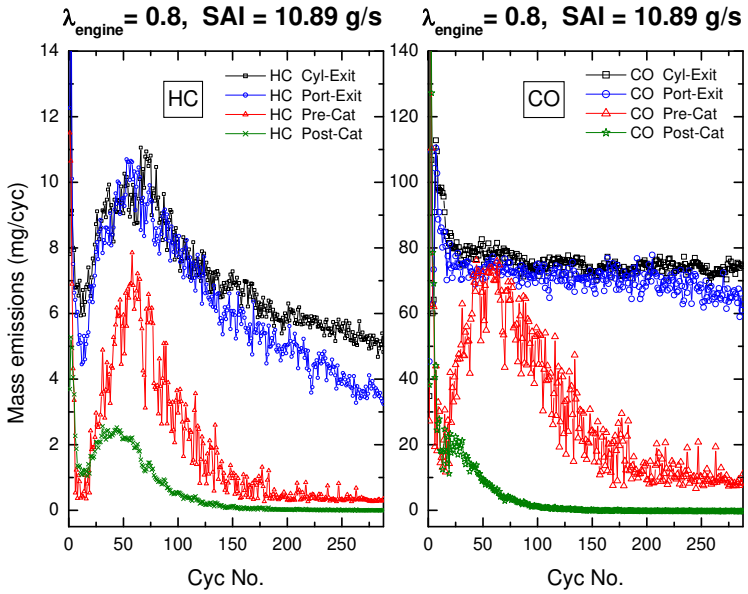

Figure A-34 Cycle-averaged HC and CO mass emissions as a function of cycle number at various locations in the exhaust system (λ_{engine} = 0.8, SAI = 10.89 g/s).

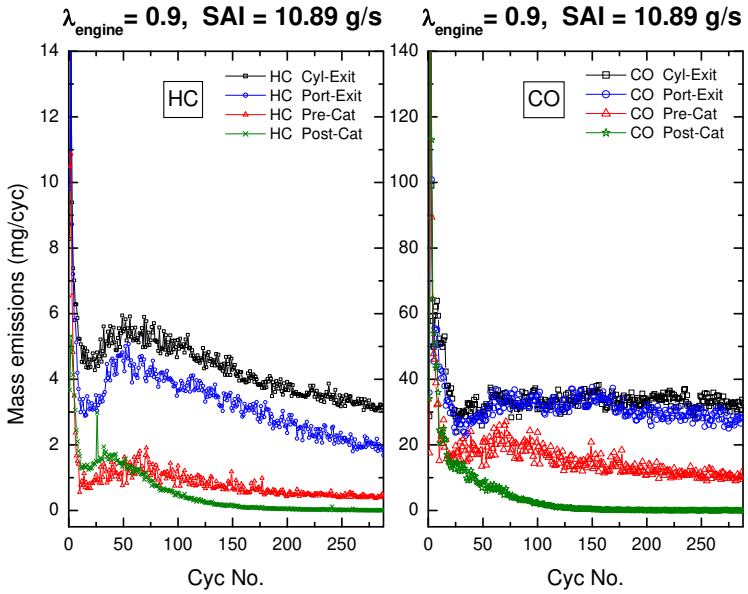

Figure A-35 Cycle-averaged HC and CO mass emissions as a function of cycle number at various locations in the exhaust system (λ_{engine} = 0.9, SAI = 10.89 g/s).

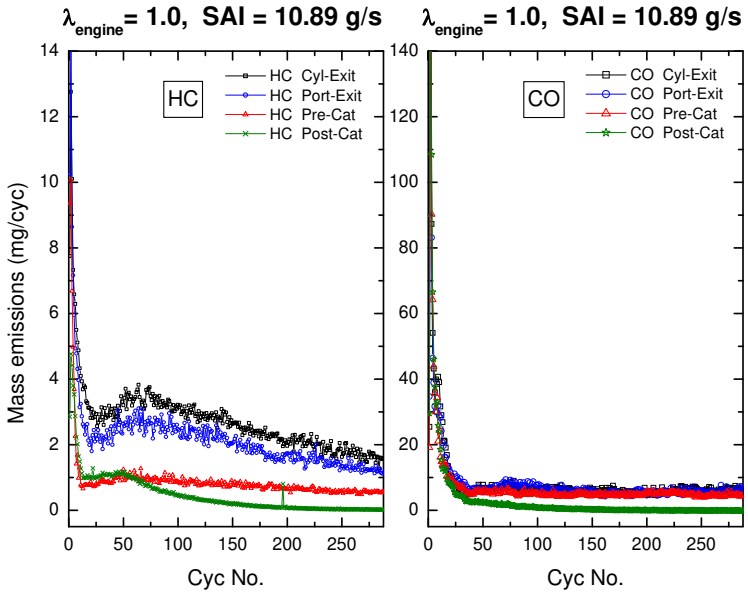

Figure A-36 Cycle-averaged HC and CO mass emissions as a function of cycle number at various locations in the exhaust system (λ_{engine} = 1.0, SAI = 10.89 g/s).

Appendix B

Analysis Methods

B.1 Residual Gas Fraction

To calculate in-cylinder air/fuel ratio and engine-out HC mass emissions, it is crucial to be able to estimate the cycle-by-cycle composition of the combustion chamber charge. This charge consists of fresh air, fuel, and residual gas from the previous cycle. The conventional SI combustion process is largely affected by the residual gas fraction. Residual gas in SI engines has a profound effect on emissions, performance, and combustion stability. Residual gas affects the combustion process through its influence on charge mass, dilution, temperature, and flame speed. Residual gas influences combustion mainly by acting as a diluent which decreases the flame speed and temperature of the resulting charge. These effects are especially important for engine idle stability and for HC emissions. Also, interpreting experimental pressure data through chemical energy release and exhaust mass flow analysis requires that the residual gas mass fraction be known. Fox's model [21] was used to estimate the residual gas fraction during the engine start-up process since the model is applicable for low to medium engine speeds such that the cylinder pressure does not substantially differ from the exhaust port pressure at IVO. In the model, the contribution of the back flow from the exhaust port to the cylinder during the valve overlap period is accounted for explicitly in terms of a valve overlap factor.

$$x_r = 1.266 \cdot \frac{OF}{N} \cdot \left(\frac{P_i}{P_e} \right)^{-0.87} \cdot \sqrt{|P_e - P_i|} + 0.632 \cdot \phi \cdot \frac{\left(P_i / P_e\right)^{-0.74}}{r_c}$$

$$OF = \frac{1.45}{B} \cdot (107 + 7.8 \cdot \Delta\theta + \Delta\theta^2) \cdot \left(\frac{L_{v,\max} \cdot D_v}{B^2} \right)$$

B.2 Water-Gas Shift Reaction

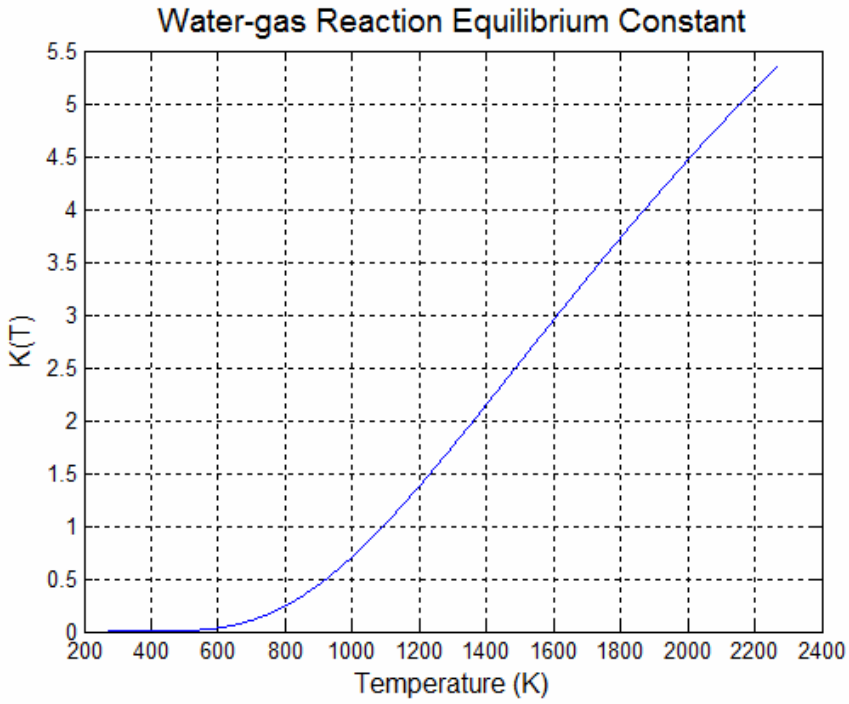

Figure B-1 Water-gas shift reaction equilibrium constant as a function of gas temperature.

$$CO_2 + H_2 = CO + H_2O$$

$$K(T) = \frac{\tilde{x}_{CO} \cdot \tilde{x}_{H_2O}}{x_{CO_2} \cdot \tilde{x}_{H_2}}$$

$$\ln K(T) = 2.743 - \frac{1.761 \times 10^3}{T} - \frac{1.611 \times 10^6}{T^2} + \frac{0.2803 \times 10^9}{T^3}$$